Laser Processing of Polymers for Controlled Carbonization and Folding

by

Moataz Magdi Mahmoud Amin Abdulhafez

Bachelors of Mechanical Design Engineering, Cairo University, 2011

Masters of Mechanical Design Engineering, Cairo University, 2016

Submitted to the Graduate Faculty of the

Swanson School of Engineering in partial fulfillment

of the requirements for the degree of

Doctor of Philosophy

University of Pittsburgh

2022

UNIVERSITY OF PITTSBURGH

SWANSON SCHOOL OF ENGINEERING

This dissertation was presented

by

Moataz Magdi Mahmoud Amin Abdulhafez

It was defended on

December 10, 2021

and approved by

Mostafa Bedewy, Ph.D, Assistant Professor, Department of Industrial Engineering

Paul Leu, Ph.D, Associate Professor, Department of Industrial Engineering

Bopaya Bidanda, Ph.D, Professor, Department of Industrial Engineering

Sachin Velankar, Ph.D, Professor, Department of Chemical and Petroleum Engineering

Dissertation Director: Mostafa Bedewy, Ph.D, Associate Professor, Department of Industrial Engineering

Laser Processing of Polymers for Controlled Carbonization and Folding

Moataz Magdi Mahmoud Amin Abdulhafez, Ph.D

University of Pittsburgh, 2022

Since the development of lasers, their applications have been continuously growing, and one emerging area of fundamental and applied research focuses on laser processing of polymers. This is due to the transformative potential of laser techniques, which are versatile and reliable methods for rapid and direct-write processing of soft materials to locally modify their geometry, physical and chemical properties. The combined potential of recent developments in polymer science and the commercialization of capable laser processes naturally lend themselves to the emerging area of manufacturing flexible electronics, soft-robotics and flexible neural probes. This powerful combination provides a platform of free form fabrication methodologies that enable both three-dimensional shaping in the millimeter-to-centimeter scale and local synthesis of graphene-related materials in the nanometer-to-micrometer scale. Hence, this thesis research focuses on understanding the fundamentals of such methodologies with specific application to graphene electrode fabrication by direct laser carbonization of polymers, as well as to self-folding of pre-strained polymers by laser-induced viscoelastic relaxation.

Laser carbonization of polymers is an emerging technique that enables directly patterning conductive nanocarbon electrodes directly on polymer films enabling a plethora of flexible devices. These laser-induced nanocarbon (LINC) patterns exhibit hierarchical porous and fibrous graphene-based morphologies. Nevertheless, the fundamental mechanisms underlying the formation of specific LINC morphologies are still missing. In this work, we develop different approaches to investigate these mechanisms through lasing polyimide with spatially controlled

gradients of optical energy flux, combined with imaging and analytical/numerical modeling methods to elucidate the mechanisms of carbonization. From the analysis, we aim to correlate the process parameters to the electrical, electrochemical and surface properties of the nanocarbons.

Light induced bending/folding of specific types of polymers is also a powerful technique for creating complex three-dimensional shapes from either two-dimensional sheets. Of particular interest is inducing self-folding of pre-strained polymer sheets based on the interplay between spatiotemporal thermal gradients and viscoelastic relaxation. In this work, we develop a new approach for controlled self-folding of shape memory polymer sheets based on direct laser processing. Our work aims at understanding and describing the mechanics of folding through experimental and simulation techniques.

Table of Contents

List of Tables

List of Figures

Preface

This work is dedicated to my late grandfather Mostafa Sadek, my biggest supporter and champion in this Ph.D journey.

I would first like to thank my advisor, Prof. Mostafa Bedewy, for giving me the opportunity to pursue my Ph.D. degree at the University of Pittsburgh and for his invaluable guidance and support throughout this journey.

I would also like to thank Prof. Paul Leu, Prof. Sachin Velankar and Prof. Bopaya Bidanda for serving on my thesis committee.

I would like to acknowledge and thank all of the students and staff members that I have worked with, learned from, and become friends with over the years. I'd like to thank current and former NanoProduct Lab members: Prof. Jaegeun Lee, Prof. Ki-Ho Nam, Prof. Se Youn Cho and Ms Golnaz Tomaraei for the useful discussions we had and their help and support. I would also like to thank the staff members who assisted me at University of Pittsburgh: Dr. Susheng Tan, Mike McDonald, Dr. Jun Chen, Dr. Daniel Lamont and Matthew France and Dr. Esta Abelev in the Gertrude E. & John M. Petersen Institute of NanoScience and Engineering. I also would like to thank all of our collaborators, Prof. James McKone, Prof. Tracy Cui, Dr. Elisa Castagnola for their help and support.

I would like to thank all undergraduate students I had the privilege of mentoring at the NanoProduct Lab: Karim Kadry, Angie McComb and Joshua Line. I would also like to acknowledge my wonderful colleagues at the Department of Industrial Engineering, especially my office mates Shadi Sanoubar, Tarik Bilgic, Arnab Bhattacharya, David Abdul-Malak and Moataz

Elsisy for being great friends. I would like to express my sincere gratitude to all the friends here in Pittsburgh and Tartan Salsa at CMU for being my family away from home.

I am eternally grateful for the love and endless support of my parents and my brother, for being an endless source of love, inspiration, and motivation. And finally, Nora, my lovely wife, for her never-ending patience, support and faith in me.

1.0 Introduction

1.1 Laser Polymer Processing

Polymers and lasers are ubiquitous in the modern age. Since their inception in the last century, both have demonstrated continuous development thanks to their versatility as a material and a process. Both constitute an essential part of modern manufacturing with lasers enabling localized energy delivery and polymers demonstrating tunability, durability and mechanical flexibility. Combining the flexibility of polymers as a material and lasers as a processing technology allows for a plethora of processes that could potentially be combined easily in a single platform. Emerging applications that benefit from the synergy between both lasers and polymers are the areas of flexible electronics and soft robotics both of which fundamentally require mechanical flexibility and functionality at different length scales.[1–6]

Laser processing of polymers enables the geometrical, chemical and physical modification of polymers as listed in Figure 1. Geometrical modification of existing polymer can be accomplished through laser etching and cutting of polymer sheets, or 3D modification through inducing self-folding of the polymer with light stimulus. Chemical and physical changes can also be induced. Laser heating of polymers can carbonize the material into conductive graphitic material

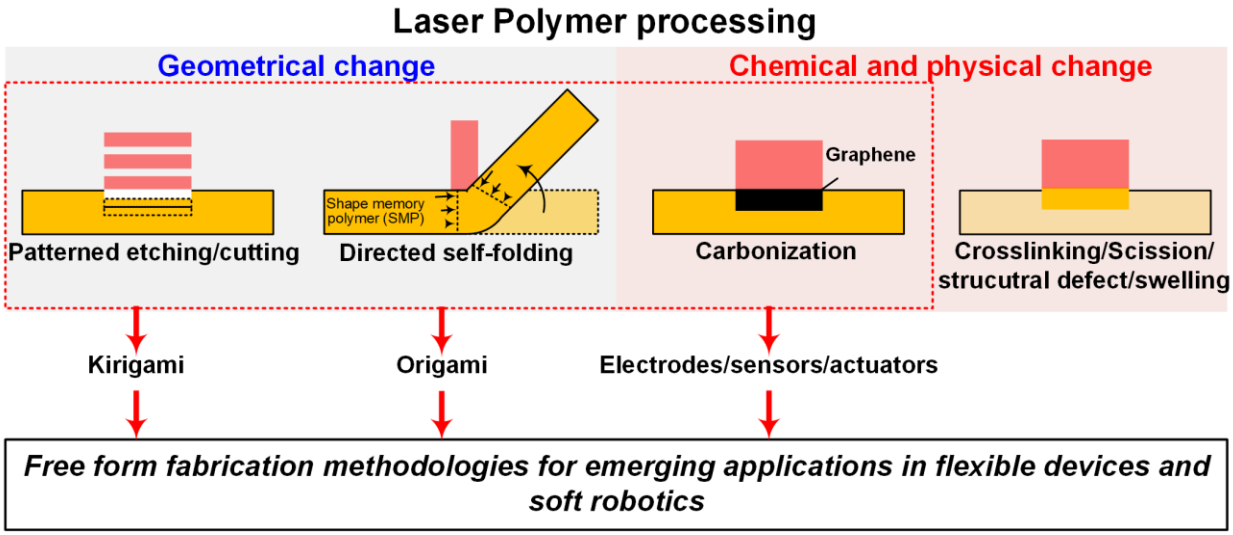

Figure 1: Laser polymer processes

Additionally, lasers can also induce physical and chemical changes through crosslinking, scission, swelling of the starting material to shape, functionalize or change its properties and support subsequent processing. Combined, these processing tools present a set of free form fabrication methodologies that directly support the development of flexible device and soft robotic applications[1–6] as illustrated in the examples in Figure 2. For example, laser carbonization is capable of directly writing electrochemically sensitive conductive electrodes on flexible polymers for sensing, energy storage and actuation applications. The patterned etching and cutting allows creating the 3D shapes; a frame for any flexible device or robot. The successful utilization of this framework hinges on fully understanding these processes and how the lasing condition affects the resulting properties of the end product. Hence, in this thesis, we examine a subset of these processes: *directed self-folding of shape memory polymers and laser induced carbonization*, with the objective of understanding the fundamentals behind the processes in order facilitate its translation into applications.

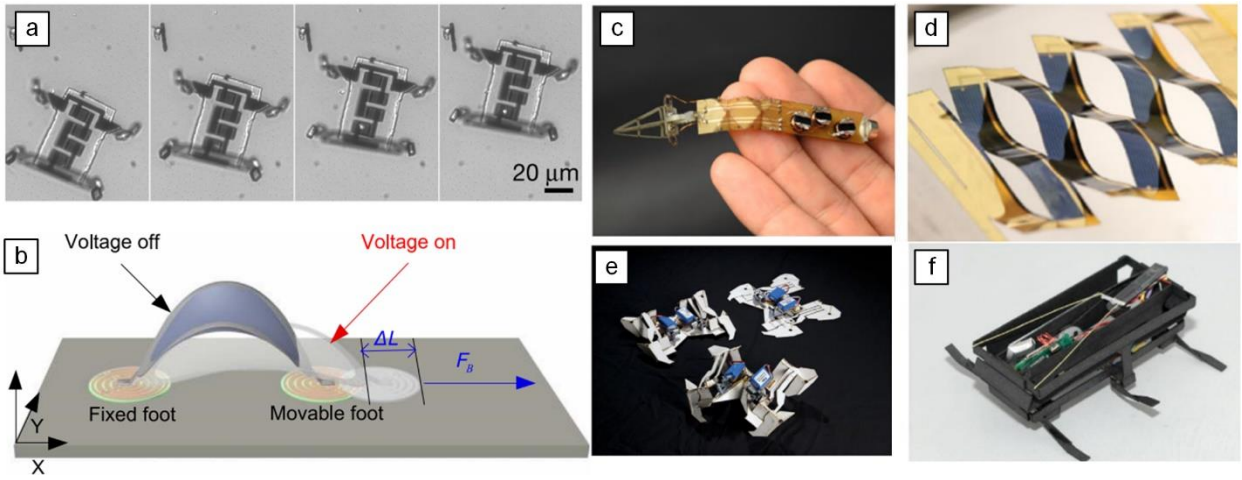

Figure 2: Applications of origami/bio-inspired flexible robots at different scales (a) Microrobots with flexible legs for motion.[7] (b) Soft wall-climbing robot.[4] (c) Flexible wireless gripper for medical applications.[1] (d) Actuated solar tracking device with flexible Kirigami solar panels.[8] (e) self-assembling folding robot for search and rescue.[9] (f) legged robot utilizing flexible legs.[2]

1.2 Directed Self-folding of Shape Memory Polymers

1.2.1 Shape Memory Effect

Directed self-folding of 2D stock materials to create complex 3D geometries is an attractive pathway toward manufacturing functional structures at different length scales. This origami-based approach of self-folding is observed in nature at different length scales ranging from nanometers to meters. Organic molecules[10], insects [11], brain tissue [12], and tree leaves [13] are all observed to use folding techniques for producing 3D structures that underlie their function. Similarly, engineered origami and nature inspired foldable structures have found applications in areas like robotics [9], implantable devices [14], sensors, actuator [14], aerospace [15] and battery development [16].

The main element of a self-folding technique is the used material which has to exhibit a change in geometry as a response to a stimulus like light [17–19], heat [7,9,20], surface tension [21]. The accumulation of such spatially varying responses to stimuli results in controlled folding at desired locations. Polymers are ideal as a self-folding material since they can be durable, low-cost, lightweight, bio-compatible, and can be designed to be stimulus responsive, such as in the case of shape memory polymers (SMP). A polymer can be programed by pre-straining at high temperature, followed by cooling below the glass transition temperature. Hence, pre-strained polymer sheets are a widely used material in self-folding research since they are a low cost and versatile material to induce self-folding from the macroscale to the microscale. When heated, localized thermal gradients in the material lead to a shrinkage across the thickness of the sheet which induces instant folding in the sheet [19,20,22].

Different methods have been proposed in literature to induce folding stimuli of both non-SMP sheets and SMP sheets, including focused or unfocused light radiation [17–19], heat conduction through resistive wires [7,9,20], microwave irradiation [23], uniform by ovens or air guns [22,24] and surface tension [21] as illustrated in Figure 3. In addition to differences in stimuli and heating method, techniques can also differ based on whether the folds are made in a sequential or a simultaneous manner. Liu et al. [19] initially demonstrated the self-folding of pre-strained films by using local light absorption generated from an unfocused IR light bulb that heats pre-defined hinges patterned by desktop printing. Recently, Lee [25,26] has developed a technique using curvilinear strain engineering to create complex 3D geometries and curvatures from 2D inked polymer sheets, subject to unfocused light. Felton et al. [22] developed a method where composites of pre-strained polymer hinges bonded to paper are activated to fold by joule heating via resistive circuits at the hinges. Elsisy et al. [7,20] developed a technique using resistive heating

ribbons to locally heat the pre-strained polymer sheets and demonstrated that changing the composite layer combination can be utilized to control the direction of hinge fold in the structure. Another non-contact technique developed utilizes microwave absorbing ink [23] to define the hinges on microwave transparent pre-strained polymer. When the sheet is subject to microwaves, the ink patterns heat up remotely, leading to hinge folding. To demonstrate selective sequential folding using unfocused light, Liu et al. [18] used printed ink of different colors to define the hinges on the surface of the polymer sheets. This enabled controlling the amount of absorbed light based on the wavelength of the used light and the color of the ink, hence achieving selective folding. In addition to self-folding using unfocused light, direct local heating of the pre-strained films has also been demonstrated using laser to induce folding [27] by focusing a continuous-wave laser with an elongated beam shape using a cylindrical lens. In that method however, the shaped laser spot is fixed and is wider than the used polymer strip as illustrated in Figure 3. Indirect laser heating was also demonstrated in which the laser was used to heat the sample substrate instead of the sample itself [28]. Here, we investigate a scalable approach for controlled self-folding of shape memory polymers based on laser rastering. Localized heating is achieved by moving laser to deliver controlled energy across the rastering path. This is in contrast to prior work on using a stationary laser spot with a rectangular shape described earlier as illustrated in Figure 3. Our approach allows the accurate control of the spatiotemporal delivery of heat as a function of laser power, speed and number of passes along designed paths on the polymer, which enables control of fold angle and quality. This approach can potentially be used to create complex three-dimensional shapes and it paves the way for developing unique manufacturing capabilities in creating functional parts that require complex 3D geometries and high surface quality.

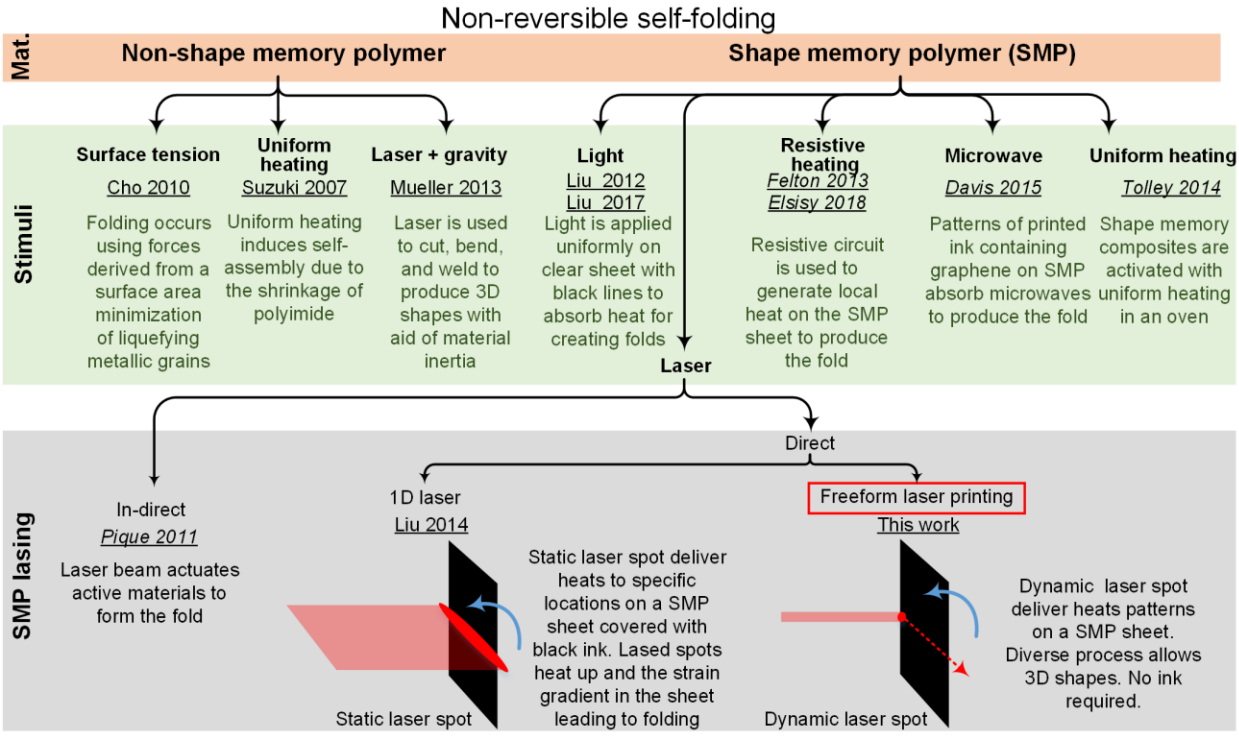

Figure 3: Illustration of different methods of inducing self-folding of polymers based on external stimuli [9,17,29,18–24,28], highlighting the unique freeform direct-write capability of our new approach.

1.3 Laser Carbonization of Polymers

The use of lasers to locally carbonize commercial polymers, such as polyimide, is an emerging technique for the fabrication of functional graphenic nanocarbons directly on flexible substrates.[30–35] This direct-write approach is a powerful alternative to printing technologies, which use nanocarbon-containing inks to print conducting electrodes of carbon nanotubes or graphene in flexible device fabrication.[36,37] In fact, before the recent interest in flexible electronics, laser processing of polymers (especially polyimide) was first studied in the context of polymer ablation using UV pulsed lasers.[38] However, in addition to the dissociation of its polymeric structure, carbonization and enhanced conductivity were observed using both

pulsed[39–42] and continuous wave (CW)[43,44] UV lasers, as well as pulsed [42,45,46] and CW visible light[47,48] lasers.

Accordingly, micron-scale conductive electrodes were fabricated on polyimide for electrochemical and electronic devices.[40,43] The resulting electrodes can be porous, conductive, and electrochemically active and have tunable surface properties and are directly written on a flexible substrate. These properties make it an ideal material for sensor, energy storage and flexible device applications.

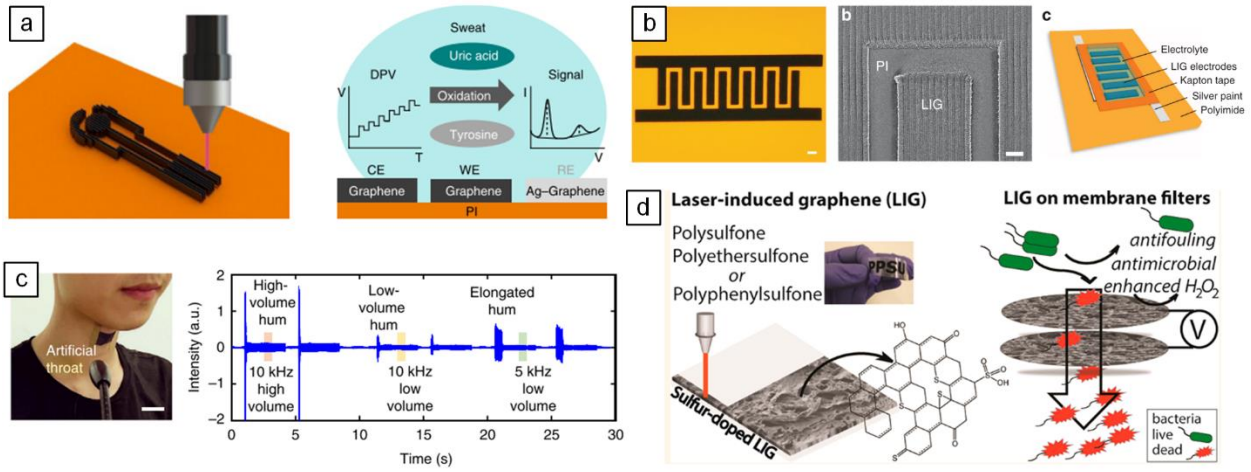

Figure 4: Figure illustrating different LINC applications on polymers.[49] (a) Wearable sensor for sensitive detection of uric acid and tyrosine in sweat. (b) LINC based super microcapacitors for energy storage.[30] (c) An artificial throat utilizing LINC.[50] (d) Antifouling membrane filter made from doped LINC.[51]

More recently, it was reported that rastering a CW CO_2 laser in air creates patterns of porous graphene-based structures on polyimide.[30] Importantly, these conductive patterns were used to develop a plethora of devices including micro supercapacitors,[31] strain or piezoresistive sensors,[52,53] multifunctional strain sensors,[54] pH sensors,[52] gas sensors,[55] flexible electrodes,[56] anti-fouling surfaces,[57] wearable sensors,[49] artificial throat,[50] microfluidic

devices,[58] and heating elements[59], some of which are listed in Figure 4. Owing to the diversity of morphologies achievable by laser carbonization, here we use the term laser-induced nanocarbon (LINC), as a more general term than laser-induced graphene to collectively refer to all nanostructured carbon materials fabricated by laser irradiation of polymer precursors. The process of LINC formation is still not fully clear due to the complexity of the laser-polymer interactions and how the lasing conditions (speed, power, fluence, flux…etc.), laser wavelength, fluence and lasing kinetics affect the resulting graphene/carbon. Hence, it is an objective of this research to help understand the process-structure-property relationships of the process.

2.0 Research Scope and Objectives

As discussed in the previous chapter, we are investigating the processes: *directed self-folding of shape memory polymers and laser-induced carbonization.* In this chapter, we will be outlining the main research questions and objectives of the research.

2.1 Laser-Induced NanoCarbon (LINC) Formation

A key challenge is to understand the process-structure-property relationships for LINC formation. We pose the following questions:

- How does laser condition (wavelength, power, speed, pulse rate, etc.) affect the resulting LINC morphology?
- How does the morphology and chemical composition of LINCs affect their properties suc h as electrical conductivity and electrochemical behavior?
- How does the kinetics of laser heating affect the carbonization process?

While the morphology of LINC is generally described in literature as porous, there are reports indicating that LINC's morphological structure can be tuned with varying laser parameters.[60,61] In particular, it was observed that increasing laser-induced thermal damage can result in fibrous[62] or porous formations [43] in pulsed laser irradiation of polyimides. Using CO_2 lasers, Lamberti *et al.* reported that by varying the scan speed of the laser and the pulse width modulation (PWM) frequency, different morphologies of LINC were observed that were described as "sheets", "needles" and "porous" morphologies.[61] However, the precise mapping of laser conditions that lead to these differences in terms of universally recognizable physical quantities

such as laser fluence is still largely missing. Moreover, identifying the transition thresholds between these morphologies has been challenging, because previous work has relied on discrete experiments exploring the large parameter space,[63] owing to the lack of facile approaches that can enable applying continuous gradients of laser parameters on the same sample. Additionally, no work currently exists that focuses on how the kinetics of the process affect the carbonization process. How does the heating rate affect the resulting LINC? Can the density of LINC be controlled by controlling speed?

To address some of the these questions, we develop experiments to leverage laser fluence gradients and beam defocus to facilitate understanding of the LINC formation process by quantitatively correlating laser condition, the resulting LINC morphologies, and their varying electrical conductivity. Additionally, we describe methods of creating LINC materials with spatially varying morphologies and hence spatially varying properties. In particular, to investigate the effect of tuning fluence on morphology and properties, we uniquely combine mathematical modeling of Gaussian laser beams with two experimental approaches to control the local spread of the beam: 1) lasing individual lines on a tilted polyimide surface to achieve controlled gradients of fluence, and 2) lasing untilted samples at different degrees of defocusing for spatially uniform LINC lines. The first approach enable studying the evolution of nanoscale morphology and atomic structure continuously at different fluence values on the same polyimide film. Thus, we can precisely identify fluence thresholds for transition between different LINC morphologies owing to the resulting spatial map of fluence along a single LINC line in the tilted experiments. Based on our findings, outlined in Chapter 3.0, we propose a model for the morphological evolution during laser carbonization that results in nanoporous structures, cellular networks, and woolly fibers at different fluence values, which enables delineating a clear morphology diagram. We also correlate

these results with electrical conductivity measurements in order to reveal the process-structure-property relationships governing the design of LINC materials with tunable and spatially varying properties.

In Chapter 4.0, we focus on understanding the kinetics of the process and how lasing speed affects the result LINC morphology and properties. This is achieved by developing experiments and thermal models to investigate the effect of heating rates on the resulting LINC in terms of molecular structure and morphology. Chapter 5.0 focuses on optimizing the electrical and electrochemical properties for functional application development through exploring methods to improve the electrical conductivity and electrochemical sensitivity of LINC based electrodes.

2.2 Directed Laser Self-Folding

Here, we propose a scalable approach for controlled self-folding of shape memory polymers based on laser rastering. The objective can be summarized through the following hypothesis:

Direct write laser scanning of shape memory polymers (SMPs) under optimized laser conditions can generate repeatable high quality straight folds which can be used to generate 3D geometries of the polymer.

To test this hypothesis, we designed a number of experiments where localized heating is achieved by moving laser (40W, CO2, 10.6 μm) to deliver controlled energy across the rastering path. Our approach allows the accurate control of the spatiotemporal delivery of heat as a function of laser power, speed and number of passes along designed paths on the polymer, which enables control of fold angle and quality. This work paves the way for developing unique manufacturing

capabilities in creating functional parts that require complex 3D geometries and high surface quality. Additionally, to further understand how the lasing condition affects the viscoelastic relaxation and hence the folding kinetics we develop a multi-physics model, coupling the mechanical and thermal effects, and monitoring the change in strain rates and displacements. These findings are presented in Chapter 6.0.

The rest of the work is arranged as follows,

- Chapter 7.0 will discuss ongoing and future research directions.
- Finally, Chapter 8.0 will discuss the conclusions of this thesis, list of papers as first author or co-author.

3.0 Fluence-dependent Morphological Transitions in Laser-induced Formation of Graphene-based Conducting Electrodes Directly On Polymers for Flexible Devices

3.1 Introduction

In this chapter, we leverage laser fluence gradients and beam defocus to facilitate understanding LINC formation process by quantitatively correlating laser condition, the resulting LINC morphologies, and their varying electrical conductivity. Additionally, we describe methods of creating LINC materials with spatially varying morphologies and hence spatially varying properties. In particular, to investigate the effect of tuning fluence on morphology and properties, we uniquely combine mathematical modeling of Gaussian laser beams with two experimental approaches to control the local spread of the beam: 1) lasing individual lines on a tilted polyimide surface to achieve controlled gradients of fluence, and 2) lasing untilted samples at different degrees of defocusing for spatially uniform LINC lines. The first approach enables studying the evolution of nanoscale morphology and atomic structure continuously at different fluence values on the same polyimide film. Thus, we can precisely identify fluence thresholds for transition between different LINC morphologies owing to the resulting spatial map of fluence along a single LINC line in the tilted experiments. Based on our findings, we propose a model for the morphological evolution during laser carbonization that results in nanoporous structures, cellular networks, and woolly fibers at different fluence values, which enables delineating a clear morphology diagram. We also correlate these results with electrical conductivity measurements in order to reveal the process-structure-property relationships governing the design of LINC materials with tunable and spatially varying properties.

3.2 Materials and Methods

Polyimide tape (TAPECASE 2B, Cat. No. 15C616, tape thickness: 88.9 microns) was used as a substrate precursor for LINC formation experiments. To prepare for the experiments, the tape was place on silicon wafers, rinsed with acetone then Isopropyl alcohol for sample surface cleaning.

Direct laser irradiation on the polyimide sheets was conducted in air using a CO_2 laser cutter/engraver system (Full Spectrum Laser Pro-Series 20×12, 1.5 inch focus lens) with 10.6 μm wavelength and 45 W power. The system allows tuning the power by controlling the laser current. We measure the laser power at different currents using a CO_2 laser power meter (HLP-200, Changchun Laser Optoelectronics Technology Co., Ltd.). The beam radius was measured based on ($1/e^2$) of the maximum intensity (w_y, w_x) at different distances (z) from the beam waist using the knife-edge method.[64] Using this technique, the beam radius at the beam waist (w_{ox}, w_{oy}), based on a Gaussian beam assumption, was determined to be 125.8 μm in the x-direction and 84 μm in the y-direction.

The laser objective lens is mounted on a motorized XY stage with a maximum speed of 500 mm/s in the X-direction. The beam spot size was controlled by adjusting the vertical distance (z) between the sample position and the beam waist; i.e. by moving the sample stage vertically with respect the objective lens. Laser power (P) was varied from 11.7 W to 30.7 W, and all experiments were performed at X-direction speed (v) of 500 mm/s and under ambient conditions.

3.3 Area-averaged Fluence Model

The beam is modeled as a non-astigmatic elliptical Gaussian beam. The beam intensity is modeled using the following relationship (as illustrated in Figure 5(a))[65,66]:

$$I(x,y,z) = I_o e^{-2\left(\left(\frac{x}{w_x(z)}\right)^2+\left(\frac{y}{w_{y(z)}}\right)^2\right)}\left[\frac{W}{m^2}\right] \quad (3\text{-}1)$$

where x and y are measured from beam center axis at distance z from the beam waist. Beam dimensions at defocusing level (z) are w_x and w_y (as illustrated in Figure 5(d)) based on $1/e^2$, and I_o is the maximum intensity.

Beam total power delivered at a spot with z vertical distance from the beam waist (estimated using thermopile measurements) is equal to the integration of the intensity over the laser spot in the horizontal plane (normal to the beam center axis), assuming complete absorption of the laser beam energy:

$$P = I_o \int_{-\infty}^{\infty}\int e^{-2\left(\frac{x}{w_x}\right)^2} e^{-2\left(\frac{y}{w_y}\right)^2} dxdy \approx \frac{\pi}{2} I_o w_x w_y \quad (3\text{-}2)$$

where w_x and w_y are the $(1/e^2)$ beam size.

This integration approximately gives the value of the maximum intensity:

$$I_o(z) \approx \frac{2P}{\pi w_x(z) w_y(z)} \quad (3\text{-}3)$$

where P is constant for different z's, however the w_x and w_y change.

The Gaussian beam size at different z values is estimated using the following equations (assuming the beam spot major and minor axis is aligned with the lasing direction x and y):

$$w_x(z) = w_{ox}\sqrt{1+\left(\frac{M_x^2 \lambda z}{\pi w_{ox}^2}\right)^2} \quad (3\text{-}4)$$

$$w_y(z) = w_{oy}\sqrt{1 + \left(\frac{M_y^2 \lambda z}{\pi w_{oy}^2}\right)^2} \tag{3-5}$$

where M_x^2 and M_y^2 are the beam quality factor for the x and y direction respectively, w_{ox} and w_{oy} are the beam waist dimensions (as illustrated in Figure 5(a)). These parameters are estimated using the knife edge method as described in the supplementary information.

The average flux I_{av} is estimated at a certain spot size for a laser power P, by averaging the intensity I(z) over the spot area A(z):

$$I_{av}(z) = \frac{\int_{-w_x(z)}^{w_x(z)} \int_{w_{y(z)}}^{w_y(z)} I(x,y,z)dydx}{A(z)} = \frac{I_o}{\pi w_x(z) w_y(z)} \int_{-w_x(z)}^{w_x\,(z)} \int_{-w_y(z)}^{w_y(z)} e^{-2\left(\frac{x}{w_x(z)}\right)^2} e^{-2\left(\frac{y}{w_y(z)}\right)^2} dxdy \tag{3-6}$$

The average fluence F is then estimated using the following relationship:

$$F_{Aavg}(z,v) = D(z,v) I_{av}(z) \tag{3-7}$$

where D(z,v) is the dwell time of the laser beam over a spot. The dwell time is estimated by dividing the beam length in the lasing direction x by the beam speed v. [67]

$$D(z,v) = \frac{2w_x(z)}{v} \tag{3-8}$$

The average fluence of the beam on a tilted surface was shown to be approximately equal to the untilted surface average fluence for our ranges of the tilting angle γ.

3.4 Tunable Beam Intensity for Patterning Graphitic LINC on Polyimide

LINCs form due to the local interaction of a laser beam with the surface of polyimide. As shown schematically in Figure 5 (a), a continuous beam with power P is scanned across the polyimide film at a speed v with the sample surface at a distance z from the beam waist. Photothermal interactions from the radiation absorption by the polyimide drive a rapid temperature increase that carbonizes polyimide locally at the moving laser spot to create a pattern, as depicted in Figure 5 (b). Depending on the lasing parameters, the polyimide can be carbonized into nanoscale graphene-rich domains, as shown from X-ray diffraction (XRD) results in Figure 5 (c). These results were generated for individual LINC lines, which are formed at power P = 28 W, speed v = 500 mm/s, and distance from beam waist z = 0 mm. From XRD, we can clearly identify the (002) and (100) peaks that are characteristic of highly ordered sp^2-hybridized graphitic carbon. The laser beam profile of the CW CO_2 laser used in this study is depicted in Figure 5 (d), estimated from beam characterization experiments. CW CO_2 lasers are used for LINC applications primarily because polyimide has high absorptivity for the infrared (IR) range around the wavelength of CO_2 laser (λ=10.6 μm) and hence carbonizes relatively easily.[68] Moreover, CO_2 laser systems are commercially available at low cost, which paves the way for widespread adoption of this approach for fabrication of functional electrodes on flexible devices. Beam power and profile measurements are used to estimate the laser intensity profile at the different z values at different spot sizes and powers.

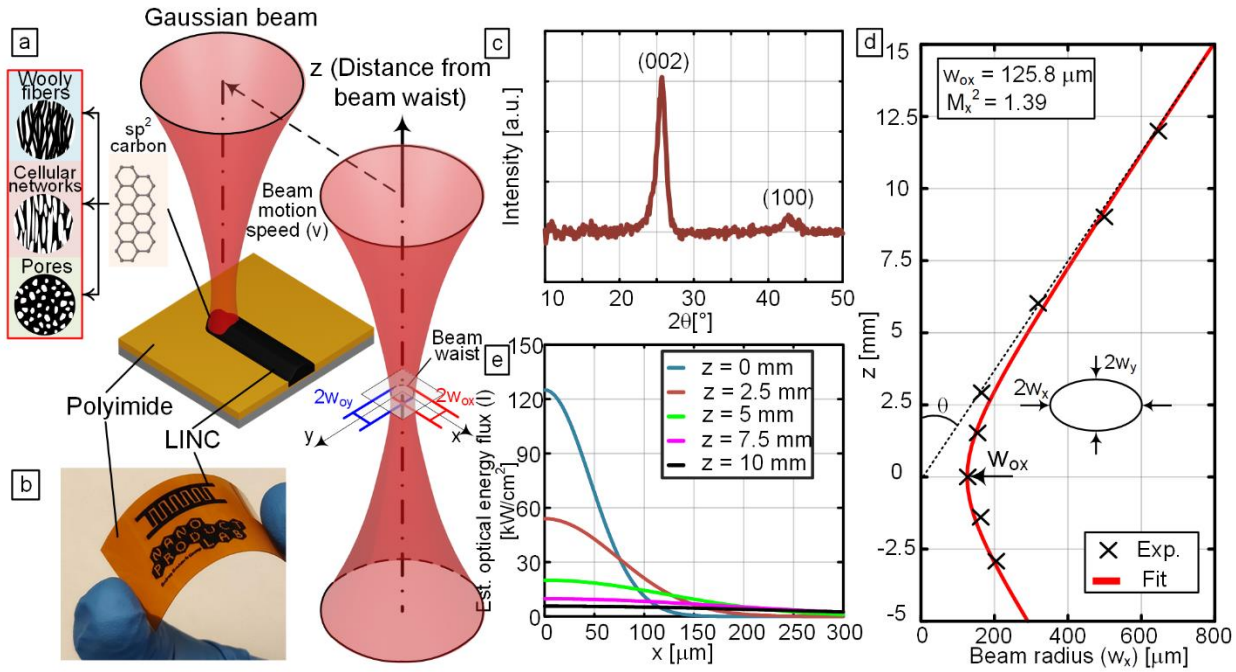

Figure 5: (a) Schematic of lasing flat untilted polyimide to produce a LINC line with a Gaussian beam. (b) Photograph of a 2D LINC pattern on a flexible polyimide substrate. (c) XRD of powdered LINC lased at *P* = 28 W, *v* = 500 mm/s, *z* = 0 mm). (d) Experimental points representing the estimated laser beam profile along the lasing direction x using the knife edge technique, along with the profile of the fitted Gaussian beam illustrating the divergence of the beam away from the beam waist. The resulting beam spot in the x direction is estimated to be $2w_{ox}$ = 251.6 μm. (e) Estimated optical flux along the x direction at constant power (*P* = 22.5 W), showing the change of beam intensity with *z* (i.e. with changing spot size by defocusing the beam).

An example is shown in Figure 5 (e) which shows the change of intensity across the beam for different *z* values at the same laser power. At different *z* values, the beam intensity I(x,y) follows a Gaussian distribution with the narrowest distribution featuring the overall maximum value of intensity at the beam waist where *z* = 0 mm. Changing both the speed and the spot size changes the dwell time of the laser spot,[67] which corresponds to how long a point is exposed to the moving laser beam. Naturally, faster speeds reduce the dwell time. At a fixed speed however, the dwell time also decreases with decreasing spot size. The relationship between the beam dwell

time and laser intensity controls the value of the average fluence (estimated using the Gaussian beam model), which would in turn influence the temperature increase at a point.

3.5 Fluence Gradients for Spatial Control of LINC Morphology

To investigate the influence of beam intensity and fluence on polyimide carbonization, we create a gradient of fluence by lasing a tilted sample of polyimide. This tilt angle controls how different points on the substrate along the laser path experience different fluence levels. A schematic of the experiment is shown in Figure 6 (a), where the sample is lased at an angle (γ = 45°). While the laser beam moves in a horizontal direction x at a speed *v*, the sample is tilted along the x' direction with angle γ between x and x'. Since the spot size changes with z, the beam maximum intensity, average fluence and dwell time also change along the x' direction (i.e. along the lased lines in the sample's plane). Tilting the axis normal to the sample (Z') with respect to the beam axis (*Z*) by γ changes the distribution of beam intensity and transforms the geometry of the beam spot. We demonstrated that the average fluence value for the untilted case is approximately equal to the tilted case for our values of beam parameters. This can be explained by the fact that the tilt angle doesn't drastically change the laser beam intensity profile, and that while the beam broadens, so does the beam spot. Hence, averaging over the area doesn't affect the averaged intensity over the spot when comparing the untilted to the tilted case.

The sample is lased at different powers ranging from P = 11.7 W to P = 30.7 W at a constant beam scanning velocity v = 500 mm/s with the resulting lased lines shown in Figure 6 (b). Since, each point on the line represents a different average fluence value, the lines with gradient fluence uniquely enables mapping the fluence-dependent morphological evolution. Close to the edges of

the visible lines, swelling of the polyimide is observed. Towards the center of the lines, carbonization is visible, and in some cases the formation of fuzzy/woolly fibers at the center was observed where fluence is highest. The length of the carbonized portion of the line where LINC is formed (black portion) increases with increasing *P*, which can be explained by shifts in the location, at which the threshold fluence for carbonization (estimated to be in the range of 5-8 J/cm^2) is reached, referred to here as transition T0.

More discrete transitions of LINC morphology along the lines are identified under both optical microscopy and scanning electron microscopy (SEM) imaging, as shown in Figure 6 (c, d). The first type of transition (T1) observed is from a porous morphology to a cellular network morphology, which is accompanied by a stark change in reflectivity as noticed in the optical images Figure 6 (d).

The second type of transition (T2) observed is an abrupt transition from the cellular networks to a large volume woolly fibrous formation. This second transition was only observed at powers larger than P = 18.4 W. The distance between the midpoint of the lines and the points of transition along the x' direction are plotted in Figure 6 (e). The transitions (T1 and T2) are mapped with the average fluence estimated at the different powers and x' values according to our beam model presented in the Methods section. The plot indicates that the transitions occur at fixed average fluence values, which is a useful insight that we will build on later for creating a morphology diagram.

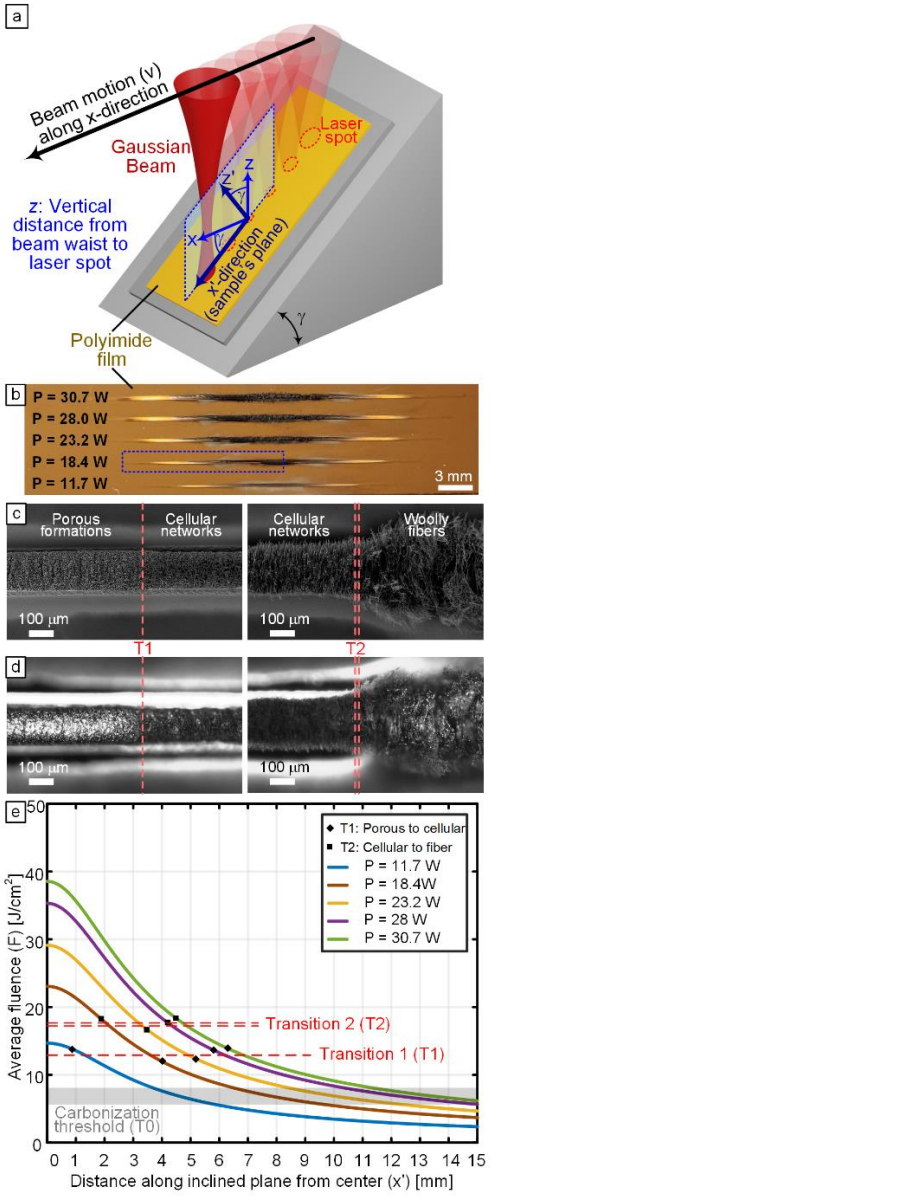

Figure 6: (a) Schematic of setup for LINC formed with gradient fluence by lasing tilted polyimide at an angle γ. The lines are lased along the x' in the sample's plane, while the beam moves along x direction with speed v. (b) Optical photograph of the different lines lased at different powers using the method described in (a) at γ=45°, showing the different color changes along the lased lines and the change of the location of the transition of LINC morphology as a function of powers. (c) SEM image of the two transitions from porous to cellular networks (T1) and from cellular networks to woolly fibers (T2) lased at power P = 18.4 W. (d) Optical microscopy images at the same points showing the change in line reflectivity for both transitions and abrupt formation of woolly fibers. (e) Plot of estimated fluence delivered at different powers and v = 500 mm/s vs. the

distance from LINC line center in the x' direction. Locations of transitions T1 and T2 are marked with black diamond and square markers on the curves, respectively, showing that the transitions occur at similar fluence values around FT1= 12 J/cm^2 and FT2=17 J/cm^2 (horizontal red lines of constant fluence). Horizontal grey band 5-8 J/cm^2 represents the estimated carbonization threshold.

The porous formation to cellular formation transition (T1 in Figure 6 (e)) occurs at an estimated average fluence value of ≈12 J/cm^2. The transition from cellular network to woolly fiber formations occurs at an estimated average fluence value of around ≈17 J/cm^2. It is also observed that while there is a porous to cellular network transition (T1) when the lasing power was P =11.7 W, there is no network to fibers transition (T2) at this low power. This indicates that the fluence threshold for woolly fiber formation is higher than peak fluence in the center of the line at this power, which highlights the utility of our fluence-based mapping approach and our beam modeling. In addition to the fluence driven transitions, the resulting woolly fibers at the point of highest fluence (center of the lines) become more voluminous and wider with increasing power.

3.6 Structural Changes Concomitant with LINC Morphology Evolution

To correlate the observed morphologies from the tilted lasing experiment to the molecular structure of LINC, Raman spectroscopy mapping was carried out along the lased lines for two power values, P = 11.7 W (does not have woolly fibers at the center of the line) and P = 18.4 W (has woolly fibers at the center of the line), as shown in Figure 7 and Figure 8. Raman spectra for different points along the lased line are shown in Figure 7 (a) and Figure 8 (a), and top view SEM images of the lines are shown Figure 7 (b-j) and Figure 8 (b-j). For a comprehensive understanding of the evolution along the centimeters-long line, we stitched SEM images going from the edge of the line

to its center in Figure 7 (b) and Figure 8 (b). Also, we present higher resolution SEMs of selected points along the line in Figure 7 (c-j) and Figure 8 (c-j).

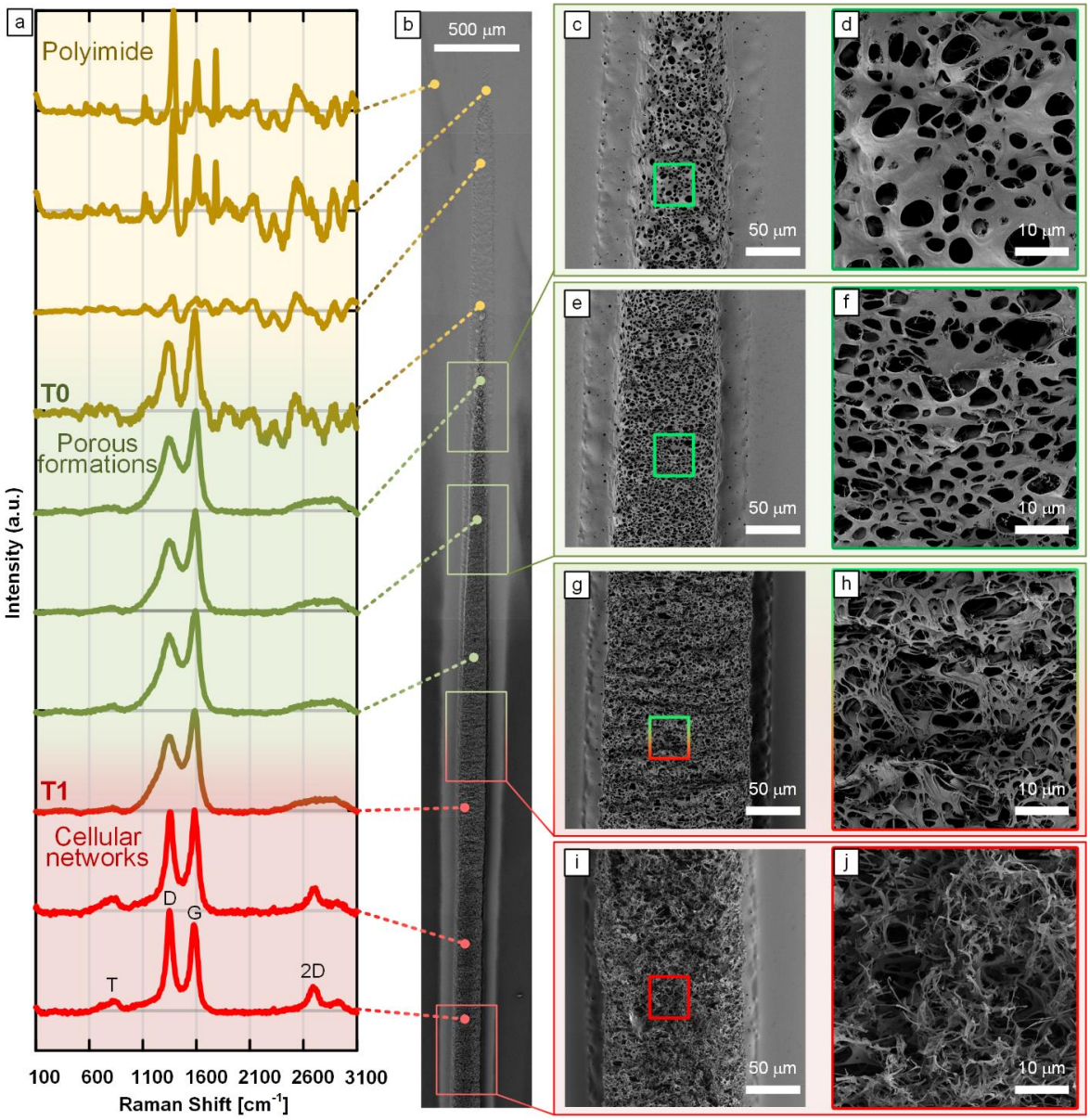

Figure 7: (a) Raman spectra of different points along the LINC line generated from tilted lasing at γ = 45°, power P =11.7 W and speed v = 500 mm/s, showing the carbonization transition from polyimide to porous LINC (T0) as well the transition from isotropic porous LINC to cellular networks (T1). (b) Stitched SEM images of lased line. (c-j) SEM images along the line illustrating the different morphologies.

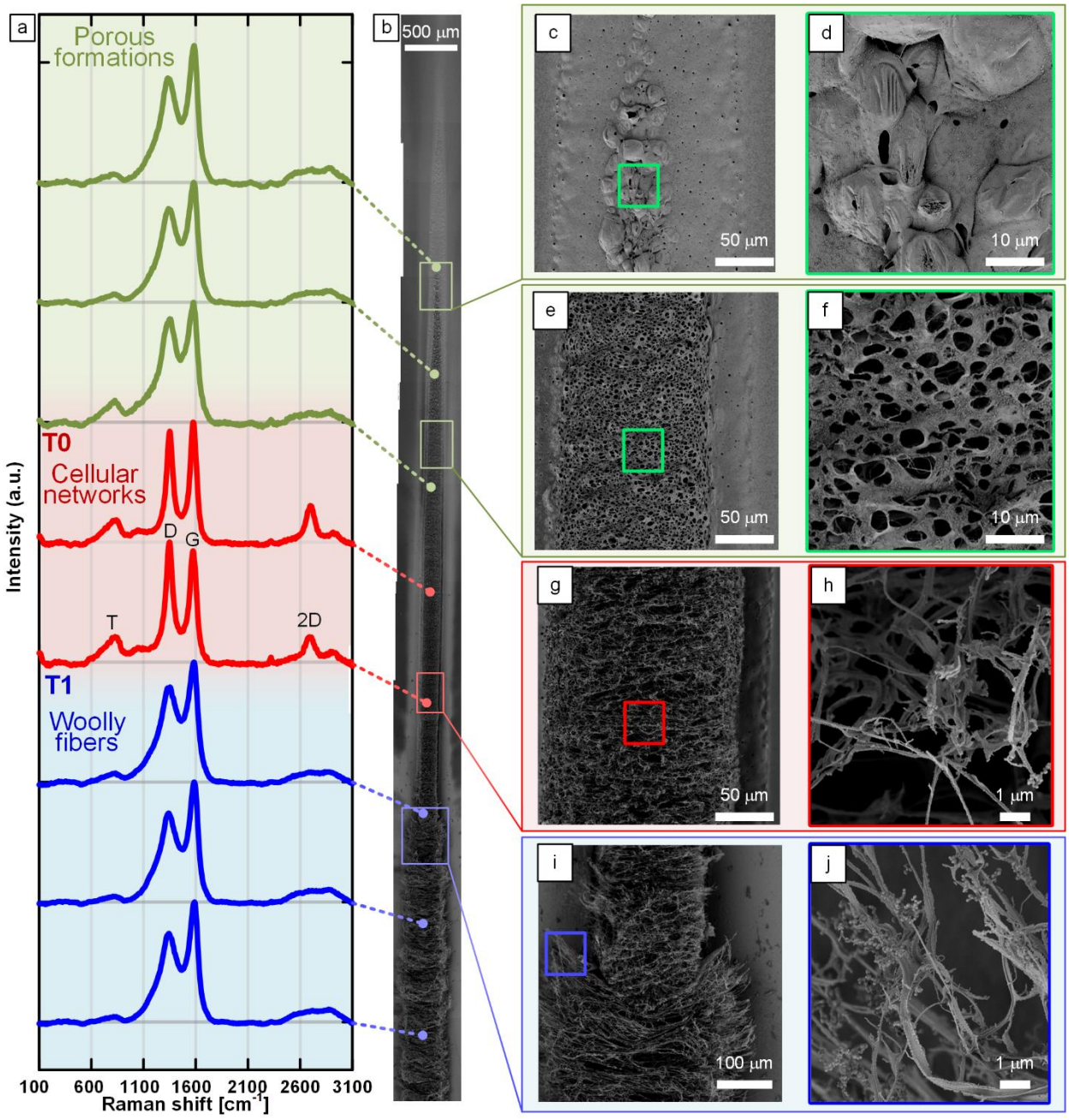

Figure 8: (a) Raman spectra of different points along the LINC line generated from tilted lasing at γ = 45°, power P = 18.4 W and speed v = 500 mm/s, showing the transition from isotropic porous LINC to cellular networks (T1), as well as the transition to woolly fibers (T2). (b) Stitched SEM images of lased line. (c-j) SEM images along the line illustrating the different morphologies.

The Raman spectra at points towards the edge of the lines prior to the formation of porous LINC display the characteristic peaks of polyimide at a Raman shift of 1395 cm^{-1},1601 cm^{-1} and 1786 cm^{-1} associated with C-N-C axial vibration, imide ring vibration and C=O asymmetric ring respectively. (The background signal due to polyimide fluorescence is removed).[45] Moving along the line with increasing average fluence, the Raman peaks associated with polyimide disappear and the G and D bands characteristic of graphenic nanocarbon appear, indicating the progression of carbonization after T0. The observed spectra exhibit G and D peaks with large full width at half maximum (FWHM) and broadband band around the 2D peak. The spectra have the same shape along the lased line until a stark change in shape is observed beyond the T1 transition. In particular, a sharper well-defined 2D band appears, accompanied by a marked decrease in G and D peak FWHM (from 150 cm^{-1} to around 75 cm^{-1} for the G peak), as shown in Figure 7 (a). The decrease of FWHM of the G peak indicates larger sp^2 grains.[69] Hence, these changes suggest the formation of well-defined graphene domains concomitant with the transition from isotropic porous morphology to more anisotropic (as will be shown later in Figure 9 from side-view SEMs) cellular networks of 3D graphene, as shown in the difference between Figure 7 (f) and (j). A small peak is observed in the Raman spectra at 850 cm^{-1}, which was reported previously for laser carbonization of polyimide with a UV laser.[43] This peak is consistent with the T band representing sp^3 vibration density of states,[70,71] which was previously shown in *ab initio* calculations of Raman spectra.[72]

Similar analysis is performed for the lased line at P = 18.4 W (Figure 8), showing the same transitions take place at higher power. In this case however, three morphologies are observed with both transitions T1 and T2 identifiable in Raman measurements and SEMs. At the T2 threshold, an abrupt transition into woolly fibrous morphology is observed ((Figure 8 (i) and (j)), which was

not seen in the low-power (P = 11.7 W) results shown in Figure 7. Interestingly, the voluminous woolly fibers exhibit similar Raman spectra to the isotropic porous LINC that form between T0 and T1, with no sharp 2D peak and larger FWHM for the G peak compared to the anisotropic cellular networks that form between T1 and T2. These results suggest that the fibrous LINC formed beyond T2 generally has lower-quality sp^2 carbon than the anisotropic cellular networked structure formed between T1 and T2. This is crucial for tailoring the properties of LINC patterns, as will be shown for electrical conductivity measurements below.

3.7 Fluence-dependent Tunability of LINC Morphology

To gain more insight into the obtained LINC morphologies, untilted polyimide films are lased at different z values for the same power P = 18.4 W to change the average fluence values. SEM images of the side view of the films along the direction of lasing are shown in Figure 9 (a-i), with high-resolution images shown in Figure 9 (j-o). The images at the different levels of defocusing elaborate the evolution of the morphology with increasing average fluence (largest at z = 0 mm). At z = 4.8 mm, some swelling is observed in the morphology as shown Figure 9 (a, j). With more beam focusing (i.e. less defocusing with smaller z = 3.6 mm), more swelling of polyimide is observed along with the emergence of a clearly defined porous structure, having isotropic pores on the surface as shown in Figure 9 (c, k). At z = 3 mm, the pores appear to be larger in size and more anisotropic as shown in Figure 9 (d, l). With further beam focusing, alignment emerges in a highly anisotropic cellular network structure at z = 1.8 mm, as shown in Figure 9 (f, m). Approaching z = 0 mm, nanofibers form starting at z = 1.2 mm, with progressively

more voluminous woolly morphology, as seen in Figure 9 (i, n). High-resolution SEM imaging shows that nanofibers of ≈ 60 nm form at $z = 0$ mm Figure 9 (o).

These transitions capture the evolution of LINC morphology with increasing average fluence values. A model of these fluence-dependent transitions is illustrated schematically in Figure 9 (p), which shows the phenomenon of swelling and blistering of the polyimide, followed by the formation of pores that gradually increase in number, size, and anisotropy, leading to the formation of anisotropic cellular networks. These 3D graphene networks become more aligned at higher fluence and eventually individual nanofibers emerge in voluminous wooly morphologies. While this model is useful in designing LINC patterns with tailored properties, further research using high speed *in situ* characterization methodologies is needed in order to reveal the temporal evolution of the LINC morphology during lasing.

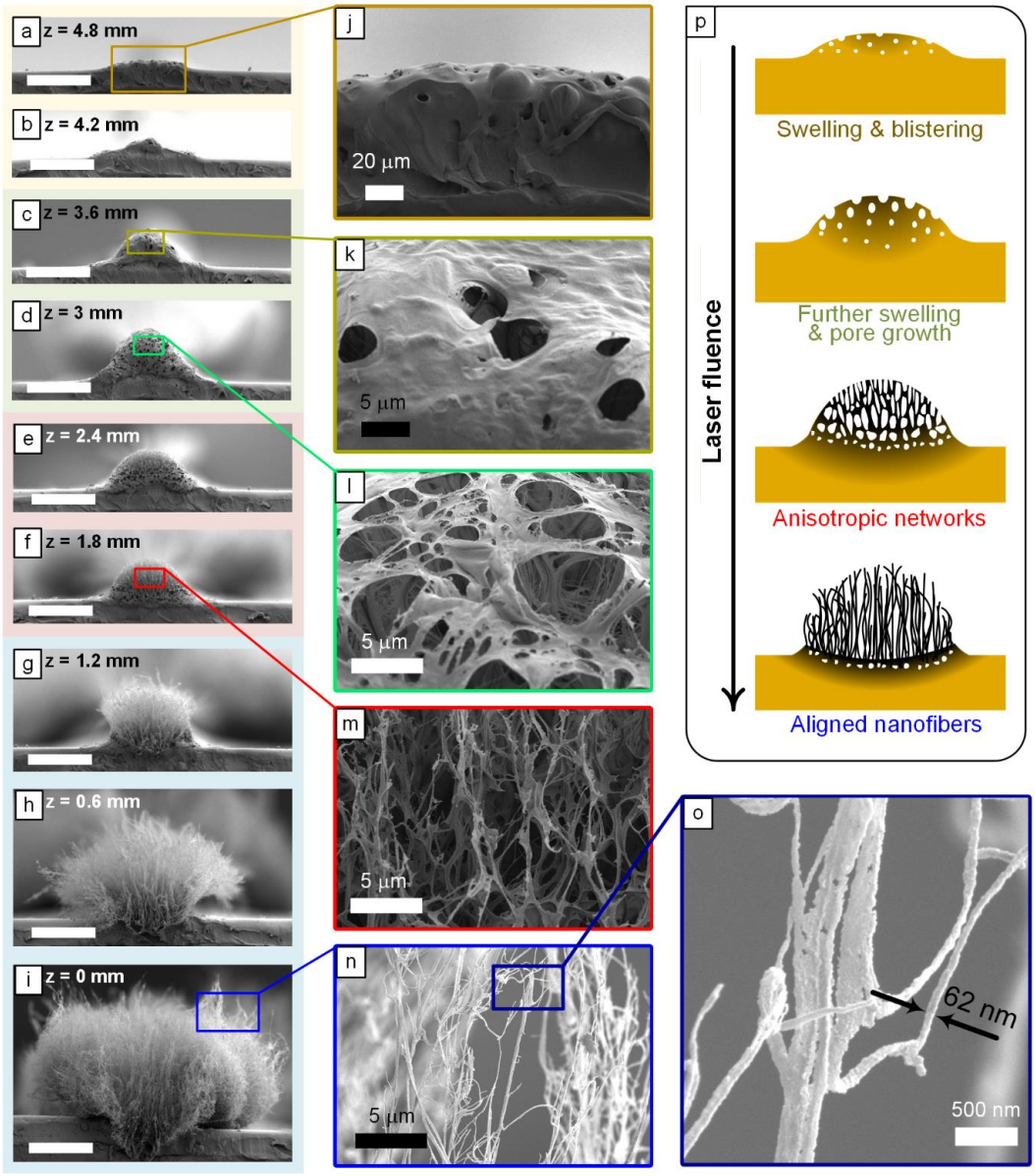

Figure 9: (a-i) SEM images of side views of the edge of polyimide films lased to generate LINC,while untilted (γ = 0°) at different z values (Scale bar: 100 μm). (j-o) Higher resolution SEM images. (j) SEM showing the swelling of polyimide. (k) SEM showing pore formation and growth. (i) SEM showing increase in pore shape anisotropy. (m) SEM showing the formation of anisotropic cellular networks. (n) SEM showing the formation of LINC nanofibers. (o) High resolution image showing ≈ 60 nm nanofibers. (p) Schematic illustrating the evolution of LINC formation with increasing fluence, showing the transitions between different LINC morphologies.

3.8 Equivalence of LINC Formation on Tilted and Untilted Samples

In light of the results discussed above energetic and kinetic equivalence in the cases of laser heating across tilted and untilted samples, the most important aspect of equivalence is the similarity of LINC morphologies obtained in both cases.

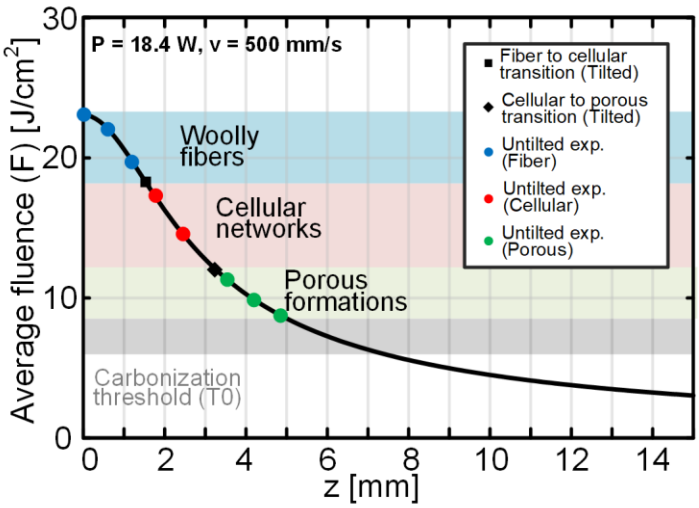

Figure 10: The average fluence experienced by the substrate at P = 18.4 W and v = 500 mm/s at different level of defocus (z) , the transitions from woolly fibers to cellular networks and from cellular to porous structures (calculated form tilted lasing experiments) are illustrated. Additionally, the morphologies experienced at different z values from the untilted lasing experiments are presented.

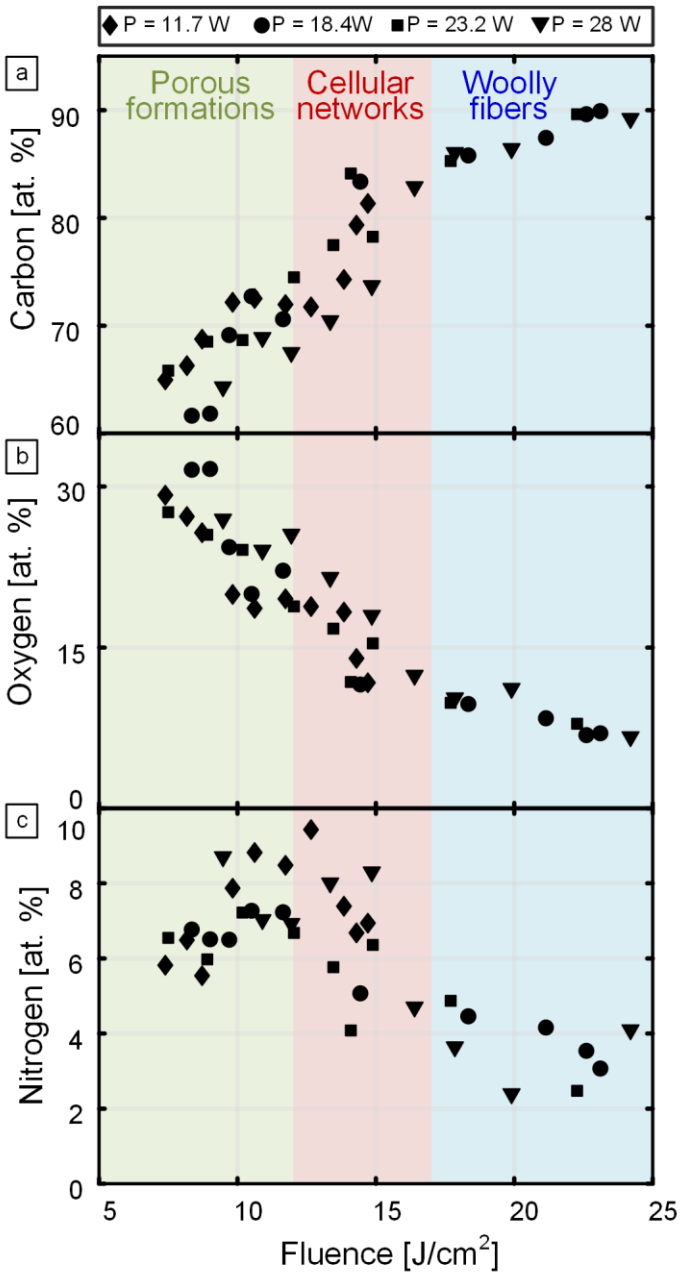

Figure 11: Fluence-dependent elemental composition of LINC from XPS measurements represented as atomic percentage for carbon in (a), oxygen in (b), and nitrogen in (c). Results plotted here are collected from 38 survey scans at different points along the four lines lased on tilted polyimide substrate with γ=45° at powers of 11.7, 18.4, 23.2, and 28 W.

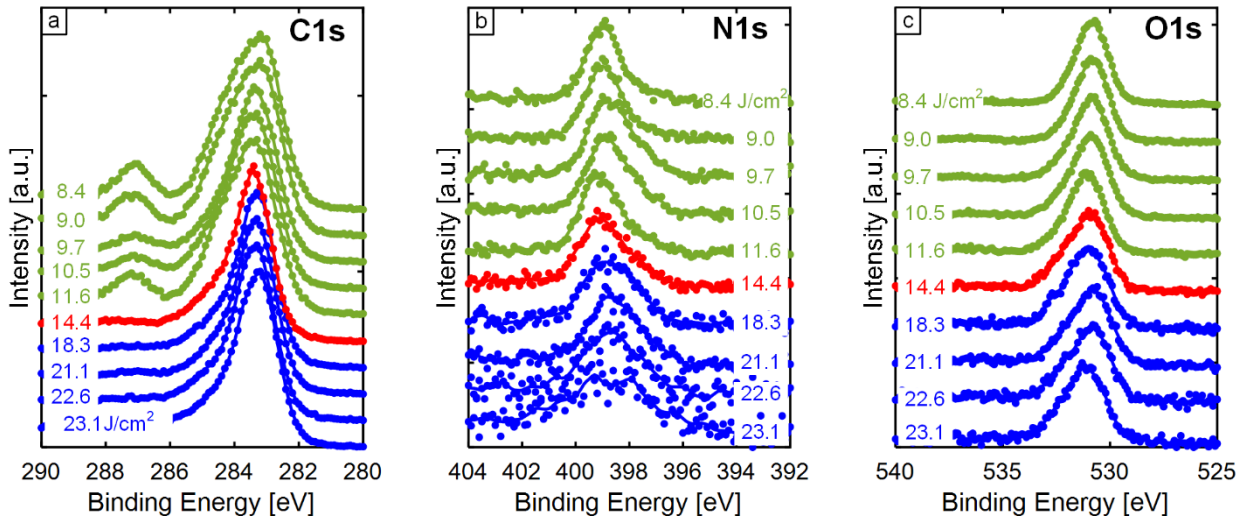

Figure 12: XPS results for several point across an individual LINC line generated by tilted lasing at γ = 45° at power P =18.4 W and speed v = 500 mm/s. (a) C1s core scans, (b) N1s core scans, and (c) O1s core scans. Fluence values are indicated on each spectrum in (a). Note the disappearance of the broad band between 286 and 288 eV in (a), which indicates that rapid loss of heteroatoms after T1. All green lines represent isotropic porous morphology, while the red spectrum represents anisotropic networked morphology, and the blue spectra represent aligned nanofibers.

Hence, we confirm here that the LINC morphologies obtained in the case of flat untilted lasing experiments shown in Figure 9 (a-i) match the morphologies resulting from tilted lasing experiments shown in Figure 6 (e) at P = 18.4 W and v = 500 mm/s. This comparison between the fluence-dependent morphological transitions in both cases is plotted in Figure 10.

3.9 Fluence-dependent Chemical Evolution

We use X-ray photoelectron spectroscopy (XPS) to characterize the fluence-dependent morphologies at several points along the lased lines (Figure 11) using the tilted sample approach shown in Figure 6 with $\gamma = 45°$ at different powers. We then use the mathematical model describing the beam to correlate each point across those lines to a fluence value. Accordingly, we plot the atomic percentages of carbon, oxygen, and nitrogen as a function of fluence, as shown in Figure 11. Results show that carbonization increases with fluence, owing to the progressive reduction in heteroatom content (oxygen and nitrogen). A rapid drop of both oxygen and nitrogen is observed after the T1 transition, which is also clearly observed in the C1s core scans shown in Figure 12 (a), wherein the broad band between 286 and 288 eV disappear immediately after T1. This rapid loss of heteroatom content is concomitant with a marked increase in carbon content, which is also observed from the sharpening of the carbon-carbon peak in the C1s scan (Figure 12 (a)). On the other hand, after the T2 transition, slower increase in carbon and slower decrease in both oxygen and nitrogen are observed.

It is worth noting here that plotting the evolution of elemental composition as a function of fluence is more insightful than plotting these values as a function of power, because fluence is a quantity that is normalized to the spot area, which changes along the laser path in our tilted lasing experiments (i.e. we have a gradient of fluence along the lines even though the power and speed are constant, as shown in Figure 6). Also, the fact that we are lasing only individual lines with no overlapping laser paths means that the fluence values we calculate are truly representative of the energy delivered locally at each point on the substrate, as opposed to the case of rastering 2D pixel arrays (or overlapping lines), where changing power, not only changes fluence, but also increases the overlap between neighboring pixels.[30]

3.10 Insights into coupled physicochemical phenomena governing LINC formation

Multiple processes are involved in the formation of LINC, which depend on factors like laser wavelength, laser intensity, fluence, IR absorption of the material and type of polyimide. These inputs drive the temperature and heating rate in the polyimide and hence control the level of liquification, outgassing and carbonization that occur. This in turn affects the resulting morphology and molecular structure and hence the resulting properties. Chemical reactions also drive these processes like thermal dissociation and carbonization of the polyimide, solid-liquid phase transitions, plasma material interactions, melt expulsion and melt dynamics driven by Marangoni convection.[73] In addition, the optical properties of the material can change, driving complex chain reactions, caused by the changing absorptivity of the material.[74] These processes can also depend on the gas environment and partial pressure. Moreover, they take place at different time scales, further complicating the phenomenon.

A number of noteworthy phenomena are observed in our experiments, which provide insight into the LINC formation process. For example, the transition to woolly fibers (T2) is clearly observed from the SEMs in Figure 8 and Figure 9 by the drastically bigger volume of carbon, which suggests that the kinetics of forming the woolly fiber morphology is faster than the kinetics of forming cellular networks and isotropic porous morphology.

Hence, the rate of outgassing during laser irradiation is higher for higher fluence, which is also supported by the XPS results indicating more loss of oxygen and nitrogen at higher fluence (Figure 11 and Figure 12). This rapid jetting of gases out of the surface can also explain the increase of anisotropy in the porous structures that is observed after T1, as well as the alignment of the nanofibers after T2. In fact the mushroom-top geometry of LINC observed for fluence exceeding T2 (Figure 9 (g-i)) resembles high speed images of laser-induced splashing of polymers

from literature.[75] Such plashing dynamics of liquefied polymers could drive the formation of aligned woolly nanofibers upon rapid conversion into solid carbon.. Hence, our results indicate that the liquification and rapid solidification beyond T2 hinders graphitization of carbon and hence leads to the lower G and D peak FWHM and the disappearance of the 2D peak observed in Raman spectroscopy (Figure 8). Moreover, at even higher fluence, exceeding 25 J/cm^2, the consumption of the polyimide leads to splitting of the film as the laser either ablates, melts, and/or chemically converts the whole thickness of the film.

A better understanding of the chemical transformations that take place during these transitions can be built on previous pyrolysis research on the evolution and graphitization of different types of polyimide at temperatures up to 3000 °C. These studies are based on transmission electron microscopy (TEM),[76] Raman spectroscopy,[45,77] infrared spectroscopy, and outgassing observations at different temperatures. These studies show that carbonization of polyimide films occurs over two steps. Initially at a temperature of 500 °C – 650 °C there is an abrupt weight decrease of the films accompanied by the release of large amounts of CO and CO_2. This is followed by less weight loss and shrinkage due to evolution of small amounts of methane, hydrogen and nitrogen which can occur over a temperature range from 800°C to above 1000 °C.[78,79] It was also reported that nitrogen release continues in the second step of carbonization up to temperatures above 2000 °C and can be released abruptly.[80] These findings further support the hypothesis that the morphology transitions we observe (T1 and T2) are partly attributed to the rapid rate of gas released, especially when interacting with material jetting that can lead to the formation of nanofibers through rapid solidification of the jetted material. This mechanism of nanofiber formation is analogous to the fabrication of polymer nanofibers by electrospinning,[81] albeit at much higher temperatures and more rapid heating/cooling rates. It should be noted that

the *in situ* polyimide pyrolysis studies were carried out using relatively low heating rates(≤ 30 °C/min),[82] compared to rapid temperature increase rates typical in laser irradiation. Hence, they do not necessarily represent the same reaction pathways taking place during laser heating of polyimide, which is an inherently non-equilibrium process in contrast to the quasi-equilibrium process of the slow heating. Structurally, TEM studies of the pyrolyzed polyimide have shown that the slowly carbonized polyimide exhibited turbostratic structure with nano-scale elongated pores from temperatures as low as 650 °C up to temperatures as high as 2450°C, beyond which the carbonized polyimide graphitized into high quality flat layers of graphitic carbon sheets comparable to pyrolytic carbon.[76]

3.11 Correlating LINC Morphology to Electrical Eesistivity

To understand how the observed morphology transitions affects the properties of LINC, 15 mm LINC lines are lased at different z values and two power values, P = 11.7 W and P = 28.0 W in untilted configuration ($\gamma = 0°$). Using the two point probe method, the resistance divided by line length (R/L) values are calculated from multiple resistance measurements at different lengths. First, the change in spot area as a function of z, according to the beam model is plotted in Figure 13 (a).

The average R/L values for P = 11.7 W and P = 28 W are plotted in Figure 13 (b) and Figure 13 (d), respectively. For P = 11.7 W, the polyimide is not conducting at $z > 3$ mm and $z < -3$ mm. For z between -3 and 3 mm, the average R/L values are at their highest at the edges of the range with values between 2.1 KΩ/mm to 2.5 KΩ/mm, indicating that the connectivity of cellular networks in key for writing highly conducting LINC. These values of R/L are within the range of

previously reported values for LINC.[31,53] As the spot size decreases at values around $z = 0$, R/L decreases to a value of around 1.65 KΩ/mm. The average carbonized line widths are noted to be ≈ 130 μm as illustrated from optical microscopy images.

Raman spectroscopy of these lines show a general inverse relationship between R/L values and the I(2D)/I(G) ratio. Indeed, we find that LINC with a well-defined and sharp 2D peak, exhibited the lowest resistivity. The average I(2D)/I(G) ratio starts at a value between 0.4 - 0.45, and increases for smaller spot size till a maximum value of around 0.53. Similar trends are observed in the I(G)/I(D) ratio where it reaches a maximum value of around 1.25. At higher power (P = 28 W), R/L values are significantly smaller (Figure 13 (d)), with values ranging between 1 KΩ/mm and 0.4 KΩ/mm when compared to the lower power case. Again a decreasing trend is observed with beam focusing, with R/L decreasing from around 1 KΩ/mm at z = 9 mm to around 0.4 KΩ/mm at z = 7 mm as the porous morphology transitions into a more anisotropic cellular networks. The average value of R/L then remains constant until the onset of the fibrous morphologies where the resistance increases drastically. At z > 4 mm (i.e. below the T2 threshold for fiber formation), the line width was measured to be ≈ 250 μm.

The I(2D)/I(G) ratio for P = 28 W are generally similar to those obtained for P = 11.7 W, with values between 0.42 at z = 8 mm, and 0.49 at z = 7 mm. Importantly, the disappearance of a sharp 2D peak at the onset of fiber formations (around z = 3.8 mm) is accompanied by a drastic drop in conductivity. The conductivity of the LINC lased at P = 28 W and v = 500 mm/s is estimated to be around 5 S/cm, matching LINC conductivities measured by other groups,[31] and superior to unannealed ink jet printed graphene.[83] The resistivity could possibly be further increased by optimizing the laser parameters such as speed or relasing.[84]

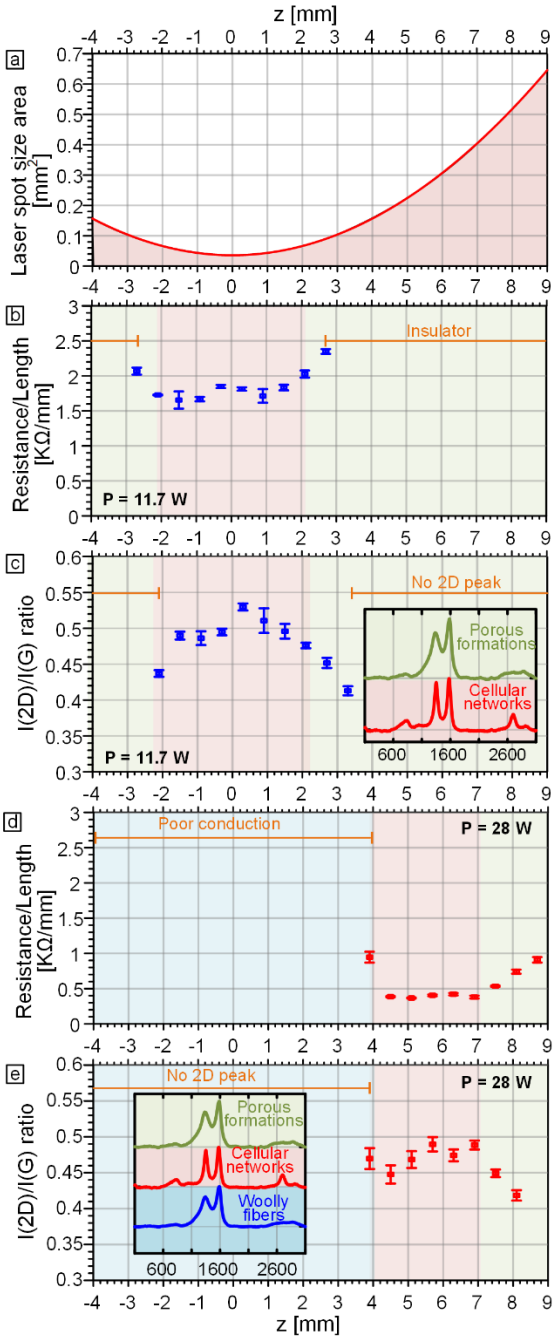

Figure 13: (a) Plot showing the change in laser spot area with *z* according to the laser beam profile. (b) Change in average R\L (average of 3 samples and error bars are standard deviation) with change in *z* value for the case of *P* = 11.7 W. (c) Plot representing the change in average I(2D)/I(G) ratio (average of 3 samples and error bars are standard deviation) with changing spot size and fluence. (Inset in c) Raman spectra at two different morphologies. (d) Change in R\L (average of 3 samples and error bars are standard deviation) with change in *z* value for the case of *P* = 28.7 W, illustrating the drop of resistance with decreased spot size until the formations

of highly insulating woolly fibers. (r) Plot representing the change in average I(2D)/I(G) ratio (average of 3 samples and error bars are standard deviation) with changing spot size and fluence for *P* = 28.0 W. (Inset in e) Raman spectra at three different morphologies.

Taken together, our electrical resistivity measurements agree with the structural changes observed in our Raman spectra (Figure 7 and Figure 8), which demonstrate that the first transition (T1) is associated with the decrease in FWHM of the G and D peaks and the emergence of the 2D peak. Relatively high FWHM in the G and D peak is typically associated with amorphous or disordered carbon and is noted in low temperature carbonization of polyimide,[45] with an expected high resistivity. On the other hand, smaller G peak FWHM is strongly correlated to the degree of graphitization and defect level,[85,86] which are crucial for lower resistivity nanocarbons. Moreover the emergence of the 2D peak is also evidence of large structural changes in the graphitic domains between T1 and T2. Disappearance of the 2D peak and increase in the FWHM of both G and D peaks are characteristics of the Raman spectra for fluence higher than the second transition (T2), producing woolly fibers with large volume. From the resistance measurements, it is clear that these complex interactions underlying fiber formation at high fluence values result in very low conductivity LINC that is not suitable for applications as electrodes, highlighting the importance of modulating fluence during LINC formation, i.e. too small or too large fluence values prevent the formation of conducting LINC.

3.12 Advantages of Fluence-based Approach and Outlook

Two analytical approaches are typically used to understand how lasers interact with polymers. The first is the thermal approach, which focused on calculating the temperature rise in the material.[87–89] The second is the fluence-based approach, which focuses on calculating the delivered laser energy in the material. Thermal models require estimating material properties of polyimide and LINC and are difficult to validate experimentally since it is difficult to measure the temperature at the laser spot;[89,90] hence, they are generally more complex than fluence-based models. In this work we present a fluence-based approach for understanding LINC formation, based on Gaussian beam modeling, which is of a great utility from a manufacturing perspective.

We also focus on lasing individual LINC lines in air, instead of areas formed by overlapping laser paths; hence, we avoid the effect of multiple lasing of some regions on the surface, which greatly complicates the analysis and hinders extracting fundamental insights into the process-structure relationships for LINC formation. Lasing lines also has an advantage over lasing individual spots, because we can circumvent laser power transient effects that are associated with laser ramping up when starting. By ignoring the initial portion of the lased LINC lines, we ensure that steady state power is reached, when investigating the rest of the line or its end. In fact, when lasing our LINC lines it was sometimes observed that the initial spot has a drastically different morphology than the rest of the line, which is attributed to power transients in the laser.

In addition to elucidating the fluence-dependence of morphology, molecular structure, and electrical conductivity of LINC, our approach also enables generating maps of resulting morphologies as a function of accessible laser processing parameters, such as power and defocus, which can be easily controlled.

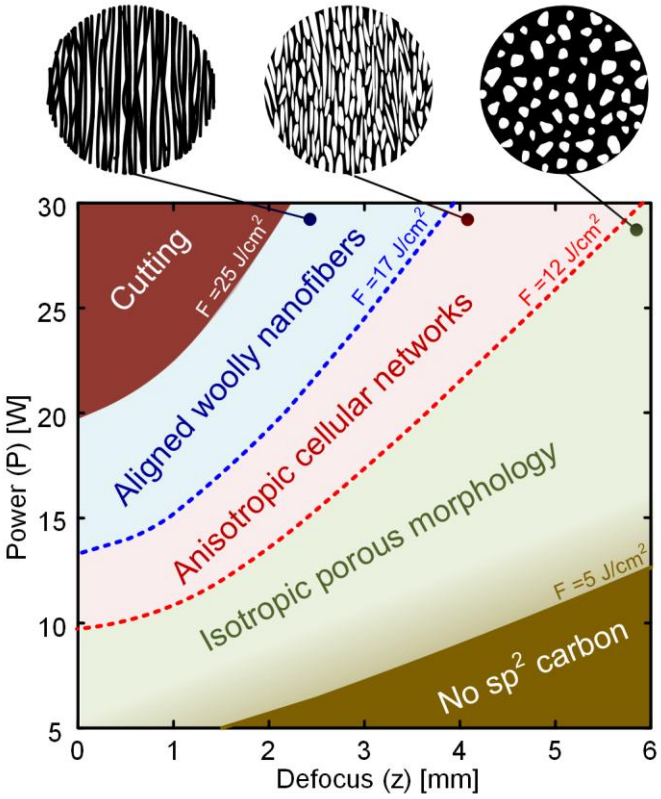

Figure 14: Morphology diagram mapping the ranges of laser parameters (power and degree of beam defocusing) for creating different types of LINC (isotropic porous morphology, anisotropic cellular networks, and aligned woolly nanofibers) for CW CO_2 laser (wavelength λ=10.5 μm) scanning at to v = 500 mm/s. Experimentally obtained threshold fluence values for T1 and T2 are plotted as constant fluence lines (dashed).

Figure 14 shows such a morphology diagram with delineated transitions represented as iso-fluence contours, which is enabled by the insight that transitions happen at threshold values of laser fluence. Furnishing this fluence-based diagram is of great utility for practical purposes to facilitate replication of experimental results across different research groups using different laser processing systems. Moreover, our approach of plotting the morphology diagrams is useful for studying the influence of pressure and gas environment on LINC. Hence, more insight into the influence of these environmental factors on the evolution of both the chemistry and morphology

of LINC can be obtained by carrying out fluence-dependent LINC formation studies under controlled gas conditions.

3.13 Conclusion

Using CO_2 laser irradiation of polyimide, we demonstrated the direct formation of a variety of nanocarbons ranging from isotropic porous carbon, highly anisotropic cellular networks of graphitic carbon, and aligned carbon nanofibers. We developed a fluence-based approach to elucidate the process-structure-property relationships governing LINC formation for these morphologies. This is achieved by mathematically modeling the effect of degree of defocus on intensity distribution and fluence for a Gaussian laser beam. We also presented an approach for creating fluence gradients on tilted polyimide films. Importantly, two specific threshold values of fluence were identified that correspond to the following: first, the transition from isotropic porous morphology to anisotropic cellular networks (T1) at a fluence value of 12 J/cm^2; second, the transition to aligned woolly nanofibers (T2) at a fluence value of 17 J/cm^2. Moreover, we show anisotropic cellular networks have the highest electrical conductivity ($\approx$ 5 S/cm) for our conditions (laser wavelength of 10.6 μm and scanning speed of 500 mm/s), due to the lateral connectivity and the high graphitic content. Hence, our model and results provide insights into the physicochemical processes underlying LINC formation and enabled generating a morphology diagram of laser processing parameters.

LINC is shown to be an attractive method to fabricate porous conductive electrodes directly on flexible substrates, which are required for a wide range of applications. As an alternative to printing technologies from nanocarbon inks, LINC formation is more scalable and less costly.

Taken together, our results show that material properties such as resistivity can be tuned through morphology adjustment based on local control of laser fluence. Accordingly, the variety of LINC morphologies achieved and the tunability of their properties make them superior to printing techniques that require the preparation of different nanocarbon inks for writing carbon-based electrodes with different morphologies and molecular structures on flexible substrates. Moreover the ability to control the spatial variation of morphologies and properties on the same substrate can be particularly useful in designing LINC for applications integrating high surface area nanocarbon electrodes with highly conductive and dense traces, such as for electrochemical applications.

4.0 Kinetically Controlled Laser Induced Graphene and Ablation Thresholds

4.1 Introduction

The pathway from polyimide to the diverse nanocarbon morphologies is a complex process starting with the polyimide photothermally absorbing the laser light[68] and the cleavage of the C-N, C-O and C-C bonds in the polymer [91,92], leading to the rapid release of gases like oxygen, carbon dioxide and nitrogen gas[93] which interact with the viscoelastic nature of the polyimide[94] and the eventual formation of sp_2 graphitic carbon domains and graphene.[95] This is all a highly non-equilibrium process because of the high temperature rates involved and the interaction between the different physical phenomenon, making it a challenging process to analyze.

Typically when studying laser nanocarbon synthesis, researchers correlate the resulting property and morphology to the process through an energetic approach, by estimating the optical energy delivered/absorbed per area, known as fluence or by simply reporting power and speed[53,96]. The authors have previously shown that when lasing individual lines with a spatially varying fluence gradient at a specific lasing speed (500 mm/s), discrete morphologies were observed, which were either of porous, cellular or fiberous nature.[97] These morphologies were correlated to chemical and structural changes, and were observed at defined thresholds of fluence, confirming that an energetic approach to understand the process is valid at least at a fixed speed with different laser power values, despite the non-equilibrium nature of the process.

However, is this approach valid at higher and lower speeds? The same fluence value delivered at different values of speed can vary drastically in terms of temperature and temperature

change with time, which can greatly affect the resulting morphology and carbonization. Can the resulting morphologies be related to specific temperatures or temperature rates, i.e. energetically controlled/limited or kinetically controlled/limited? How does the process energetics and kinetics influence the chemistry and gas release in process?

In this chapter, we utilize the unique approach presented in the previous chapter to analyze laser nanocarbon formation through lasing lines with continuously varying laser fluence at different speeds to facilitate understanding the process kinetics. The resulting lines represent a map of a wide range of conditions, allowing precisely identifying morphological, structural and property changes. Through lasing at a fixed power and different speeds ranging from 100 mm/s to 500 mm/s at a power of 28W, a more complete picture including process kinetics can be derived.

Overall, this approach enables studying the evolution of nanoscale morphology and atomic structure continuously at different fluence values on the same polyimide film to investigate the influence of speed on morphology and structure. We integrate the experimental results with two energetic based approaches for estimating fluence: an area averaged fluence approach and a two dimensional fluence model to test whether a fluence based approach can explain the results. Additionally, to get a deeper understanding of the process kinetics, we integrate the experimental results with thermal simulation results and correlate the results with process temperatures and temperature increase rates.

4.2 Tunable Beam Intensity for Patterning Graphitic LINC on Polyimide

In a typical LINC process, a laser beam with power P is scanned across a polyimide sheet at a speed v with the sample surface at a distance z from the beam waist. Here, we expose the polyimide sheet to a spatial gradient of fluence by lasing a tilted sample of polyimide. This enables different points on the linear lasing path to be exposed to different beam spots having different size and fluence. A schematic of the experimental setup is shown in Figure 15 (a), showing the polyimide sheet lased at an angle (γ= 45°). The schematic shows the laser beam, assumed to be a Gaussian beam, moving in a horizontal direction x at a speed v, the sample is tilted along the x' direction. The spot size changes with z and it also changes as well as along the x' direction on the sample.

The beam profile of the continuous CO_2 laser (λ=10.6 μm) used for this study is depicted in Figure 15 (b), estimated from beam characterization experiments described in previous work. Beam power and profile measurements are used to estimate the laser intensity profile at the different z values and at different spot sizes and powers. The tilting of the beam changes the beam intensity distribution and the geometry of the beam spot, however the authors demonstrated in previous work that for the beam parameters used here, the average fluence value for the flat case is approximately equal to the tilted case for our values of beam parameters and the conclusions derived from tilted polyimide experiments can be generalized to flat lasing.[97]

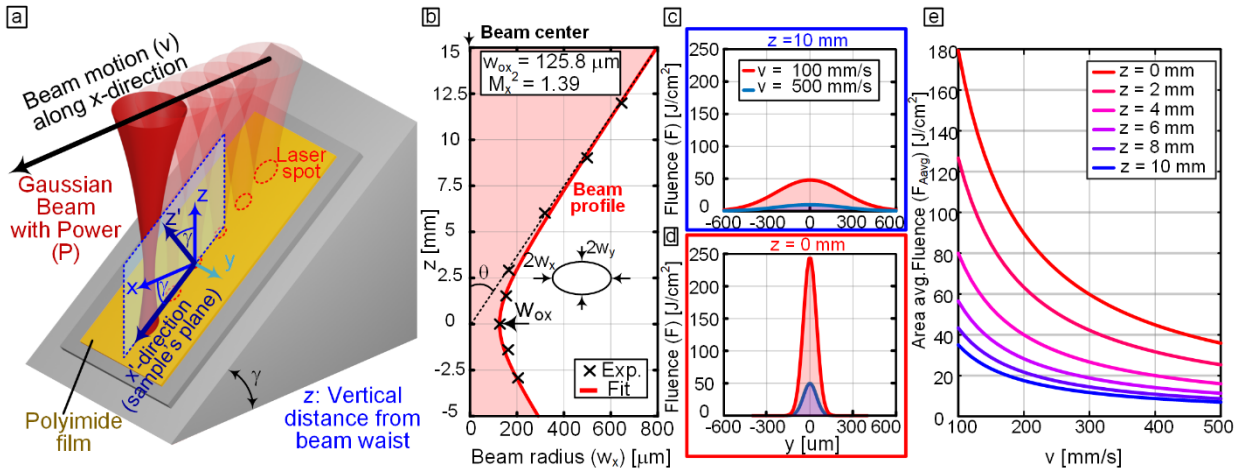

Figure 15 (a) Schematic illustrating the experimental setup with laser with power P, speed v lasing a polyimide sheet tilted by angle γ. (b) Plot representing the estimated laser beam profile along the x direction, along with the profile of the fitted Gaussian beam (c) Distribution of fluence along the y-direction at P = 28W, v =100, 500 mm/s and defocus z = 10 mm. (d) Distribution of fluence along the y-direction at P = 28W, v =100, 500 mm/s and defocus z = 0. (e) Plot showing the influence of defocus and speed on area averaged fluence F_{Aavg}.

4.3 2D Fluence Model

The laser beam flux (I) is expressed at a point (x, y) at the laser beam focus and time (t) using scanning in the x-direction with speed (v) according to the following expression:

$$I(x,y,t) = \frac{2P}{\pi w_{ox} w_{oy}} e^{-\left(\frac{2(x-(L_x-vt))^2}{w_{ox}^2} + \frac{2y^2}{w_{oy}^2}\right)} \quad (4\text{-}1)$$

where P is the laser beam power, w_{ox} and w_{oy} is the beam waist size, v is the beam velocity and L_x is the lasing length in the x-direction.

To estimate the fluence at a point, the x and y-values are fixed at a point (x_o,y_o) and the flux is integrated over time using the following expression:

$$F(t) = \int_0^{\infty} I(x_o, y_o, t)\, dt \tag{4-2}$$

If this value is estimated at different y-values perpendicular to the laser path, the fluence (*F*) delivered across the sample can be estimated due to a single laser path.

4.4 Tunable Beam Intensity for Patterning Graphitic LINC on Polyimide

An example is shown in Figure 15 (c, d) which shows the change of fluence distribution F (defined in the previous section) across the beam for two z values and two speed values at the same laser power. A more focused beam has a sharper beam intensity, however it has a smaller spot size, which decreases the dwell time of the laser spot, which corresponds to how long a point is exposed to the laser beam. Additionally, changing the speed also changes the dwell time, with higher dwell times at lower speeds and hence higher delivered fluence. The influence of speed on dwell time is shown in Figure 16. The interaction between the beam dwell time and laser intensity can be used to tune the value of fluence distribution (F) across the beam and area averaged fluence (F_{Aavg}), which would in turn influence the temperature increase at a point. The change in area averaged fluence F_{Aavg} with laser speed at different focusing levels is shown in Figure 15 (e), illustrating the extent of speed influence on delivered fluence. The figure also illustrates that equivalent levels of fluence exist at different speeds and defocus level, despite different laser conditions.

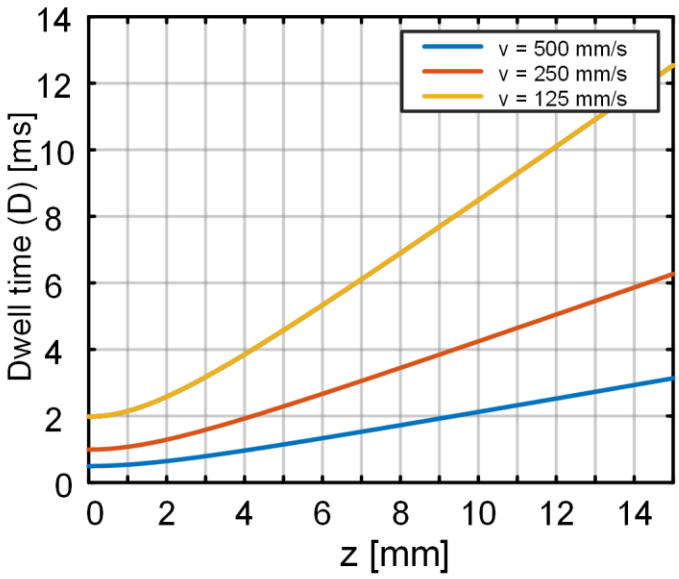

Figure 16: Plot illustrating the influence of speed on laser spot dwell time.

4.5 LINC Morphology at High Speeds

The sample is lased at a constant power P = 28W at different beam speeds ranging between v = 100 and v = 500 mm/s, consisting of 11 lines as shown in Figure 17. As demonstrated in previous work, two morphological transitions thresholds are generally observed at high lasing speeds ranging from v = 500 mm/s to v = 312 mm/s under optical and SEM imaging. Initially, LINC lines exhibit a porous morphology as observed in SEM and optical microscopy imaging as shown in Figure 17 (a,c). This porous morphology is also characterized with a shiny appearance under optical microscopy Figure 17 (c) and isotropic pores on the surface observed under SEM Figure 17 (e). With increasing fluence, the porous morphology undergoes an abrupt transition into an anisotropic cellular networks at threshold location T1 that undergoes an area averaged value of fluence FT1. This threshold is characterized by the loss of the shiny character of the surface (Figure

17 (a,c)) and the transition of the surface pores into of an anisotropic LINC network as seen under SEM imaging Figure 17 (f). With increasing fluence, a second abrupt threshold is noted at location T2, experiencing fluence FT2. This threshold is characterized with the abrupt transition from the cellular formations into a large volume woolly fibrous as observed under SEM and optical imaging shown in Figure 17 (b, d). These woolly fibers formations have a distinct large volume and exhibits nanoscale fibers Figure 17 (g) and some level of alignment between them.

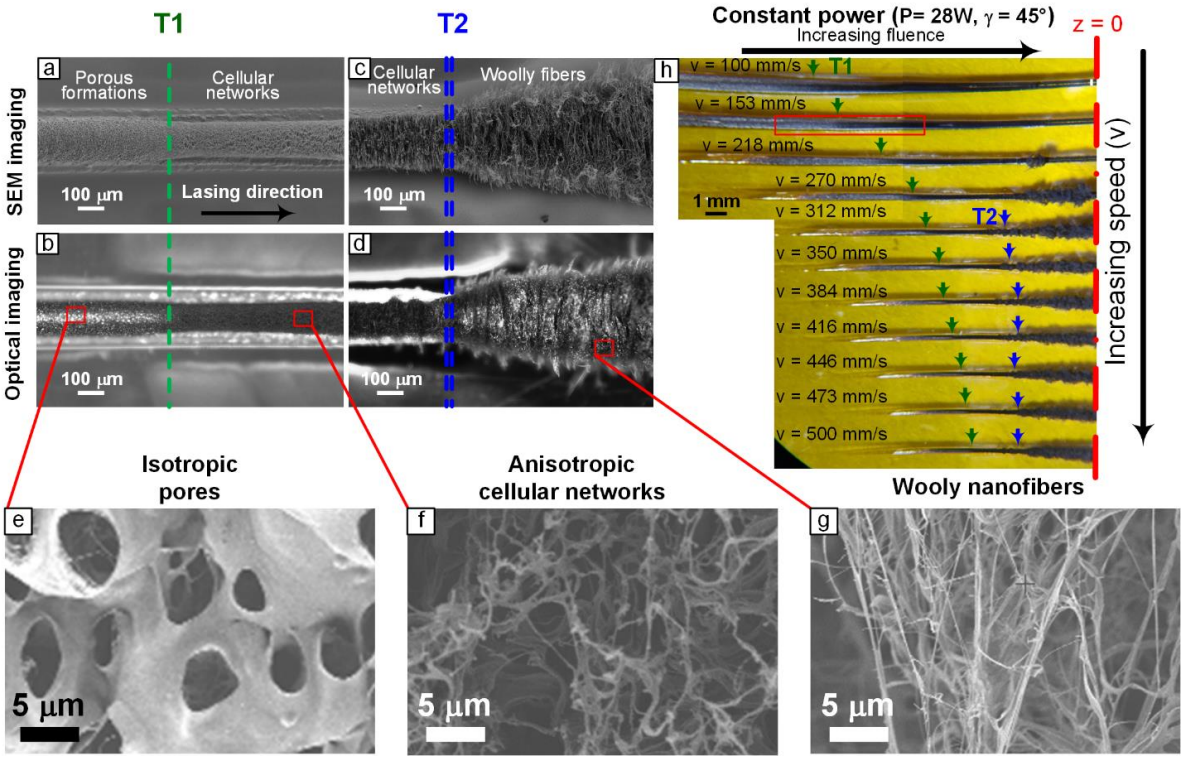

Figure 17 (a,b) SEM and optical imaging of the porous to cellular network transition at location T1 along lased LINC line at lasing conditions P = 28W, v = 500 mm/s. (c,d) SEM and optical imaging of the cellular network to wooly fiber transition at location T2 along lased line. (e) SEM image before T1, illustrating isotropic pore based morphology. (f) SEM image illustrating the anisotropic cellular network formations after T2. (g) SEM image illustrating the wooly nanofibers forming after threshold location T2. (h) Optical image showing the lines lased at P = 28W and speeds v = 100, 153, 218, 270, 312, 350, 384, 416, 446, 472, 500 mm/s and tilting angle γ = 45 ° illustrating the locations of the transitions along the lines.

This transition is typically associated with the thermal stability of the polyimide which is related to its backbone chemical bonding.[98] The T1 and T2 locations for the different lines lased at different speeds are marked in an optical image in Figure 17 (h). The T2 transition is no longer observed at speeds lower than v = 312 mm/s with only T1 transitions observed at v = 218, 153, 100 mm/s.

4.6 Ablation Threshold Identified at Low Speeds

At slower speeds between v = 270 and 100 mm/s, the T1 transition is observed with increasing fluence, however, with further increased fluence, a new unreported transition is observed which is characterized with the gradual ablation of the cellular networks following the T1 transition. While ablated morphologies have been reported before [88,96], the conditions governed their occurrence are not completely understood and it is first reported here. This transition is demonstrated in Figure 19 and Figure 18 (a, b) at v = 153 mm/s, which show a number of stitched SEM images along the lasing path with false coloring marking the onset of this ablation. Higher resolution SEM imaging show the difference between before the onset of ablation Figure 18 (c, d) and after Figure 18 (e, f). With increased ablation, a hierarchical porous network is revealed. The gradual nature of this transition is illustrated in Figure 20 which shows the gradual ablation of the cellular network and the reveal of the hierarchical pores structures beneath. This hierarchical porosity, which has been observed previously by Liu [53], exhibits multiple scales of porosity as seen in high resolution SEM imaging in Figure 21 which potentially has high surface area than prior to the transition. When lasing LINC electrodes on flat polyimide sheets, this same phenomenon can be observed, with the LINC electrodes exhibiting a dome shape at higher defocus

values and an ablated crater on top after ablation onset with more beam focusing. This is illustrated in Figure 18 (g, h), which shows cross sectional views of lased electrodes.

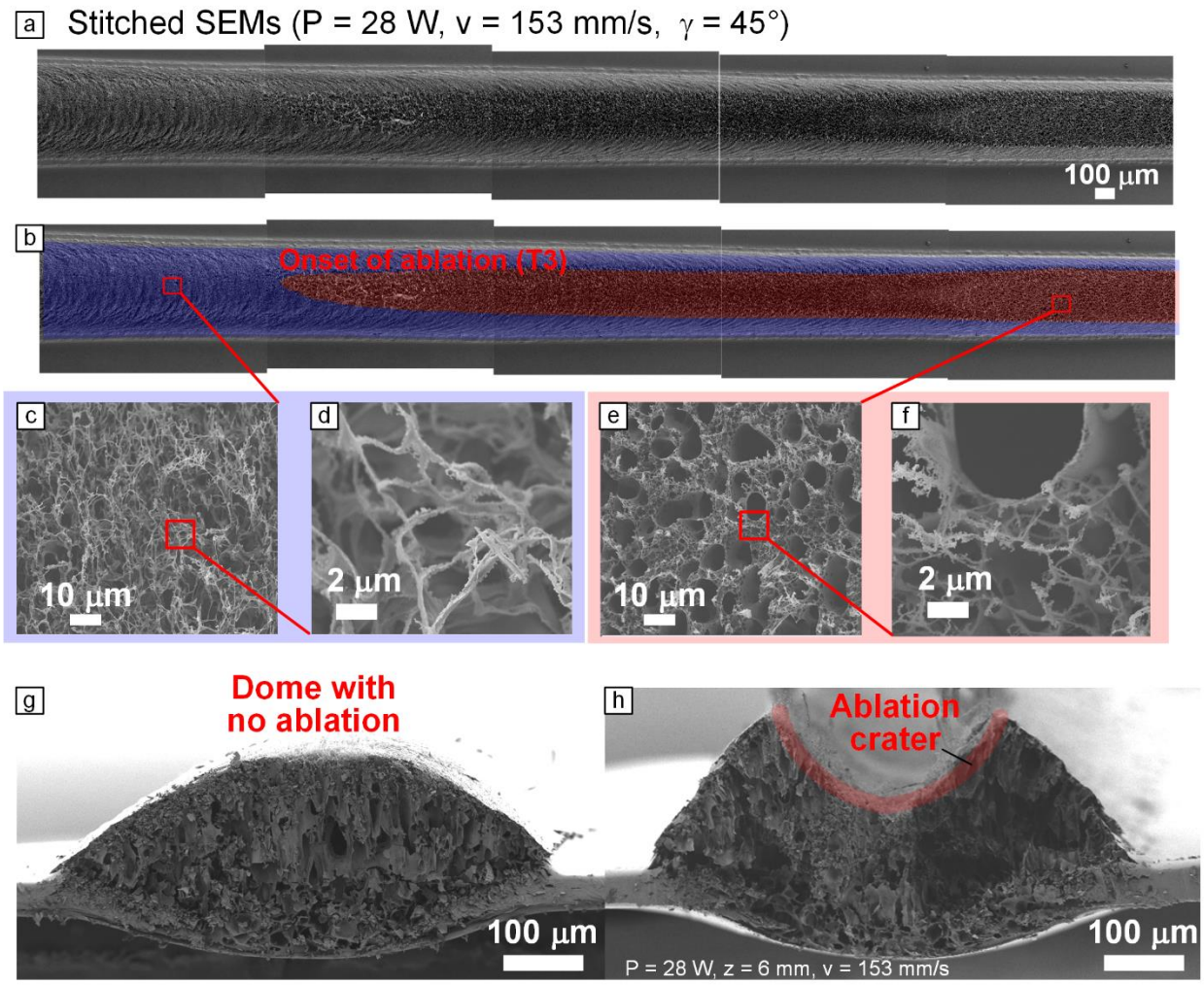

Figure 18: (a,b) Stitched SEM images illustrating the onset of ablation, starting at location T3 at P = 28W, v = 153 mm/s and γ = 45°. (c,d) SEM images illustrating the morphology prior to the onset of ablation, exhibiting a cellular network morphology. (e,f) SEM images illustrating the morphology after the onset of ablation, demonstrating a hierarchical porous morphology. (f,g) SEM images showing the cross sectional view of two LINC electrodes lased at two defocus levels, illustrating the effects of ablation on cross section and showing formation of the ablation crater associated with the threshold.

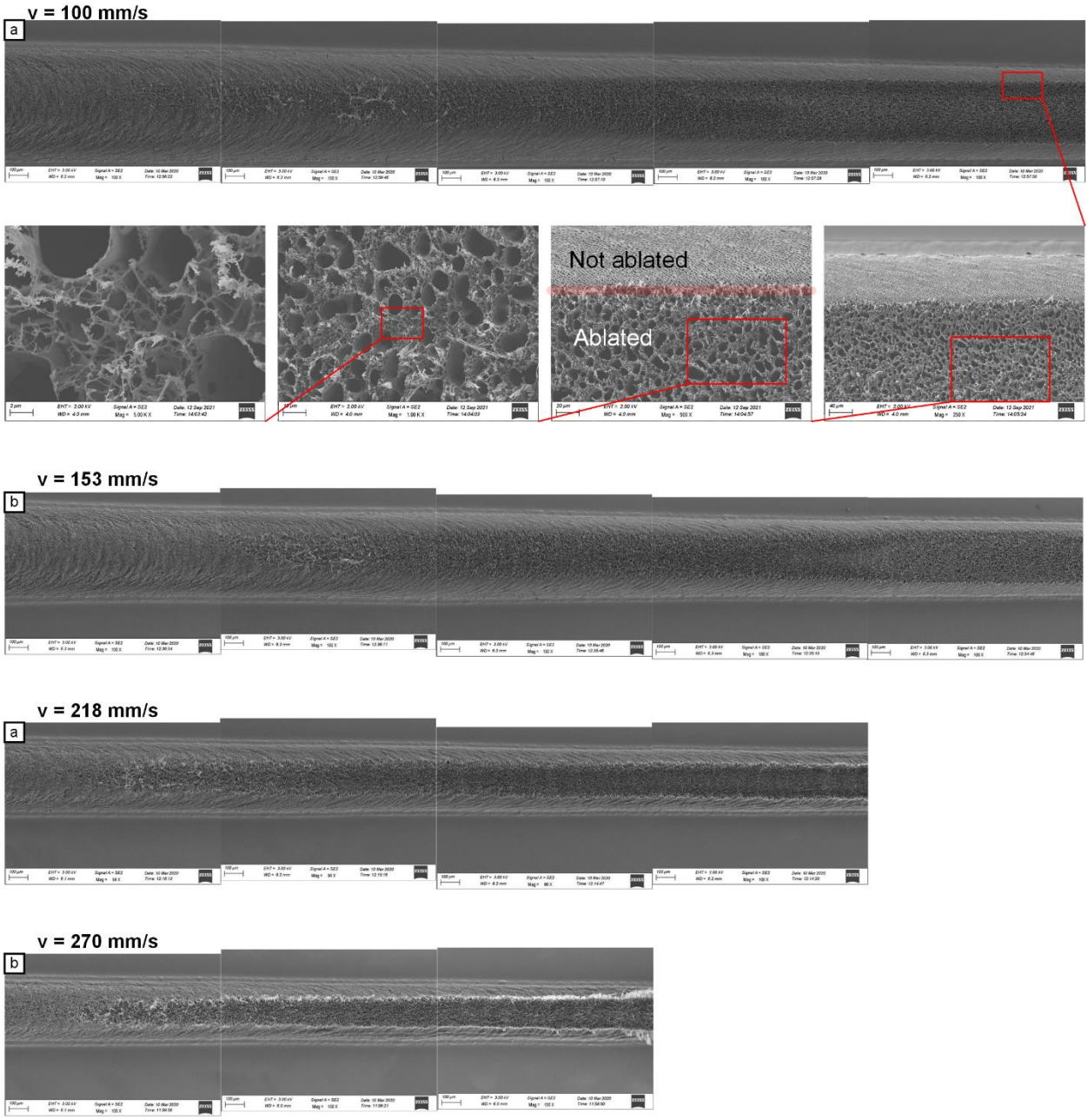

Figure 19: (a) SEM image illustrating ablation onset T3 at P =28 W, v = 100 mm/s along with high resolution SEM imaging illustrating the interface between ablated surfaces and unablated surfaces and hierarchical porosity morphology. SEM images showing the ablation onset at (b) v = 153 mm/s, (c) v = 218 mm/s, (d) v= 270 mm/s.

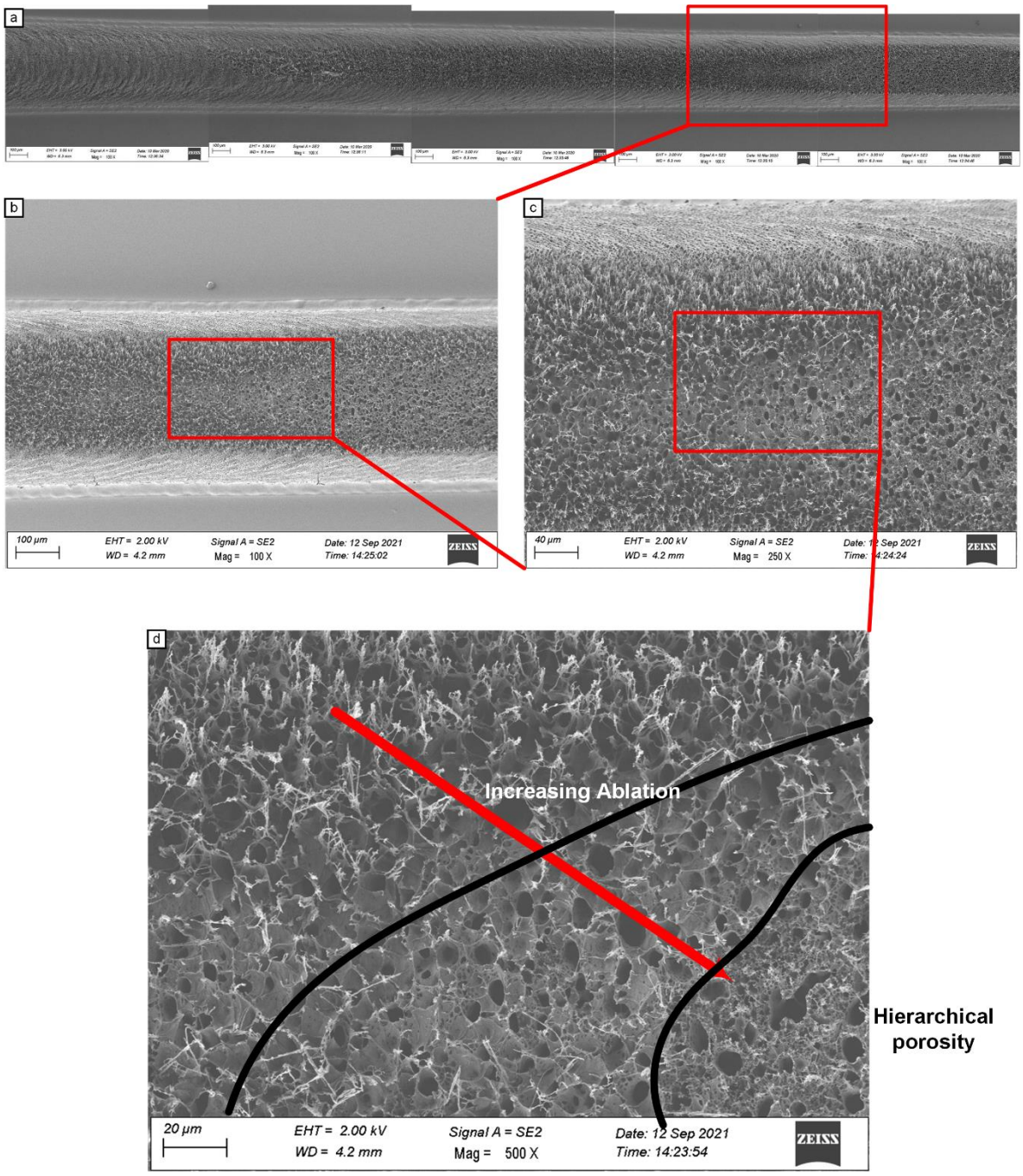

Figure 20: SEM images illustrating he gradual action of ablation along the line at P = 28W and v = 100 mm/s with increased fluence.

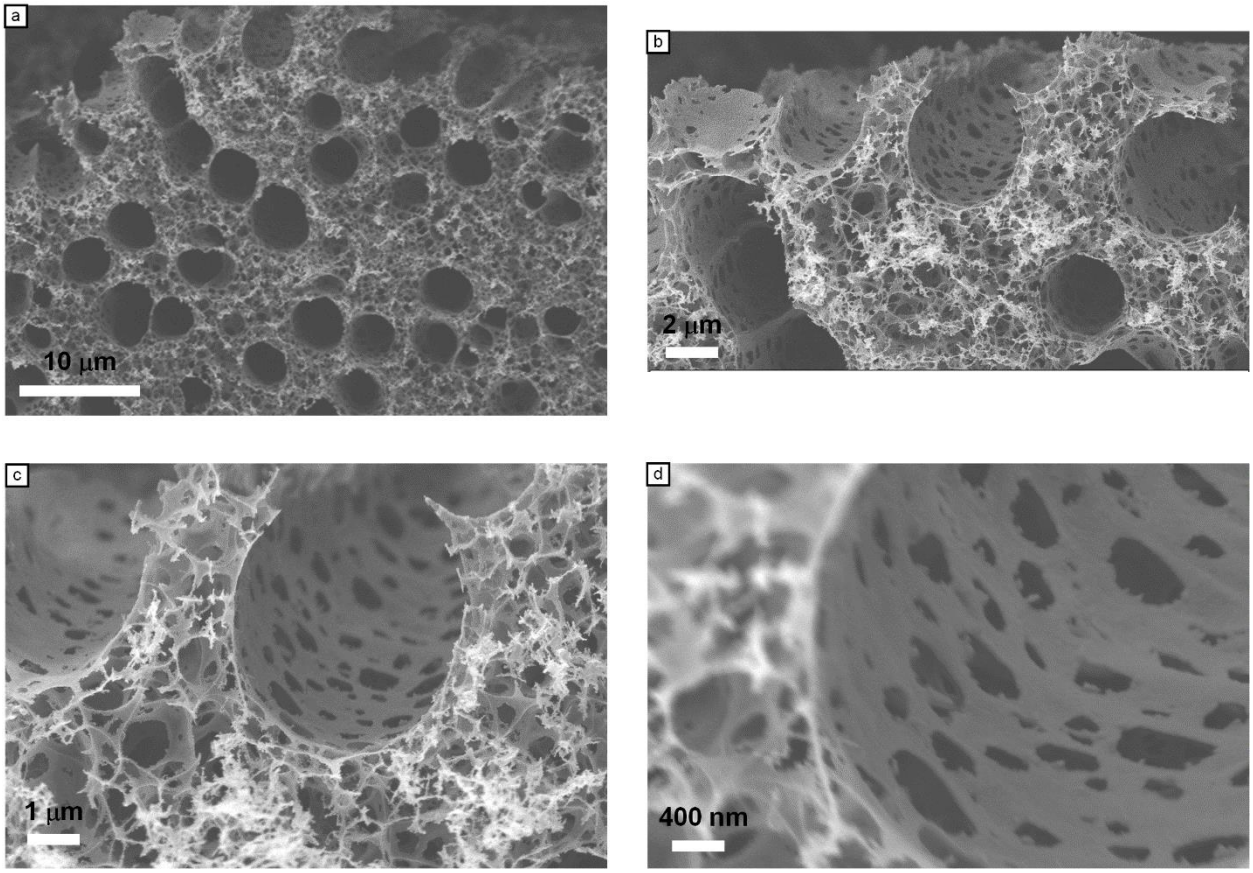

Figure 21: High resolution SEM imaging illustrating the hierarchical porosity and length scales of the different pores.

To understand if this transition is correlated with any structural or chemical difference, Raman spectroscopy and XPS analysis is conducted before and after the onset with the results presented in Figure 22, Figure 23, Figure 24 and Figure 25. The T1 transition from porous to cellular networks was previously reported by the authors to reflect on the Raman spectra with the appearance of the 2D peak [97], which would typically be non-existent in porous morphologies. Raman spectrum conducted at point P1 and P2 (Figure 22 (a)) before and after ablation at v = 153 mm/s is shown in Figure 22 (b), showing the existence of a 2D peak for both spectra, but also a marked decrease in D/G ratio after ablation onset. Deconvolution of the G, D and 2D peaks was done to extract peak parameters to accurately compare differences as shown in Figure 23and Table

1. The Raman results are summarized in Figure 22 (c-g). The results show a marked decrease in area based D/G ratio after ablation from a value of 1.47 to 0.64. Additional decreases are noted in 2D FWHM, D′ area, D+D′ area, D″ area all of which indicate higher sp2 crystallinity, improved stacking and less defects post ablation.[99] Representative XPS spectroscopy is also conducted before and after ablation with the survey scans shown in Figure 24 (a) and atomic percentage analysis summarized in SI Table 2. Corresponding C1s, N1s, O1s, C KLL scans are also conducted for in depth analysis of any chemical transitions and sp2 content analysis. The C1s core scans are shown in Figure 24 (b, c), with deconvolution analysis. The deconvolution results are summarized in Table 3. The survey scan and the atomic percentage analysis clearly indicate a decrease in O and N heteroatom content post ablation shown in Figure 22 (h). This is also clear from the O1s, N1s core scans with a notable increase in signal to noise ratio post ablation as shown in Figure 24 (d, e). The C1s core scan exhibits a graphitic nature, similar to HOPG C1s spectrum. The deconvolution analysis indicates a decrease in C-OH and C-O-C area, which is confirmed by the survey scan analysis in

Table 2 with the drop in atomic Oxygen percentage. Additionally, C KLL analysis, shown in Figure 25(a, b) to calculate the D parameter[100,101] indicates dominant sp2 bonding before (D = 19.5 eV) and after ablation (D = 20.25 eV). From the Raman and XPS analysis that clear structural changes are associated with T3, with higher graphitic crystallinity post ablation. There is some evidence for chemical changes but can mainly be associated with the increased fluence and not necessarily the onset of ablation.

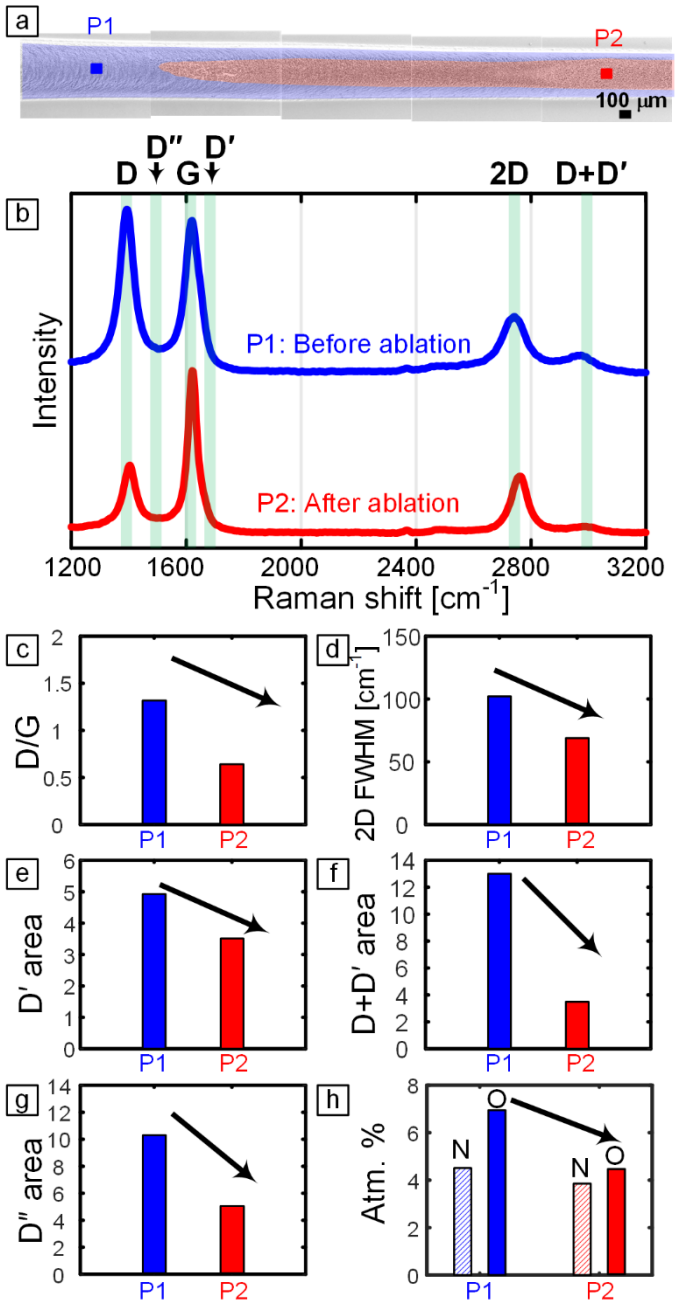

Figure 22: (a) SEM image including location T3 at P = 28W, v = 153 mm/s and γ = 45° with Raman spectroscopy locations P1 and P2, before and after T3 respectively. (b) Raman spectrum at P1 and P2, illustrating the locations of the G, D, 2D, D', D''and D+D' peaks. (c-g) Bar plots showing the difference in D/G peak area ratio, FWHM, D' area, D+D' area, D'' area at points P1 and P2. (h) Bar plot showing the difference in N, O atomic % before and after ablation threshold T3, derived from XPS survey scans.

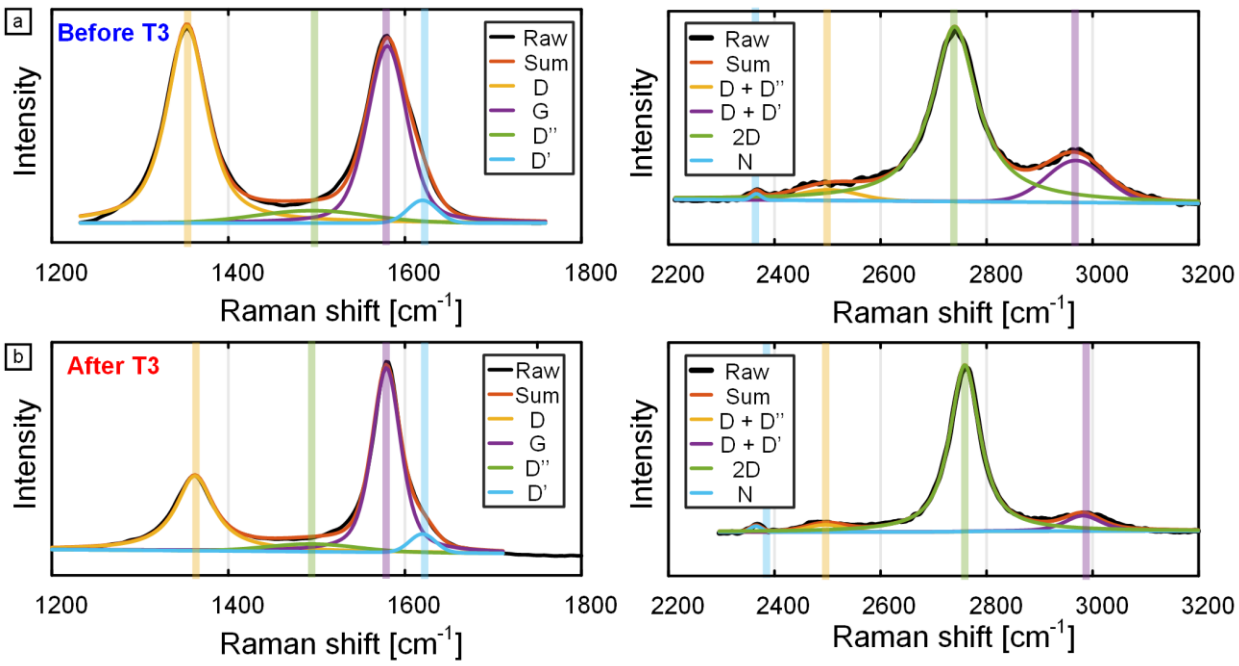

Figure 23: Deconvolution of the Raman peaks at point P1 (prior to ablation T3) and after ablation P2.

Table 1: Deconvolution of peaks from raman spectroscopy

	Parameter	Pre ablation (P1)	Post ablation (P2)
G peak	G peak height	0.910	0.968
	G peak area	60.062	48.609
	G peak FWHM	53.025	38.525
D peak	D peak height	1.020	0.400
	D peak area	78.150	31.126
	D peak FWHM	53.827	51.360
D' peak	D' Height	0.117	0.110
	D' Area	4.928	3.516
	D' fwhm	39.500	34.360
D" peak	D" Height	0.063	0.065
	D" Area	10.306	5.082
	D" fwhm	151.529	120.850
2D peak	2D Height	0.365	0.350
	2D Area	60.000	36.379
	2D FWHM	102.080	68.000
G/D ratio	G/D Int	0.892	2.420
	G/D Area	0.768	1.562
D'/G ratio	D'/G Area	0.082	0.072
	D'/G Int	0.128	0.114
D"/G ratio	D"/G Int	0.069	0.067
	D"/G Area	0.172	0.105
2D/G ratio	2D/G Int	0.401	0.362
	2D/G Area	0.999	0.748
D+D' peak	D+D' area	12.893	3.502

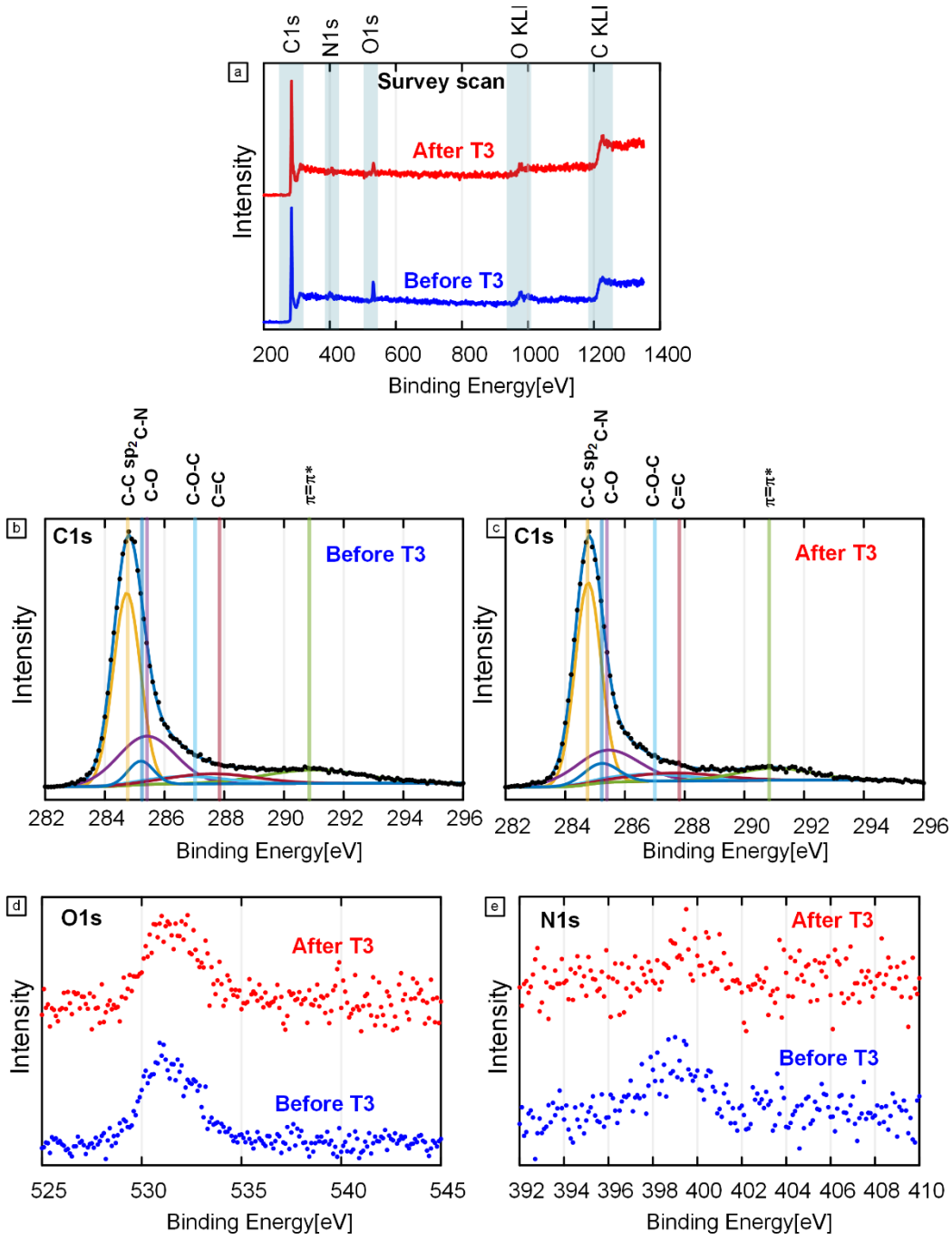

Figure 24: (a) XPS survey scans before and after ablation onset at P = 28W, v = 153 mm/s. (b,c) Deconvolution of C1s core scans before and after ablation illustrating the location of the peaks. (d) O1s core scans before and after ablation onset. (e) N1s core scans before and after ablation onset.

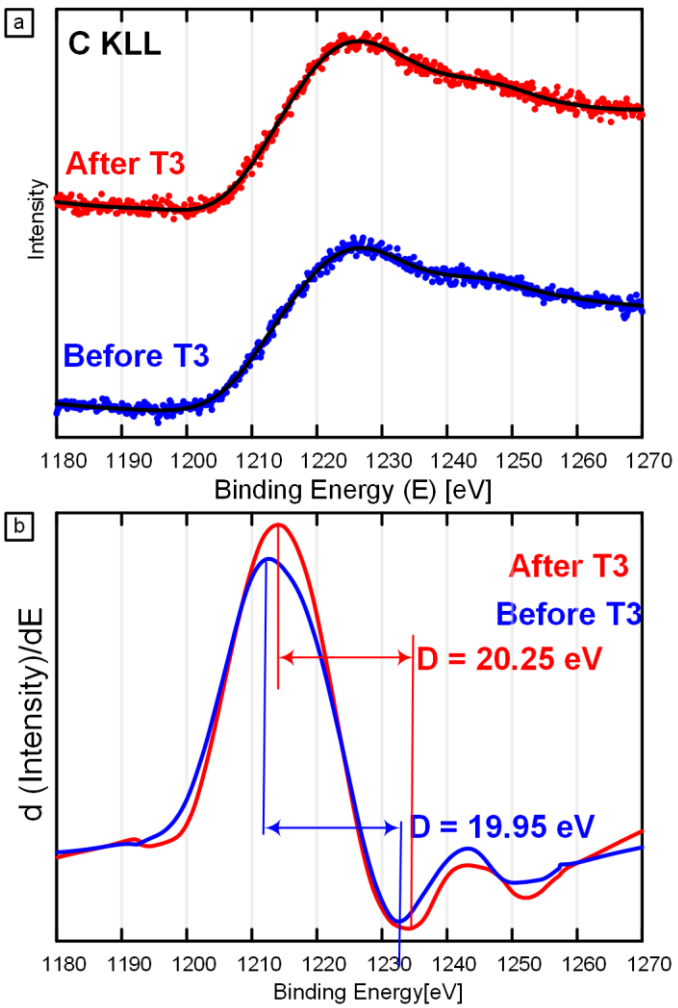

Figure 25: (a) C KLL auger spectrum before and after ablation at P =28W and v = 153 mm/s. (b) the derivative of C KLL spectrum used to estimate the D parameter.

Table 2: Atomic % analysis from XPS survey scans showing elemental analysis before and after onset of ablation.

Atomic %		
	Pre-ablation	Post-ablation
C	88.5338	91.6275
N	4.5136	3.8964
O	6.9526	4.4761

Table 3: Summary from C1s peak deconvolution

	Pre-ablation			
Group	Peak	Position	Area	FWHM
C-C	0	284.736eV	0.859	1.070eV
C-N	1	285.200eV	0.1	1.012eV
C-OH	2	285.400eV	0.459	2.277eV
C-O-C	4	286.700eV	0.1	3.153eV
C=C	3	287.600eV	0.144	3.458eV
pi-pi*	5	291.000eV	0.222	3.967eV
	Post Ablation			
Group	Peak	Position	Area	FWHM
C-C	0	284.765eV	0.861	1.023eV
C-N	1	285.200eV	0.112	1.382eV
C-OH	2	285.400eV	0.338	2.509eV
C-O-C	3	286.700eV	0.1	3.373eV
C=C	4	287.600eV	0.122	3.682eV
pi-pi*	5	291.000eV	0.15	2.972eV

4.7 Speed-dependent Ablation Thresholds

Using SEM and microscopy imaging, the locations of T1, T2 and T3 can be precisely identified along with the area averaged fluence values. These values can be used to investigate whether the occurrence of these thresholds is speed dependent and provide insight into the

influence of process kinetics on the thresholds Figure 26 (a) shows the change in estimated area averaged fluence (F_{Aarea}) with level of defocus and speed. Additionally, the experimental locations (converted to z coordinate) of the T1, T2 and T3 thresholds are marked on the curves to estimate the fluence values at which these transitions occur. Figure 26 (b) shows a plot with the values of the fluence at the transitions for each speed value and hence illustrate the influence of lasing speed on these thresholds. At v = 500 mm/s, the threshold values are estimated to be FT1 = 15 J/cm2 and FT2 = 20 J/cm2, similar in value to what was previously reported. At speeds between 350 mm/s and 500 mm/s, slight increase can be observed in FT1 indicating a weak speed dependence. However, a strong speed dependence is observed with FT2 with the transition happening at higher values of fluence at lower speeds. For example at v = 350 mm/s, FT2 = 38 J/cm2 and FT1 = 19 J/cm2. At speeds between 100 mm/s and 350 mm/s both FT1 and FT3 exhibit speed dependence, showing evidence of kinetics influence at lower speeds.

From SEM imaging of T3 in Figure 18 (a) and Figure 19, it is observed that the distribution of beam intensity and hence fluence affects the T3 transition, since the transition occurs initially at the center and extend across with increased fluence down the lasing path progressively. To precisely map the curves marking the onset of ablation and estimate the onset threshold, we use image processing techniques. This process exploits the change in image contrast accompanying the onset of ablation. The process is presented in Figure 27 and Figure 28. Initially, stitched SEM images of the transition are contrast adjusted as illustrated in Figure 27 (a) for v = 153 mm/s. MATLAB based edge detection techniques are used to detect the edge of ablation as illustrated in the false colored image in Figure 27 (b). To find the values of fluence associated with the transition, a new model of fluence (F) is used to create a spatial fluence map, as shown in Figure 27 (c) and hence an iso-fluence map that is generated and aligned with the SEM images, shown in Figure 27

(d). The area averaged fluence F_{Aavg} which is only a function of defocus (and hence x') is also shown in Figure 27(d). The values for centerline 2D fluence (F) and the area averaged fluence F_{Aavg} are both plotted in Figure 27 (f) as a function of x' and corresponding defocus z. Using the SEM imaging, imaging processing and the 2D and area average fluence modeling, the fluence values at the onset of ablation can be precisely identified. For v = 153 mm/s, F2DT3=42 J/cm2 and FT3=31 J/cm2. This process is repeated for other speeds with detectable ablation, and the results are plotted in Figure 27 (g). Similar to FT2, a speed dependence is also observed, with the value of the F2DT3 = 52 J/cm2 at v = 100 mm/s (Figure 28) and F2DT3 = 30 J/cm2 at v = 270 mm/s. Another observation from SEM imaging is the occurrence of both ablation and fiber formation at a speed v = 270 mm/s as illustrated in Figure 29. This important finding indicates that at certain conditions ablation can initiate prior to fiber formation and lead to the ablation of LINC fibers.

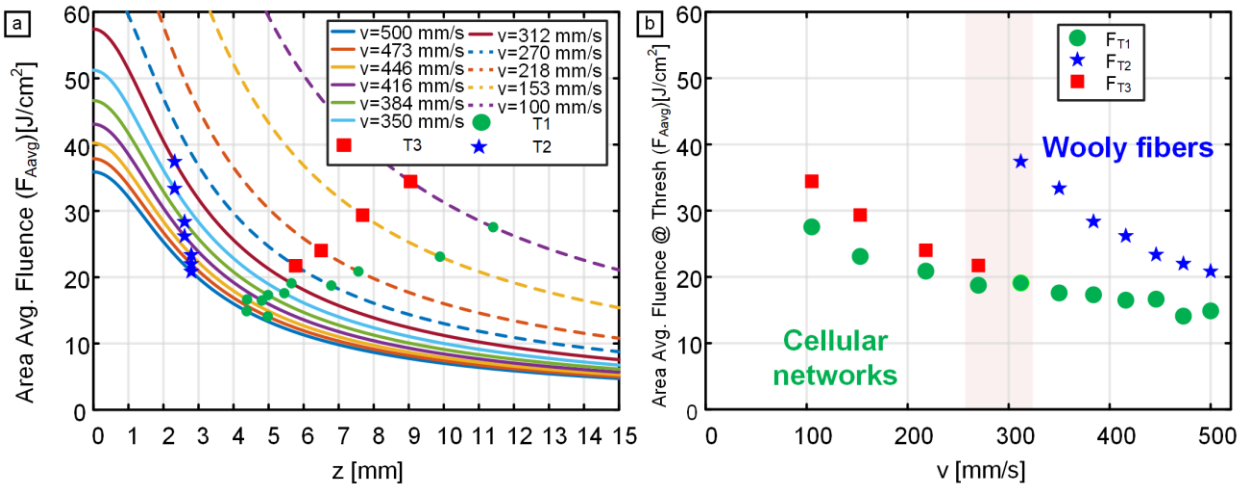

Figure 26: (a) Plot of estimated area averaged fluence F_{Aavg} as a function of defocus z at different speeds , with the transition locations T1,T2 and T3 marked on the curves at each speed. (b) Plot illustrating the values of area average fluence at T1,T2 and T3 for each speed, showing the influence of speed on the fluence at transition.

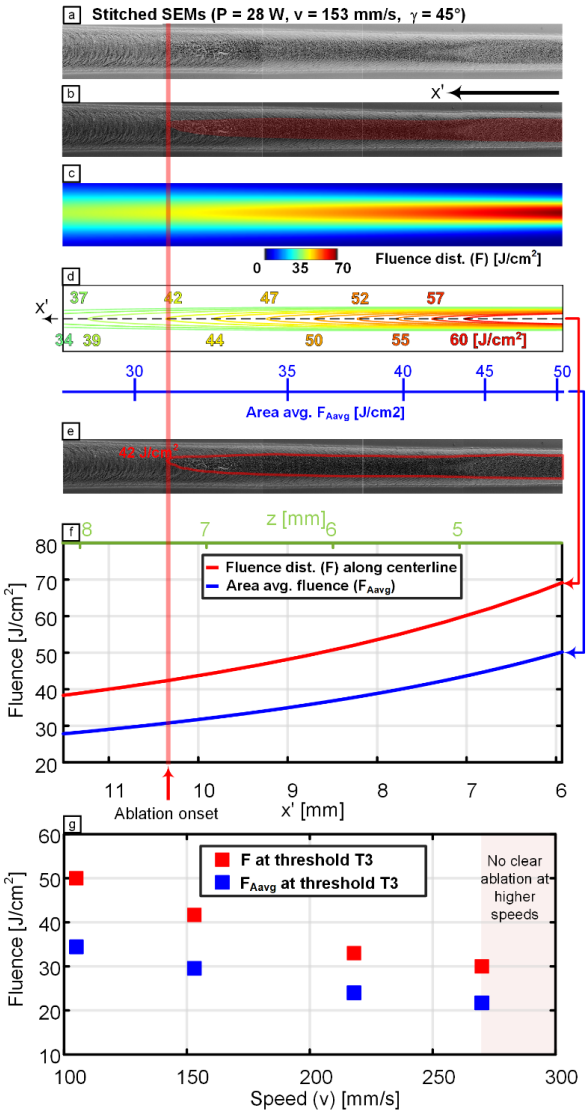

Figure 27: Figure illustrating process to identify the fluence thresholds at onset of ablation. (a) SEM image at P = 28W and v = 153 mm/s at T3. (b) SEM image with false coloring, with the red areas marking the edge of areas with ablated LINC, identified with edge detection methods. (c) Estimated fluence distribution (F) corresponding to previous figure. (d) Isofluence lines at area corresponding to (b,c) with values of area averaged fluence F_{Aavg} at equivalent locations below. (e) SEM image with overlaid edge of ablation, identified in (b). (f) Plot of fluence distribution F along lasing path center line and area averaged fluence F_{Aavg} as a function of defocus z and correspond x' values with location of ablation onset T3 marked. (g) Plot of values of fluence and area averaged fluence at ablation thresholds as a function of lasing speed, illustrating speed dependence and the lack of clear ablation at speeds higher than v = 300 mm/s.

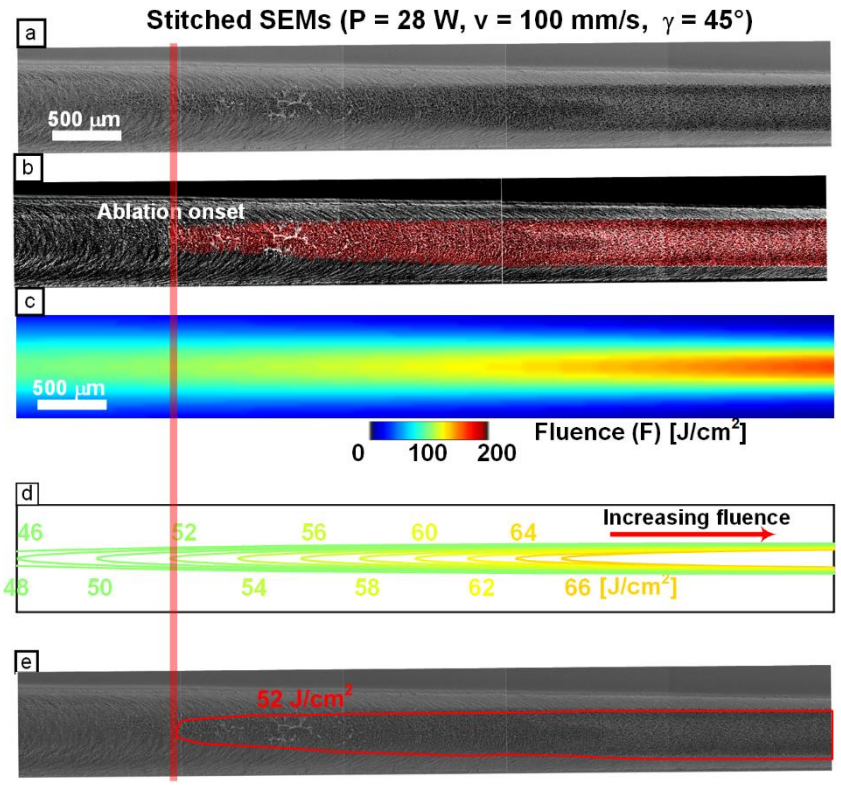

Figure 28: (a) Stitched and contrast adjusted SEM image at P = 28W, v = 100 mm/s/ (b) Estimated edge of ablation using computer based edge detection. (c) Estimated contour surface of fluence distribution corresponding to SEM image. (d) Isofluence lines of corresponding area. (e) SEM image with overlaid edge of ablation, identified in (b).

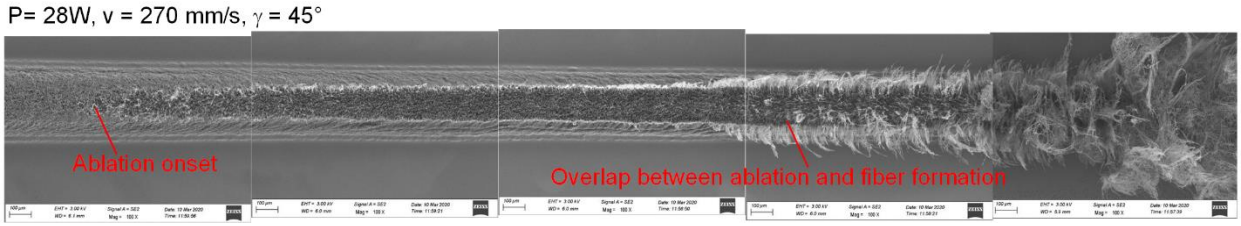

Figure 29: SEM image at P = 28W, v =270 mm/s illustrating the onset of ablation and overlap between LINC ablation and fiber formation.

4.8 Morphology Dependent Resistivity

To test the effect of T1 and T3 transition on resistivity, LINC electrodes were lased at flat conditions and their resistivity estimated from cross section area data at P = 28W and v = 153 mm/s and v = 270 mm/s and different defocusing values. The results are shown in Figure 30 (a, b). The T3 transition defocus values match the values resulting from the tilted lasing. Post ablation, a sharp drop in resistivity is observed which tends to stay constant after, with resistivity dropping to 0.27 Ohm.cm at v = 153 mm/s and a value of 0.33 Ohm.cm at v = 270 mm/s.

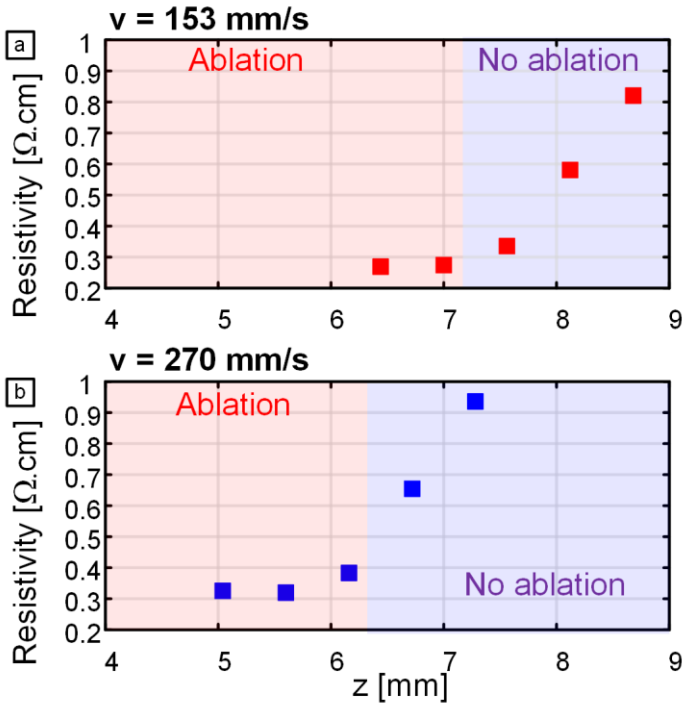

Figure 30: Plots of experimentally estimated bulk resistivity of flat lased LINC electrodes at difference defocus levels, illustrating the effect of ablation on resistivity at speeds at speeds (a) v = 153 mm/s and (b) v = 270 mm/s.

4.9 Simulation to Explain Kinetic Effects

From the previous analysis and experiments, a number of observations can be made. From the imaging it was observed that no fiber formations at speeds below v = 300 mm/s. Additionally, it was observed that T1 is not strongly speed dependent at low speeds, in contrast with T2 which is speed dependent below v = 500 mm/s indicating a kinetic influence. We identify a new threshold for ablation of LINC along the lasing path at low speeds starting at v = 312 mm/s, revealing a hierarchical porosity with increased ablation. The fluence at ablation conditions is also identified revealing a speed dependence as well. It is clear that speed has a large influence on the LINC process due to the different kinetic conditions at equivalent fluence values. To get more insight into the influence of speed of the actual thermal kinetics, we use thermal FEM simulations of the tilted lasing. It should be noted that polymer lasing is a complex process with laser material interactions, phase and chemical transitions happening at different time scales and are extremely challenging to model accurately.[73] The current model is highly simplified, however it should provide some useful insight into the process kinetics. The objective of the model is to recreate the lasing conditions used in the experiments and identifying the temperatures and temperature rates at points in the simulation corresponding to the locations of the experimentally identified thresholds.

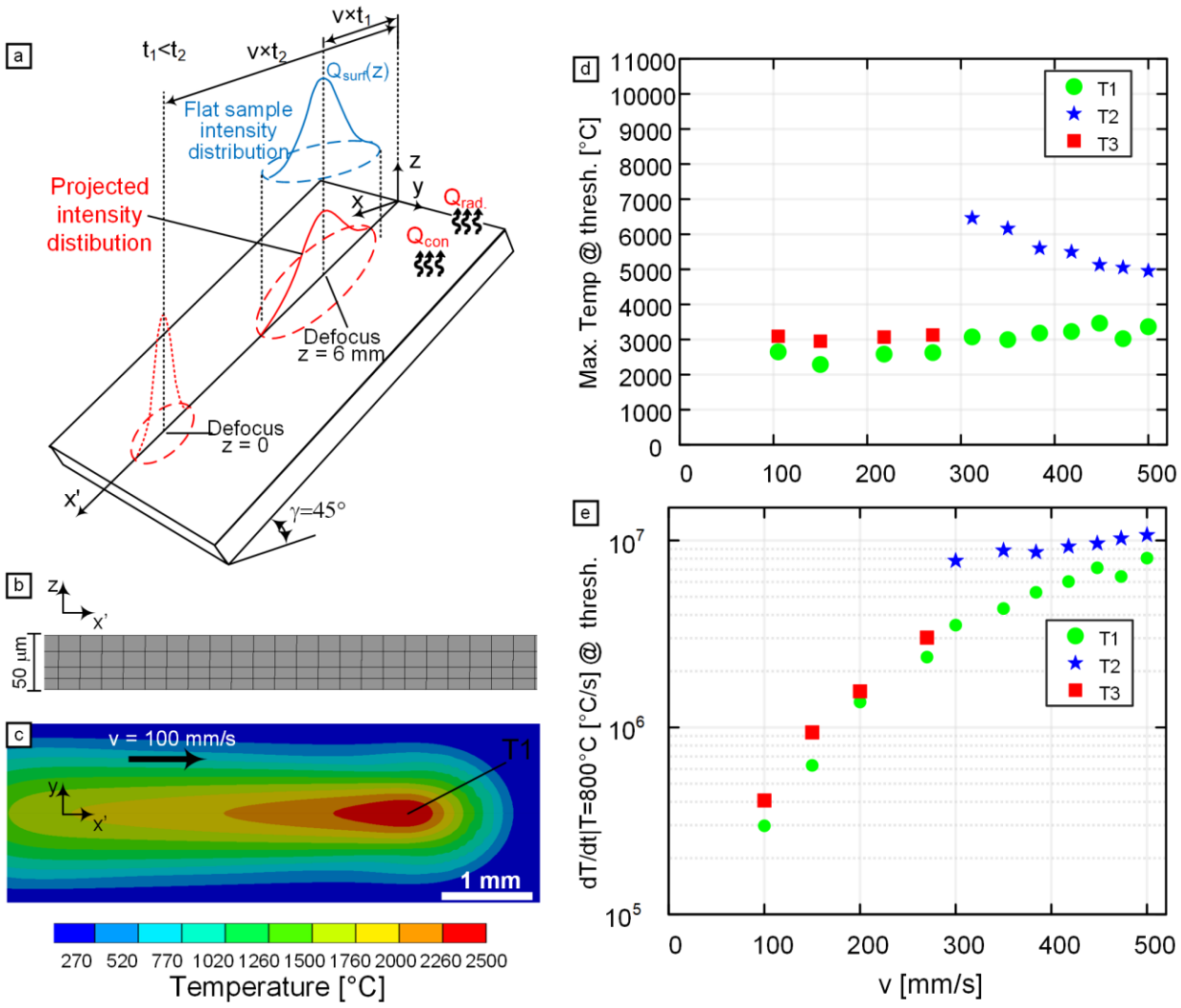

Figure 31: (a) Schematic illustrating the boundary conditions used to simulate tilted lasing. (b) Sample side view of mesh illustrating the sheet thickness. (c) Sample of temperature contours at P = 28W, v = 100 mm/s at location T1. (d) Plot illustrating simulation estimated maximum temperatures corresponding to experimentally identified locations T1,T2 and T3 as a function of speed. (e) Plot illustrating simulation estimated temperature increase rates at T = 800 °C corresponding to experimentally identified locations T1,T2 and T3 as a function of speed.

A schematic of the model boundary conditions is shown in Figure 31 (a). The beam is modeled as a translating Gaussian heat flux distribution projected along the tilted sample ($\gamma = 45°$) with speed v. The Gaussian beam parameters used are derived from the experimental beam characterization. A sample of the mesh showing the meshing across the thickness is additionally shown in Figure 31 (b). The material properties are modeled to be temperature dependent to account for phase transition effects as illustrated in Figure 32. Additionally, the model takes into account radiation and convection effects. The simulations are run at conditions corresponding to the experimental conditions (P = 28W, v = 100-500 mm/s). For each condition, the temperature and temperature rate at the points corresponding to T1, T2 and T3 are probed with time in the simulation. A sample of the temperature contours is shown in Figure 31 (c) at conditions v = 100 mm/s and location T1. From these results, the maximum temperature (T_{max}) is derived.

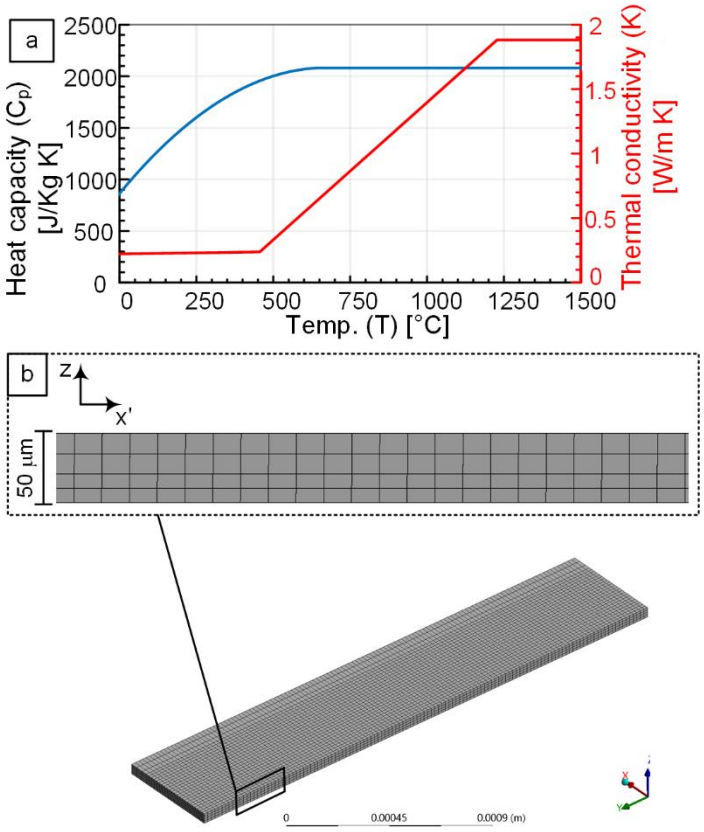

Figure 32: (a) Temperature dependent boundary conditions used in the simulations. (b) Sample of mesh used.

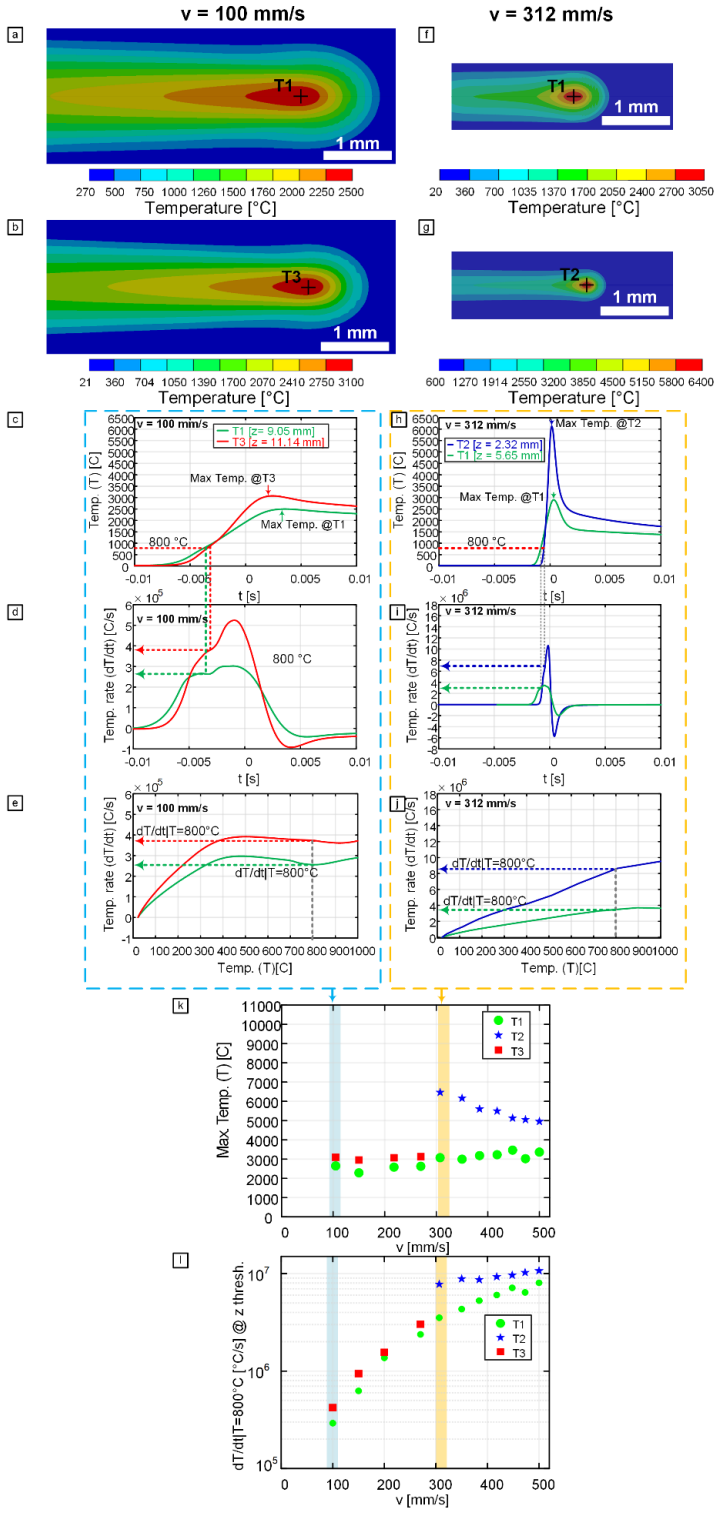

Figure 33: Schematic illustrating the process of deriving the maximum temperature and dT/dt | T = 800 °C from temperature at a point data at T1,T2 and T3 for two conditions (a-e) v = 100 mm/s and (f-j) v = 312 mm/s with the results for all conditions summarized in (k,l)

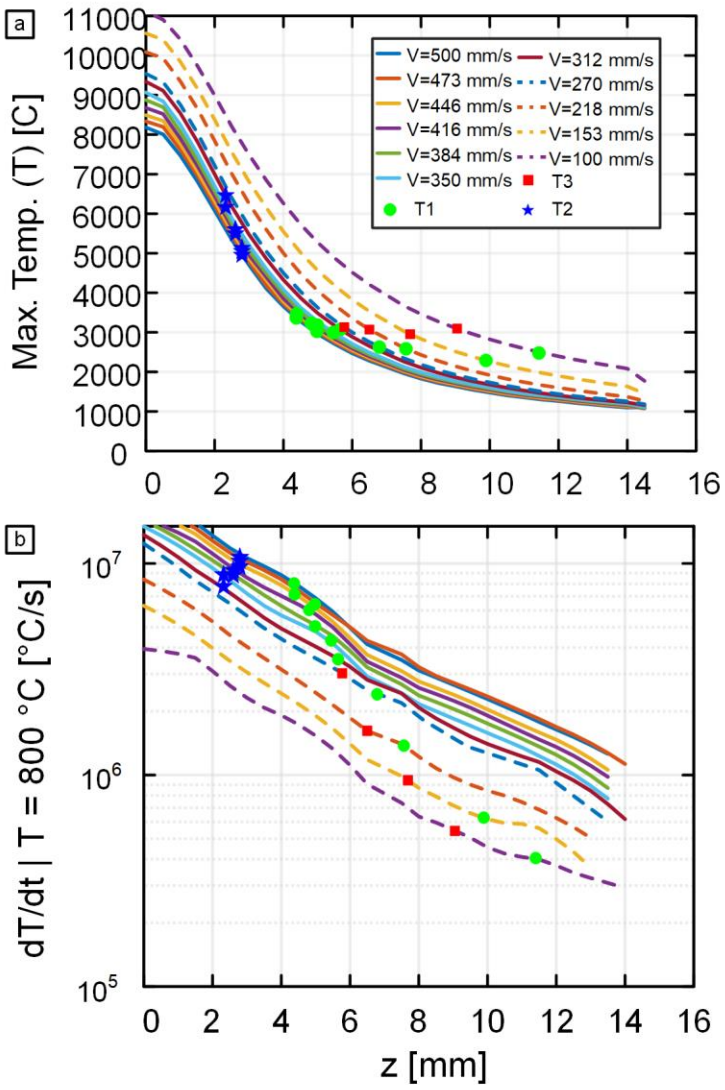

Figure 34: The maximum temperature and temperature rate at different levels of defocus and speed with the location of the T1, T2 and T3 thresholds marked.

Additionally, to get a measure for the rate of change of temperature at a point, the time derivative of temperature at T = 800 °C is also derived for each threshold point at each speed. This temperature is selected to represent the carbonization temperature of polyimide, which is typically reported to be between 700 °C and 1000 °C.[76,78,93] The overall approach is summarized in Figure 33. The results of this analysis are represented in Figure 31 (d, e) and corresponding figures

as a function of defocus and speed are shown in Figure 34. Figure 31 (d) shows the plot for the maximum temperature at the points corresponding to the T1, T2 and T3 for the different speeds. Figure 31 (d) represents the temperature rates at the transitions T1, T2 and T3. From Figure 31 (d) it is noted that the maximum temperatures for the T1 transition range between 3400 °C and 3100 °C between v = 300 and v = 500 mm/s and between 2300 °C and 2500 °C at lower speeds. Overall, the maximum temperature at the threshold T1 shows little speed dependence and occurs at around 3000 °C on average. The T3 transition shows a similar trend where it occurs at slightly higher temperatures than T1 and is between 3000 °C and 3100 °C at speeds lower than 300 mm/s. However, for the T2 transitions, the maximum temperatures start at around 5000 °C at v = 500 mm/s and increase to a value of around 6400 °C, showing a strong speed dependence. Figure 31 (e) shows the corresponding temperature rates at carbonization for the same points. The rates at carbonization range are estimated to span two orders of magnitude between 10^5 and 10^7 °C/s which agree with estimated temperature increase rates of laser heating of polymers reported by others.[67,102] From the results shown in Figure 34, it is noted that in general, higher speeds are reflected with higher temperature rate increase but lower maximum temperatures, illustrating the effect of lasing speed on kinetics. From Figure 31 (e), the rates at T1 vary strongly with speed, showing an almost piecewise linear relation when viewed in log scaling, increasing from at 3e5 at v = 100 mm/s and 8e6 at v = 500 mm/s. The rates at T3 are highly speed dependent, starting at 4e5 at v = 100 mm/s and 3e6 at v = 273 mm/s. The temperature rates at carbonization are less speed dependent for T3, slightly increasing between 0.8e7 at v = 300 mm/s to 1e7 at v = 500 mm/s.

The low speed dependence of maximum temperature for T1 (transition from porous to cellular networks) and T3 (Onset of ablation) suggests that these transitions are mainly controlled by temperature and not necessarily by temperature increase rate, implying energetic control at

these conditions. To further elaborate on these results, we correlate these two transitions to two particular phenomenon: the graphitization of the polyimide (following carbonization) at T1 and the ablation of the formed graphite/graphene at T3. Previous research has shown that graphitization of polyimide occurs at a temperature between 2500 °C and 3000 °C.[76] This would explain the appearance of the 2D peak at T1, which is associated with the onset of graphitization and the increase in degree of graphitic sheet stacking[99], and the observed drop in resistivity, which was reported previously by the authors. This also explains the increased opacity observed under optical imaging.[97] Additionally, ablation studies for graphite usually report that at a temperature of 3300 °C significant ablation is observed, even with CW laser based heating studies.[103,104] These temperature values are very close to the temperatures estimated by the simulations, and hence support these conclusions. The ablation is particularly clear at lower speeds due to the longer dwell times by the laser spot and the laser spot heat affected zone. This potentially explains why ablation is not apparent at speeds higher than 300 mm/s.

Alternatively, the results for the T2 transition (from cellular networks to wooly fibers), which show that the T2 transitions mainly occur at a rate around 0.8e7 and 1e7 °C/s, suggest a temperature rate limited process at these conditions and illustrate the influence of kinetics on this transition. It is generally been suggested that this transition to fibers is related to a number of phenomenon associated with the rapid rate of gas released, polyimide backbone bond stability and the mechanical properties of the polyimide.[60,97]

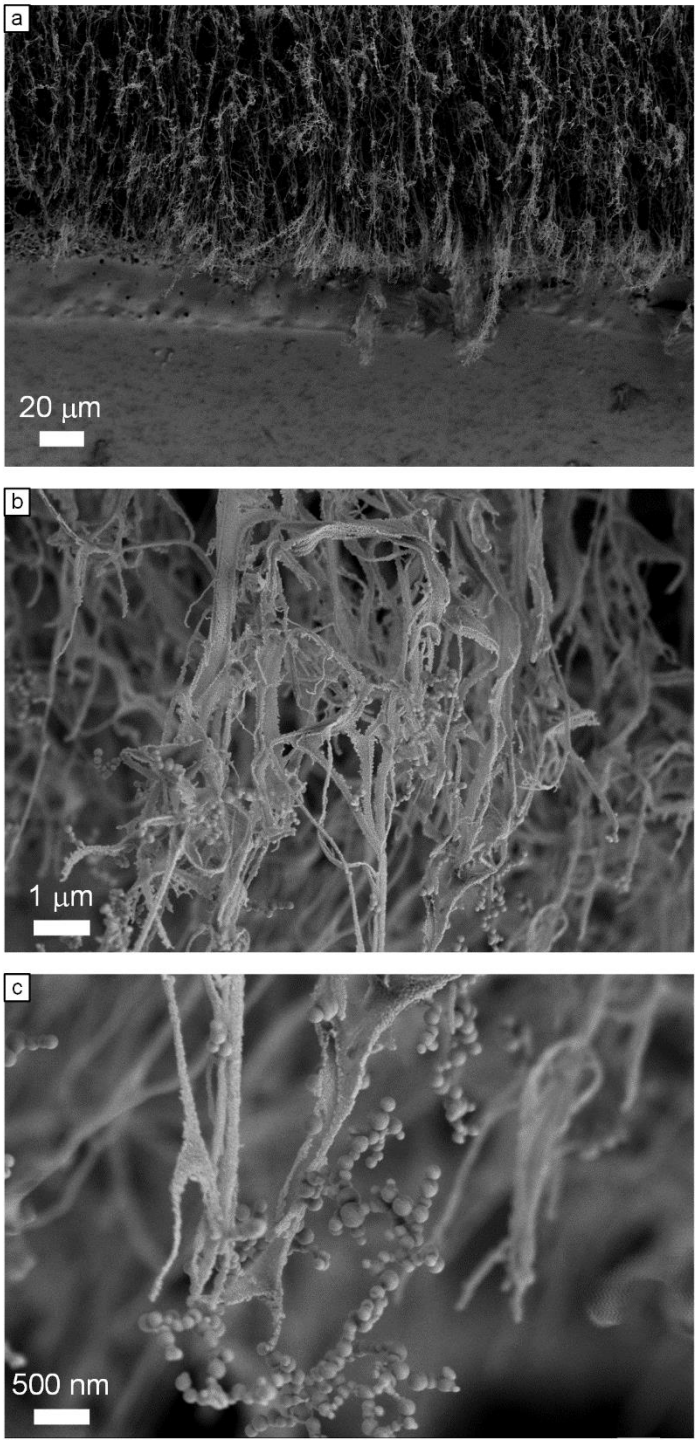

Figure 35: SEM images illustrating the formation of nanospheres and webs, which suggest viscoelastic jetting of partially carbonized polyimide at T2.

To understand this transition and how it is different from the other transitions, it is useful to consider the physical phenomenon involved in the process leading to the jetting. Pore nucleation, pore growth due to reaction products, the viscoelastic nature of polyimide and the more brittle nature of graphitic materials.

Typically, the phenomenon of jetting is studied and understood in terms of three dimensionless numbers: the Deborah number, Ohnesorge number and Weber number.[105] The Deborah number is defined as the ratio of the characteristic relaxation time for a viscoelastic material (which typically decreases with increasing temperature) and the characteristic time scale for a process, which can be the time associated with the material response.[106] When the Deborah number is low, the material behaves more like a fluid. At a high Deborah number, the material demonstrates a more solid like behavior In the case of fiber formation, the response is driven by the rapid temperature increase (due to the shorter dwell times) and hence pressure increase in the pores due to the gases released during the process. At rapid temperature increases and higher gas release pressure, driven by a chemical reaction threshold which is likely governed by polyimide backbone stability, the Deborah number is likely to be very low. This is due to the shorter relaxation time of the polyimide and high pressure increase and release driven by the high temperature rates and short laser dwell times. At the low Deborah number and incomplete carbonization of the polyimide and gas release, the phase transitioning polyimide is likely to jet out, leading to fiber formations. The size and shape of the resulting jetting material are typically governed by the Ohnesorge number and Weber number.[105,107] The Ohnesorge number represents the ratio between the viscous forces to inertial and surface tension forces. The Weber number represents the ratio between kinetic effects and surface tension effects for a droplet. These numbers, combined with other non-linear effects, decide whether the ejected material will form

filaments/fibers or droplets as well as the size of the fibers. It is interesting that the LINC fibers exhibit filamentous shapes and interconnected webs with spherically shapes in between as shown in Figure 35, which has also been observed in nonlinear viscosity jets seen with polymeric flows[108] and sneeze jets[109]. This phenomenon likely don't occur at the earlier transitions due to higher Deborah numbers, low gas release pressures and longer dwell times (Figure 16) that graphitize the polyimide before the beam coincides with a point. If the dwell time is long and the heating rates are low, the material is likely to graphitize and lose its viscoelastic properties due to the phase change and hence no jetting would occur. This conclusion is further supported by the Raman spectrum of the nanocarbon fibers reported previously by the authors which are characterized by the disappearance of the 2D peak[97], implying that the nanofibers are incompletely graphitized polyimide that are jetted prior to graphitization. Interestingly, this kind of analysis have similarly been used to study jetting and fragmenting non-Newtonian fluids. Examples are the study volcanic magma bubble formation and fiber fragmentation[106,110], sneezing[107,109], ink jet printing[111], polymer fluids[112], some of which at certain conditions, can generate interconnected filaments like the nanofibers observed after the T2 transition in LINC.[108,112–114].

4.10 Conclusions

Using our unique tilted lasing approach, we shed insight into the fundamentals of the process of laser induced carbonization of polyimide using continuous CO2 lasers. This unique approach allows identifying the morphological transformations of LINC and correlating them with fluence values, furthermore, we investigate the effect of lasing speed and hence process kinetics

on these morphological transitions. In addition to identifying how the fluence values at morphological transitions are affected by speed, we develop a unique approach to incorporate the experimental results with thermal simulations to get more insight on the process and identify whether a transition is energetically driven or kinetically driven. Using the simulation results combined with Raman and XPS analysis, we identify that the two transitions, the transition from a porous to cellular morphology and the onset of ablation are likely to reflect two physical phenomenon: the graphitization of polyimide and the ablation of the graphitized polyimide respectively. These transitions are shown to be temperature dependent and the results agree with experimentally reported temperatures for these phenomenon. The cellular to fiberous networks transition is found to be mainly driven by the rate of temperature increase and we propose that it is the results of a decreased Deborah number combined with the rapid release of gas associated with the thermochemical stability of the polyimide. The resulting morphology is the result of the jetting of the incompletely carbonized polyimide, which acts like a non-Newtonian fluid jet which manifests with the formation of filaments and webs of nanocarbons.

5.0 Low Impedance Laser-induced Graphene Microelectrodes with Relase-speed-Dependent Properties

5.1 Introduction

The flexibility of the LINC process in addition to the functionality of the carbon materials enable a wide range of applications like heaters for efficient boiling applications[115], wearable electronics [116], sensors [117], microfluidics [49,58,118], drop manipulation [119], battery applications[120] and actuators[121]. Additionally, the porous nature of LINC based electrodes and their electrochemical sensitivity make it highly suitable for biosensor based applications [49,98,122,123] LINC based sensors have been used for sensing biomolecules like dopamine [98,123,124], uric acid [49] and interleukin [125]. LINC based biosensors are typically fabricated by laser rastering areas of LINC on flexible polymers like polyimide. To enhance LINC sensing performance, the precursor polymer can be doped [98] or materials like metal nanoparticles [126] or conductive polymers like PEDOT [124] can be integrated within the LINC material. In this work, we focus on the synthesis of single line mircro-electrode based sensors (in contrast to area based LINC sensors), to minimize electrode size, towards miniaturizing the technology, which is a necessary condition for implantable microelectrode based sensors. Additionally, single line lasing allows us to fully understand the effects of the laser parameters on electrodes without the influence of laser pass overlap or proximity effects, which dominate area rastering. Moreover, we focus on enhancing device performance through reducing electrode electrical resistivity and controlling surface morphology.

Efforts for enhancing electrode electrical conductivity take multiple approaches like increasing laser power and lowering speed [63], design of experiments and machine learning,[127,128], lasing with multiple passes[84], overlap [129]. Some of these approach optimize LINC properties based on areas and use sheet resistance as a measure of resistance, which assumes a thin film of LINC and isn't practical for electrode applications.

Here, we enhance the electrode electrical conductivity by controlling the laser speed and relase speed when fabricating the electrodes. This is advantageous in two aspects: controlling graphitization levels of the LINC electrode and controlling the surface morphology of materials through ablation of the electrode. Overall this approach allows controlling electrode surface and bulk morphology, conductivity, crystallinity/atomic structure. Additionally we demonstrate the effect of relasing on the neural testing capability of functional LINC electrodes. Under this approach we reveal a more comprehensive picture of the process of LINC formation and the structure of surface and inner morphology and we shed light onto factors influencing the effective conductivity, electrochemical sensitivity and the effect of relasing.

5.2 Relasing for Controlling Surface and Inner Morphology of LINC Electrodes

In a typical LINC line fabrication process, a laser beam with power P lases a polyimide sheet with speed v_1. The sample surface is at a distance z from the beam waist (assumed Gaussian) which decides beam spot size 2w. A schematic of the experimental setup is shown in Figure 36 (a). A continuous CO_2 laser (λ=10.6 μm) is used for this study which has been characterized to estimate its beam parameters in previous work. The laser profile is shown in Figure 36 (d). Upon beam exposure, the polyimide absorbs the laser light wavelength λ=10.6 μm strongly .[68] This is

followed by a temperature increase in the material which thermally drives the carbonization of the polyimide. After this first lasing pass, a second lasing process is followed with speed v_2 at the same power P as presented in Figure 36 (b) until it is fully relased.

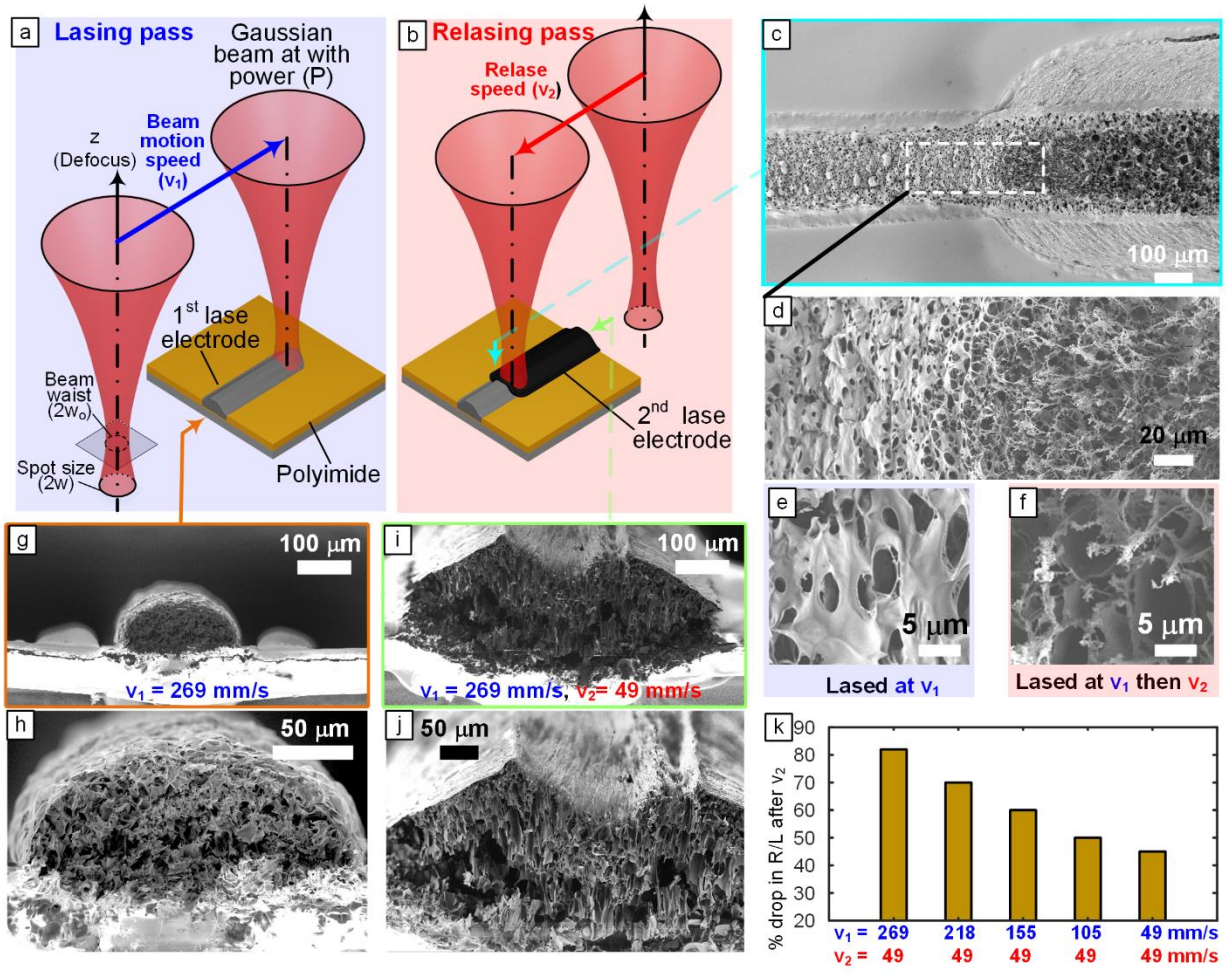

Figure 36: Schematic illustrating the first lasing step at speed v_1 (a) and speed v_2 (b). (c) SEM image of interface between line lased at P = 12.5 W and z = 9 mm and v_1 = 269 mm/s and the remaining line section relased at v_2 = 49 mm/s. (d) SEM image illustrating the influence of the relasing on surface morphology with higher resolution imaging in panel (e) and ((f). (g,h) SEM images of cross section of single lased LINC lines at v_1 = 269 mm/s. (i,j) SEM images of cross section of relased LINC lines at v_1 = 269 mm/s and relase speed v_2 =49 mm/s. (k) Bar chart illustrating the influence of relasing on electrical resistance reduction.

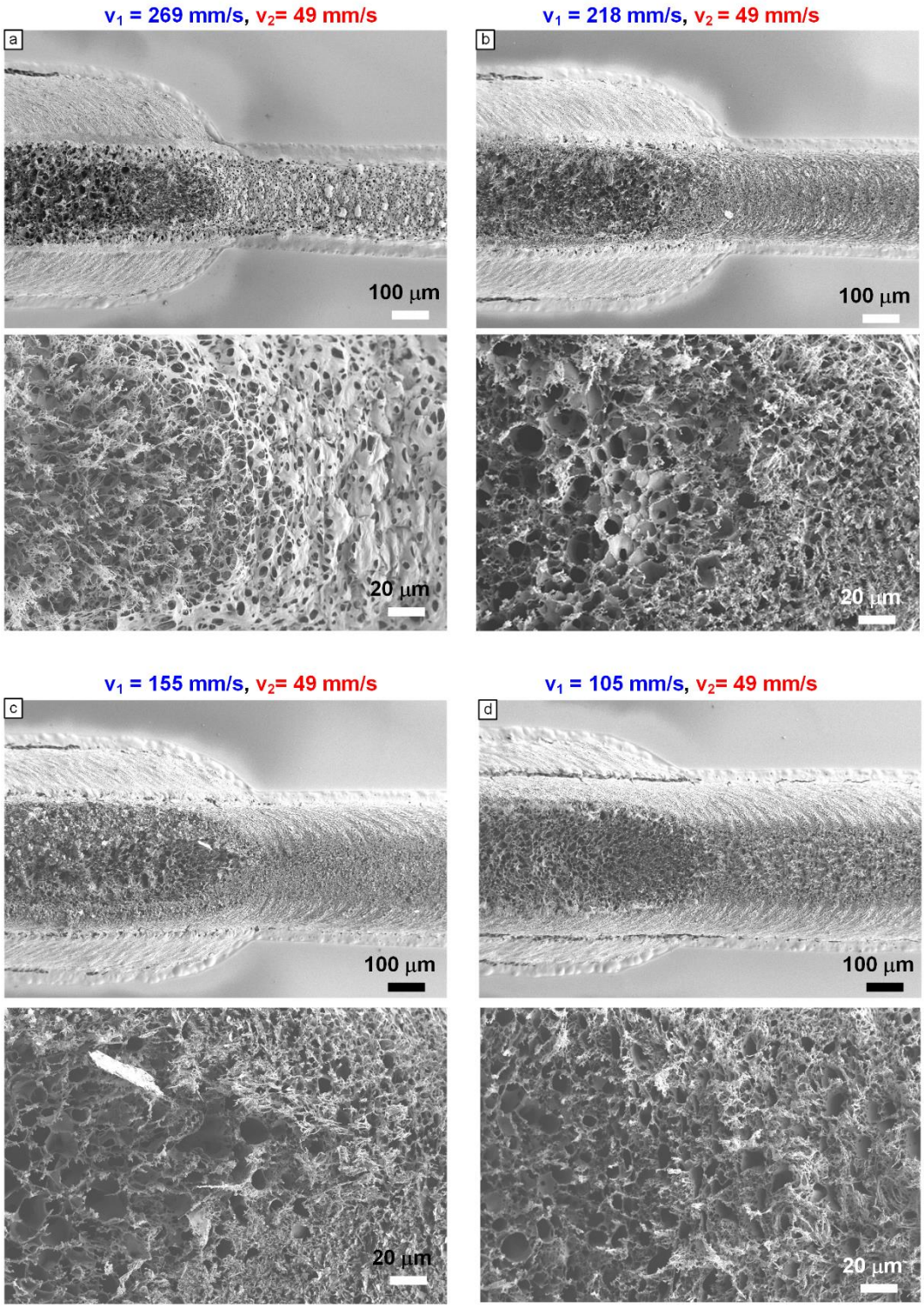

Figure 37: SEM images of LINC lines lased at P = 12.5 W, z = 9 mm (a) v_1 = 269 mm/s , (b) v_1 =218 mm/s, (c) v_1 = 155 mm/s and (d) v_1 = 105 mm/s and then relased at v_2 = 49 mm/s showing the interface between the lased segment and relased segment.

To illustrate the effects of relasing, the second lasing process is halted during the process and imaged using SEM at the interface. These lines are lased using laser conditions P = 12.5 W and different v_1 ranging between 269 mm/s and 105 mm/s and a fixed v_2 = 49 mm/s. The SEM images are presented in Figure 36 (c) and Figure 37. Figure 36 (c) demonstrates the interface between LINC lines resulting from a single lase and the relased and demonstrates the effects of the relasing step: ablation of the porous surface of the LINC lines and an increase in the surface size and width of the LINC lines. The single LINC lines resulting from a single lase at v_1 = 269 mm/s demonstrates a porous surface morphology as shown in SEM image Figure 36 (f). The ablation reveals cellular network features as demonstrated in Figure 36 (e).

Figure 37 (a, b, c, d) shows the influence of the second lasing step on LINC lines lased at slower speeds, in which the surface morphology transitions from a porous surface morphology into a cellular morphology and an ablated morphology at even lower speeds. The relasing pass generally results in ablation on the top layer of the LINC lines and the increase of the width of the lines, an effect which decreases as v_1 approaches v_2. It is also clear from the SEM images that the extent of ablation in the relased lines is more extensive at lower v_1 speeds. Cross sectional SEM imaging of the LINC lines reveals the inner morphology of the LINC lines and the influence of relasing. SEM imaging of the cross sections of LINC lines lased at v_1 = 269 mm/s and another line lased at the same v_1 and then v_2 = 49 mm/s are shown in Figure 36 (g, h) and Figure 36 (i, j) respectively. The images demonstrate the increase in cross section size and change in shape of the LINC lines after relasing. The lines are originally dome shaped with a porous outer shell, upon relasing the line width increases and an ablation crater is revealed on top of the line as well as some change to the inner morphology.

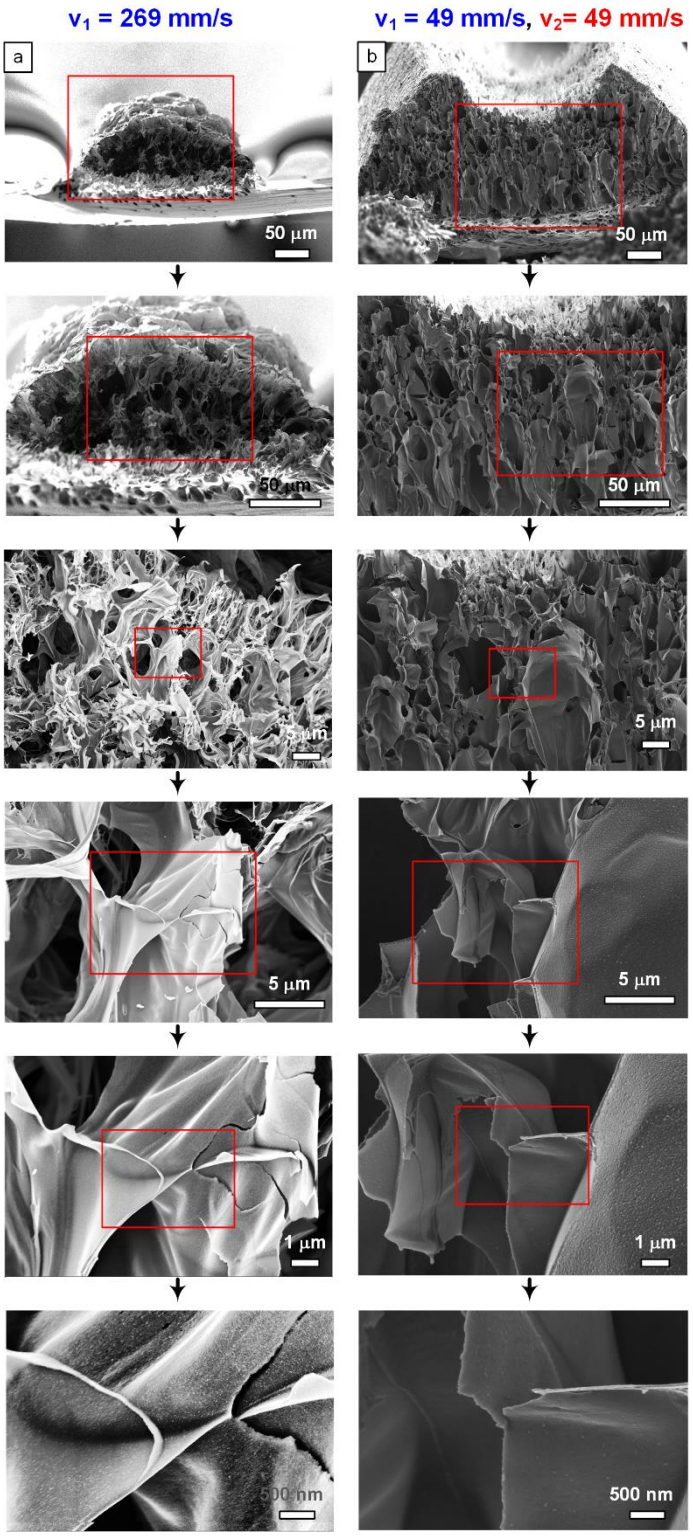

Figure 38: SEM showing mechanically fractured LINC lines lased at conditions (a) v_1 = 269 mm/s and (b) v_1 = 49 mm/s, v_2 = 49 mm/s illustrating the inner structure of LINC lines.

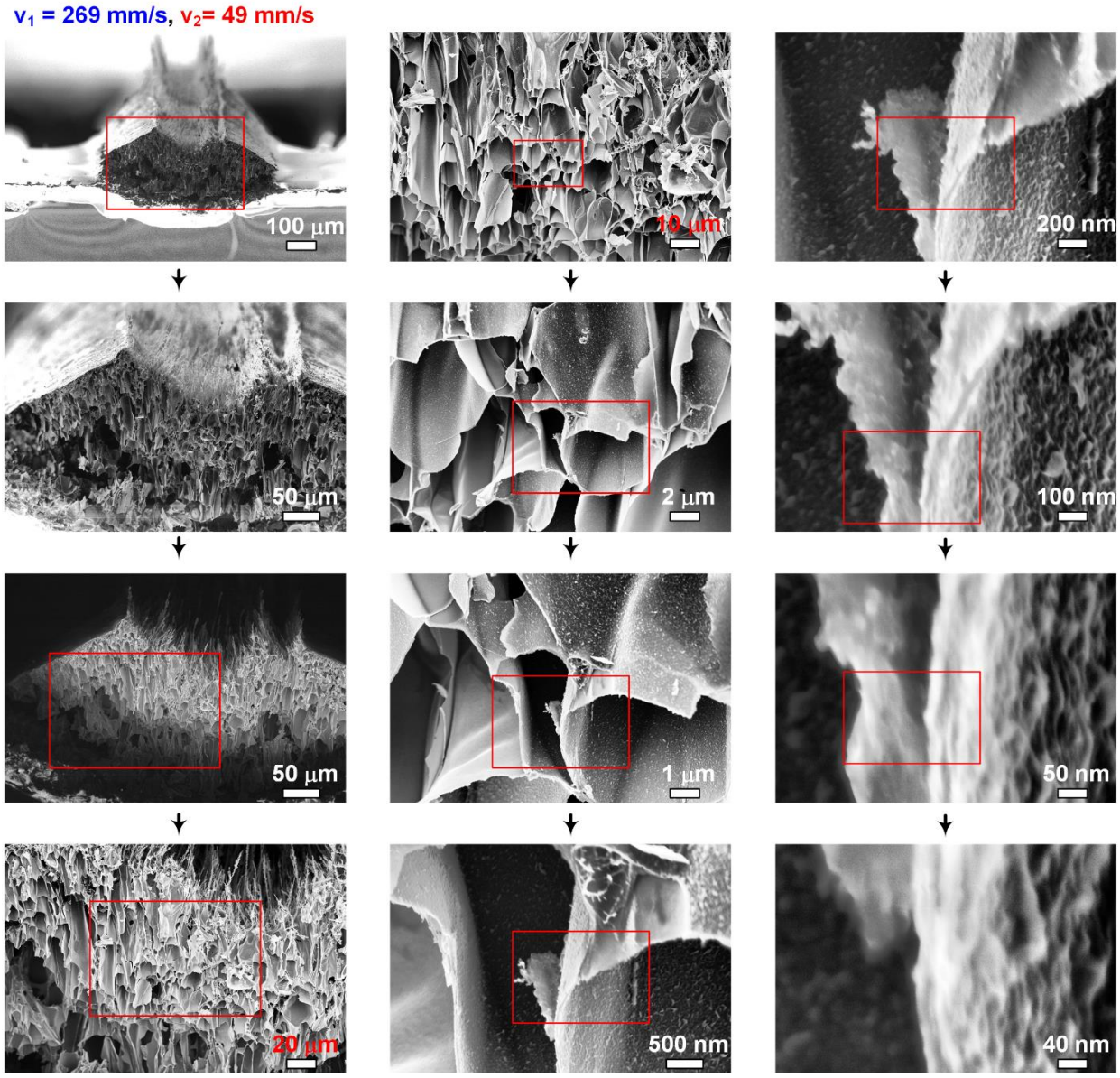

Figure 39: SEM showing mechanically fractured LINC lines lased using conditions P = 12.5 W v_1 = 269 mm/s and v_2 = 49 mm/s illustrating the inner structure of LINC lines and the nanoscale thickness of the inner pore walls.

High resolution SEM imaging of the cross sections of mechanically fractured LINC lines are also imaged to reveal more detail of their inner morphology in Figure 38 (a, b).

The images reveal that the volume of the cross sections of LINC lines are mostly empty and are composed of cells/pores with very thin walls. Some difference in the inner morphology is noted between the cross section of the lines lased at v_1 = 269 and the lines at v_1 = 49 mm/s and v_2 = 49 mm/s. In the first case the cell features aren't clearly directional and feature more wrinkles and a porous outer wall structure with fiberous features underneath. On the other hand, the relased case reveals anisotropic features with a lot of the cell walls having a vertical alignment and an ablated top. Additional high resolution SEM imaging in Figure 39 reveals that the thickness of the cell walls range between 20-50 nm. In addition to the surface morphological changes due to relasing, there is also a clear resistance per length drop due to the relasing step, illustrated in Figure 36 (k), with resistance per length drops going from a value of 80% at v_1 = 269 mm/s, v_2 = 49 mm/s and 40% at v_1 = 49 mm/s and v_2 = 49 mm/s.

5.3 Relasing Speed is a Key for Lowering LINC Electrical Resistivity

While relasing affects the line electrical resistance, does it affect the effective electrical resistivity of the material? How low can the effective resistivity be without excessively damaging or cutting the electrodes? To answer that question another study with fixed v_1 and changing v_2 is conducted. To select v_1, a single pass speed study is completed first with the results shown in Figure 40 (a, b). Figure 40 (a) demonstrates the effect of the lasing speed on the resistance per electrode length at fixed power P = 12.5 W and z = 9 mm. The onset of damage through excessive electrode fracture and cutting is denoted in the figure. The resistance per length (R/L) is noted to

drop from a value of 43 Ω/mm at v_1 = 105 mm/s to a value of around 14 Ω/mm at v_1 = 49 mm/s. The trend shows that resistance per length can potentially be lower, however the line would eventually be excessively damaged due to fracture or cutting.

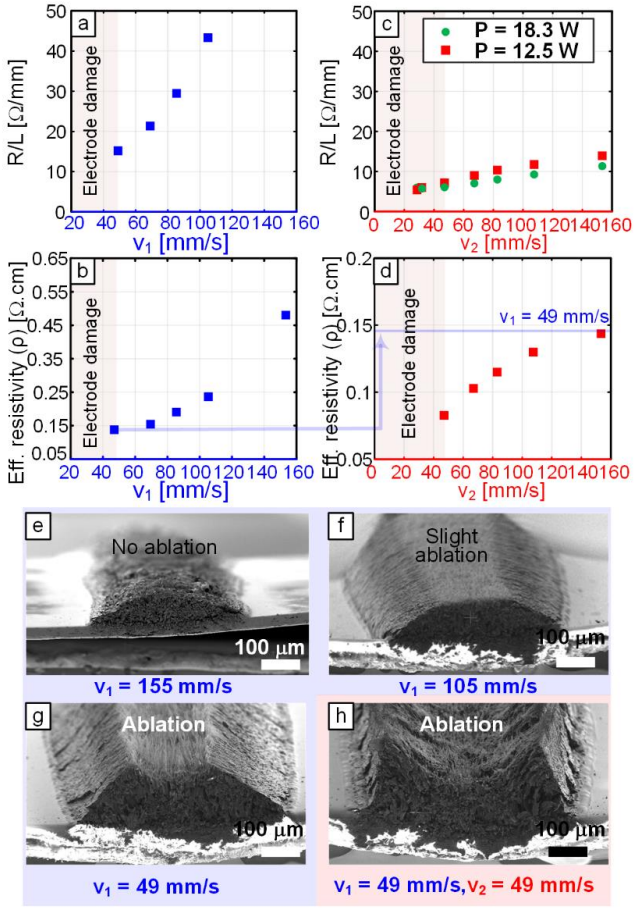

Figure 40: (a) Plot illustrating the influence of lasing speed on resistance per length values for LINC electrodes at P = 12.5 W, z = 9 mm. The onset of electrode damage at low speeds is illustrated. (b) Plot of corresponding effective resistivity of LINC electrodes in (a). (c) Plot illustrating the influence of relasing speed on resistance per length values for LINC electrodes at P = 12.5 W, z = 9 mm, v_1 = 49 mm/s and P = 18.3 W, z = 9 mm, v_1 = 49 mm/s. (d) Plot of corresponding effective resistivity of LINC electrodes in (c). (e,f,g) SEM images illustrating the cross sections of LINC electrodes at P = 12.5 W, z = 9 mm and different lasing speeds. (h) SEM image illustrating the cross sections of LINC electrodes at P = 12.5 W, z = 9 mm and v_1 = 49 mm/s and v_2 = 49 mm/s.

Through measuring the cross sectional areas of the electrodes using SEM imaging, the effective resistivity of the electrodes can be estimated. While it is not equivalent to the bulk resistivity of LINC due to its porosity, this measure can potentially give a strong indication of the change in bulk porosity and is a practical measure of electrode resistivity. The corresponding effective resistivity values to Figure 40 (a) are shown in Figure 40 (b) and show a similar trend in electrical resistivity decrease but with slower rate of decrease at lower v_1. The value of the effective resistivity ranges between 0.47 Ω.cm at v_1 = 155 mm/s and 0.14 Ω.cm at v_1 = 49 mm/s beyond which the electrodes are excessively damaged. To investigate the effect of relasing, the first lasing speed is fixed at v_1 = 49 mm/s while v_2 is changed between 155 mm/s and 29 mm/s. R/L values are shown for P = 12.5 W and P = 18.3 W with v_1 = 49 mm/s in Figure 40 (c). The corresponding effective resistivity values at P = 12.5 W are shown in Figure 40 (d). The R/L values range from 13 Ω/mm to 5 Ω/mm for v_2 values between 155 mm/s and 29 mm/s respectively with a decreasing trend. The corresponding effective resistivity values are noted to drop from around 0.14 Ω.cm to 0.08 Ω.cm. The relasing doesn't seem to affect the resistivity at v_2 = 155 mm/s but has a stronger decreasing effect as v_2 approaches v_1. However, as v_2 is decreased below v_1, excessive damage is noted in the electrodes. Overall, this shows that relasing is an effective technique to reducing the resistivity of LINC electrodes beyond the limits of single pass lasing. The effective resistivity also demonstrates a strong speed dependence which we will further investigate through other characterization techniques later. SEM imaging of some LINC electrode cross sections is shown in Figure 40 (e-h) to demonstrate the effect of lasing and relasing speed on cross section shape and show the extent of top surface ablation. Figure 40 (e) and Figure 40 (f) demonstrates the transition from wrinkled and porous surface morphology with a small cross sectional area to a more dome shaped cross section with some indications of ablation on the top of the dome when v_1 decreases

from 155 mm/s to 105 mm/s. Figure 40 (g) shows the influence of further decreasing the v_1 to 49 mm/s: the ablation of the top dome of the electrodes, revealing some of the internal cells of the material. Figure 40 (h) clearly show the effect of relasing on the cross section, with even more amounts of top surface ablation creating a U shaped upper surface and exposing even more of the internal morphology of the LINC electrode.

5.4 Influence of Relase Speed on Electrode Graphitic Crystallinity and Surface Chemistry

To understand the driving factors behind the decrease in the electrical conductivity of LINC electrodes and its speed dependence and whether the relasing affects the crystallinity and surface chemistry of the material, we use Raman spectroscopy and X-ray photoelectron spectroscopy (XPS). Additionally, to understand the changes in the inner LINC morphology, X-ray diffraction and Transmission Electron microscopy are performed on scrapped off LINC material.

Initially, the Raman spectra of lines generated using different lasing speed v_1 are analyzed. The influence of relasing is then investigated by fixing v_1 at 49 mm/s and changing the v_2 between 155 mm/s to 28 mm/s at a fixed power P = 12.5 W and defocus level z = 9 mm. The results of the Raman analysis are shown Figure 41 (a, b, c, d) and Figure 42. The Raman spectra for the lasing study is shown in Figure 41 (c) and the Raman spectra for the relasing study is shown in Figure 41 (d). The I(D)/I(G) ratio for both studies is shown in Figure 41(a) and Figure 41 (b). The I(D)/I(G) ratio is a metric that is generally highly correlated with the sp_2 carbon graphitic crystallite size, with a decreasing ratio correlated to increasing crystallite size according to the Tuinstra-Koenig correlation and is also correlated with defect levels in the material.[99] In both studies, the

I(D)/I(G) is noted to decrease with decreased speed. At a line lased at a speed of v_1 =105mm/s the I(D)/I(G) ratio average to 0.65 which drops to 0.44 at v_1= 105 mm/s as noted in Figure 41 (a, c).

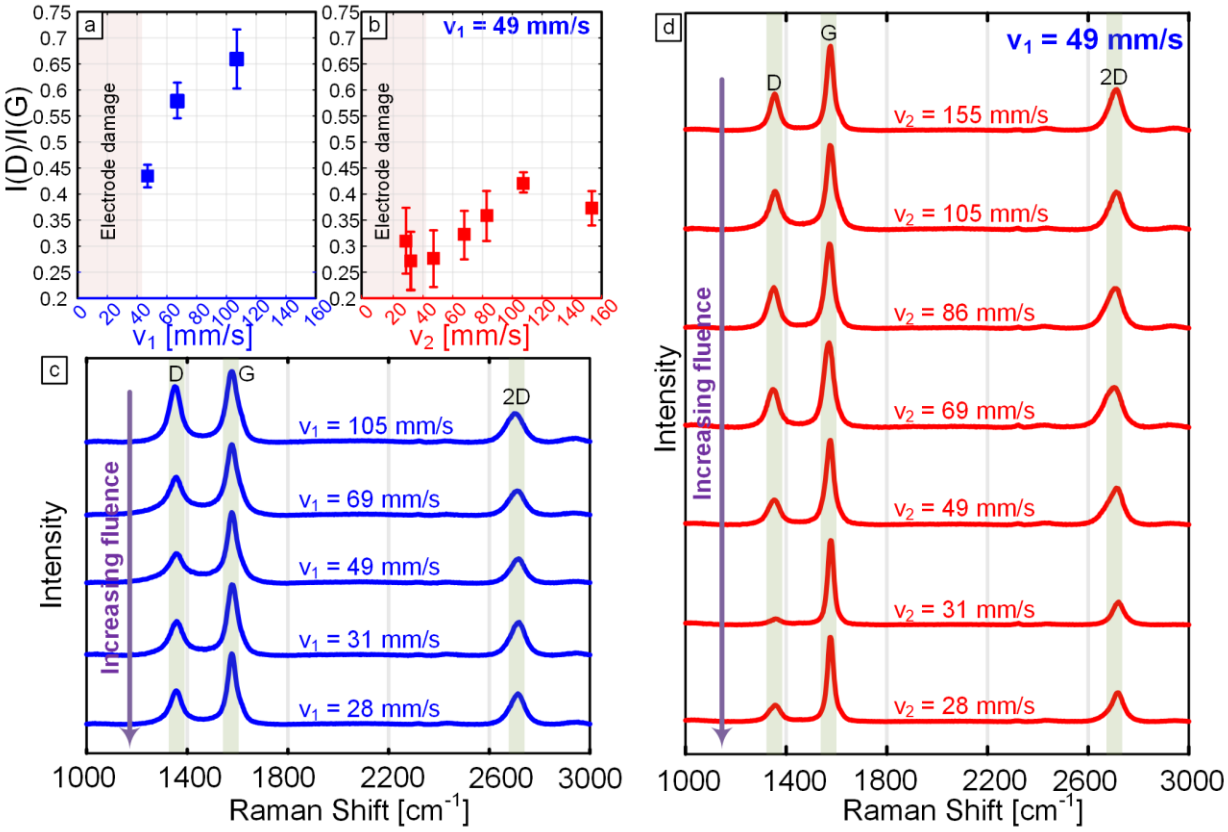

Figure 41: (a) Plot illustrating the influence of lasing speed on the I(D) to I(G) ratio for LINC lines at lased at P = 12.5 W, z = 9 mm with each point representing the mean of 5 measurements and error bars representing sample standard error. (b) Plot illustrating the influence of lasing speed on the I(D) to I(G) ratio at P = 12.5 W, z = 9 mm and v_1 = 49 mm/s with each point representing the mean of 5 measurements and error bars representing sample standard error. (c) Representative Raman spectra illustrating the effects of lasing speed at P = 12.5 W, z = 9 mm. (d) Representative Raman spectra illustrating the effects of relasing speed at P = 12.5 W, z = 9 mm and v_1 = 49 mm/s.

The relasing demonstrates that the value can be reduced further to an average ratio of around 0.26 (which can be as low as 0.1) at a relasing speed of v_2 = 31 mm/s as shown in Figure 41(b, d). Furthermore, it is noticed that the I(2D)/I(G) ratio decreases with decreasing speed as shown in Figure 42. The I(2D)/I(G) ratio is typically associated with graphitic layer stacking. These results highly suggest that the observed speed dependence of the resistivity might be correlated to increased graphitization of the graphitic domains of the material, which is driven by the increased dwell time of the laser beam when speeds are decreased.

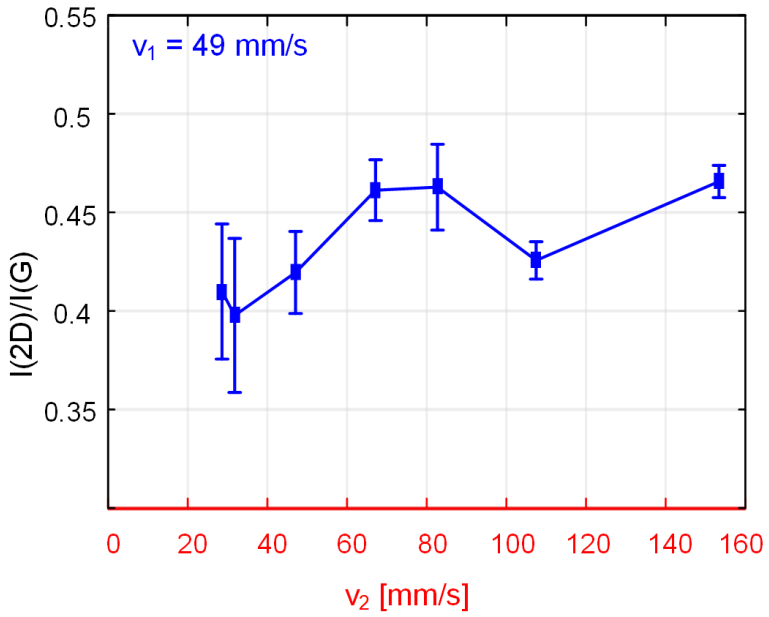

Figure 42: Plot of I(2D)/I(G) of LINC lines lased using conditions P = 12.5W, z = 9 mm, v_1 = 49 mm/s.

These conclusions are also supported by XRD analysis. XRD profiles of scrapped LINC lines lased at v_1 = 105 mm/s, v_1 = 49 mm/s .and lines lased v_1 = 49 mm/s and relased at v_2 = 105 mm/s and v_2 =49 mm/s are shown in Figure 43 (a). Using the XRD profiles, the graphitic crystallite size along the thickness as well as the interlayer spacing and number of layers are analyzed and derived. The analysis is presented in Figure 43 (b, c), Figure 44 and Figure 45. The analysis is

performed by the deconvolution of the (002) peaks into Lorentzian peaks and using the main peak locations and peak FWHM to derive the crystallite parameters as illustrated in Figure 44 and Table 4. The peak shapes are presented in Figure 43 (b, c) and Figure 45. The (002) peaks are generally observed to be asymmetric at the lowest lasing speed (v_1 = 105 mm/s) where the data is noted to have high noise to signal ratio and a weak (100) peak.

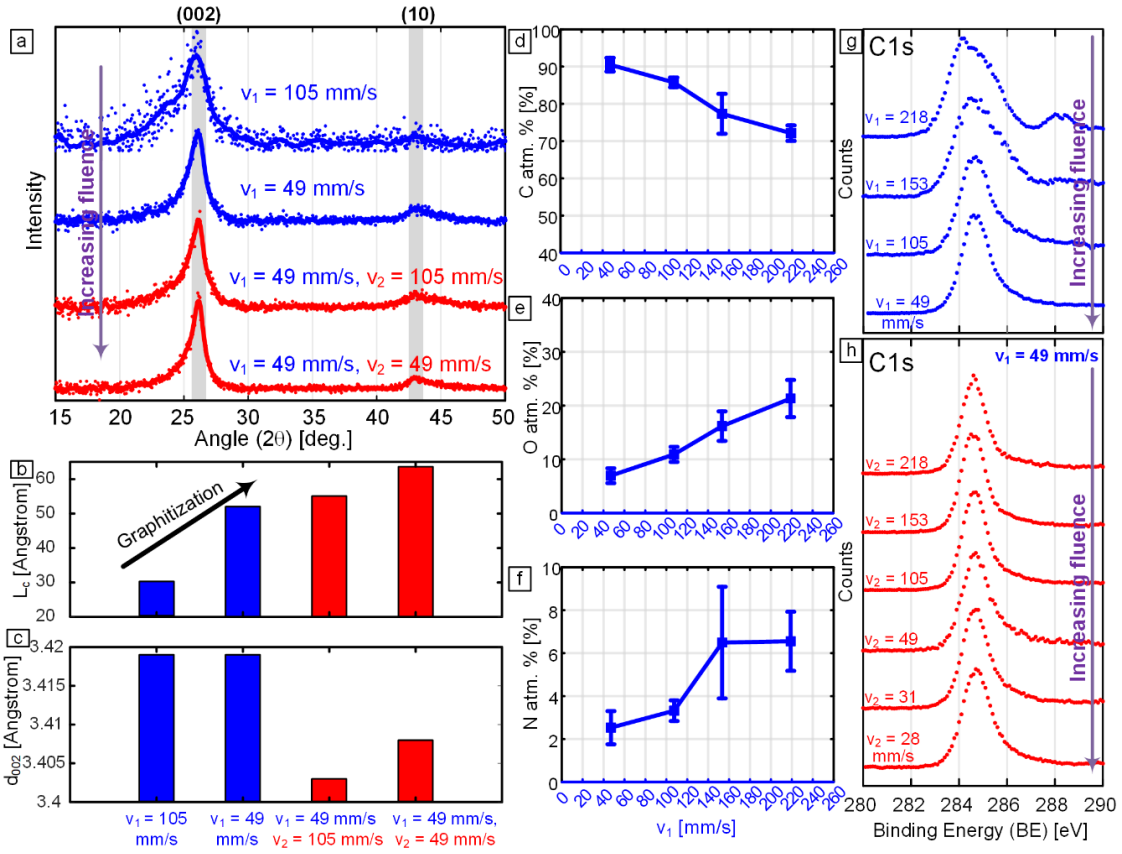

Figure 43: (a) XRD profiles of scrapped LINC lines at P = 12.5 W and z = 9 mm at different lasing and relasing conditions. (b) Bar chart illustrating the effect of lasing and relasing condition on L_c. (c) Bar chart illustrating the effect of lasing and relasing condition on d_{002}. (d) Plot showing the change in percentage atomic content of carbon derived from XPS survey spectrum of the surface of LINC lines at lased at P = 12.5W and z = 9 mm. (e) Plot showing the change in percentage atomic content of oxygen derived from XPS survey spectrum at different lasing speeds. (f) Plot showing the change in percentage atomic content of nitrogen derived from XPS survey spectrum at different lasing speeds. (g) Plots showing C1s core scans spectra at different speeds. (h) Plots showing C1s core scans spectra at different relasing speeds at P = 12.5W, z = 9 mm and v_1 = 49 mm/s.

With decreasing speed and relasing the asymmetry is noted to decrease, with improved signal-to-noise ratio. The analysis shows that lines lased at v_1 = 105 mm/s have an average L_c size of around 3 nm with an interlayer distance d_{002} of 3.418 Å and 9 graphitic layers. This changes to an average L_c = 5 nm with d_{002} = 3.418 Å and 15 layers when the lasing speed is reduced to v_1 = 49 mm/s. Line lased at v_1 = 49 mm/s and relased at v_2 = 105 mm/s show some change in the parameters with L_c = 5.5 nm with d_{002} = 3.402 Å and 16 layers. At an even lower relase speed v_2 = 49 mm/s, more significant changes are noted as the average L_c = 6.5 nm with d_{002} = 3.407 Å and 19 layers.

The results indicate clearly that relasing definitely drives more graphitization in the LINC lines. The results and analysis of the XPS analysis of LINC surfaces is shown in Figure 43 (d, e, f, g, h), Figure 46 and Figure 47.

The elemental composition of the surface for the lasing study for carbon, oxygen and nitrogen derived from XPS survey scans is shown under different lasing speeds v_1 is shown in Figure 43 (d, e, f). Expectedly, with decreasing lasing speed the heteroatom content is noted to decrease. At v_1 = 218 mm/s the % atomic percentage of carbon is around 73% which increases to a value of 92% at a speed of 49 mm/s. The C1s core scans are presented in Figure 43 (g, h) showing the evolution of the shape of the C1s peaks with changing lasing and relasing speed.

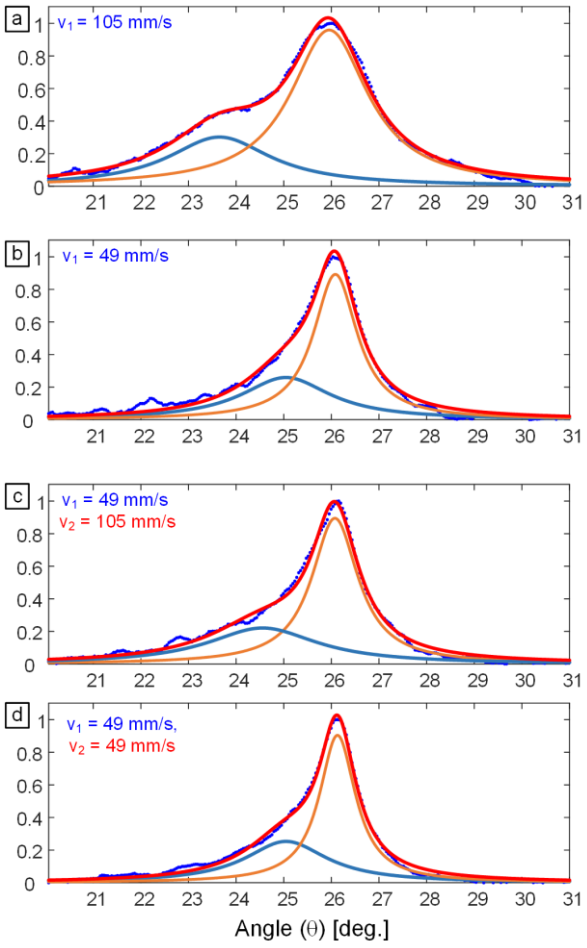

Figure 44: Plot of deconvolution of (002) peak in XRD profiles of LINC lines lased using conditions P = 12.5W, z = 9 mm and (a) v_1 = 105 mm/s, (b) v_1 = 49 mm/s, (c) v_1 = 49 mm/s, v_2 =105 mm/s and (d) v_1 = 105 mm/s and v_2 =49 mm/s.

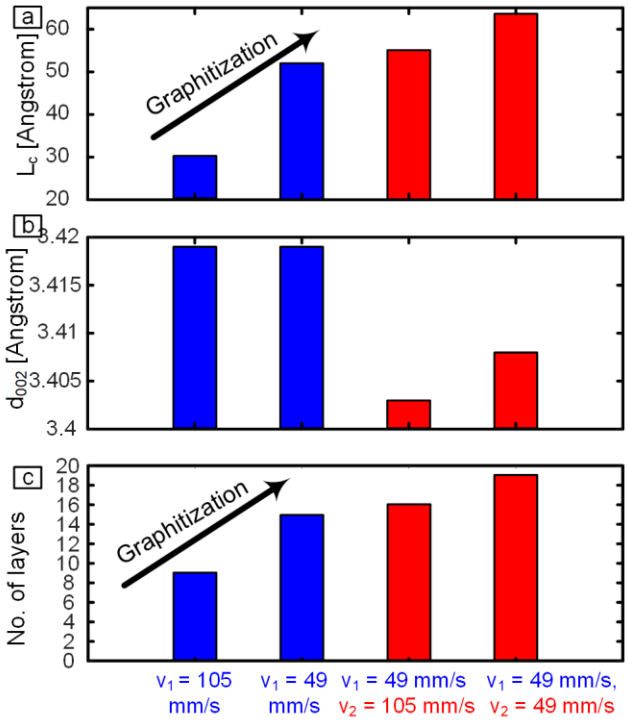

Figure 45: Bar plots demonstrating the change in the (a) crystallite size, (b) spacing and (c) no. of layers of graphitic domain of different LINC lines generated at different laser conditions with P = 12.5W and z = 9 mm.

Table 4: Summary of XRD deconvolution and derived crystallite parameters.

v_1 [mm/s]	105	49	49	49
v_2 [mm/s]			105	49
2θ [deg.]	26.034	26.034	26.154	26.114
FWHM [deg.]	2.653	1.550	1.463	1.266
L_c [Å]	30.381	51.993	55.103	63.682
d_{002} [Å]	3.419	3.419	3.403	3.408

The deconvolution of C1s peaks into its different components is presented in Figure 47 and Table 5. The results show that with relasing the sp_2 C1s peak is the dominant species of carbon without significant change in shape of C1s and heteroatom content with decreased relasing speed.

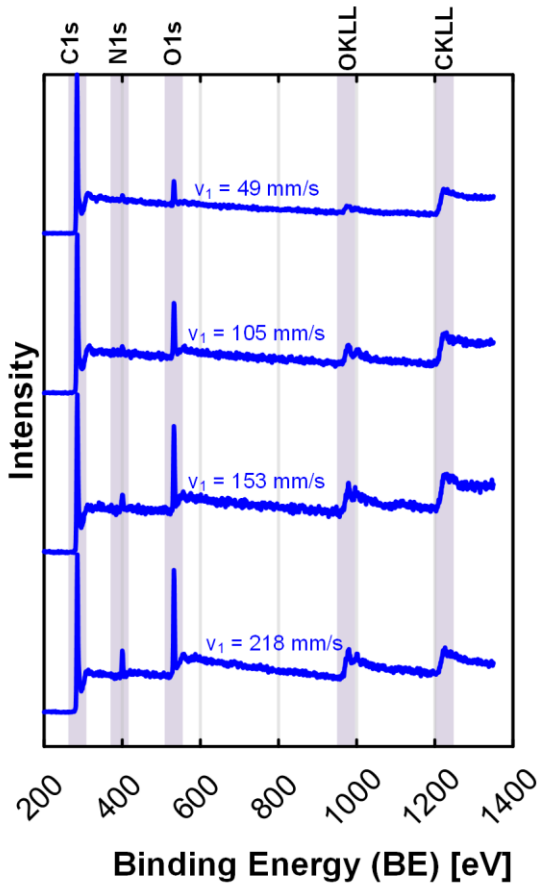

Figure 46: XPS survey scans of LINC lines created using laser condition P = 12.5W, z = 9 mm and different lasing speeds v_1.

To get more insight on the molecular structure of LINC, TEM imaging of LINC flakes is conducted to confirm if there is any noticeable difference in the size of the graphitic domains in the material as shown in Figure 48(a, b, c, d). TEM images in Figure 48 (a, b) shows that LINC lased at v_1 = 105 mm/s show small graphitic domains around L_c = 3 nm that are highly disordered with respect to each other with large pores between them as well. Figure 48 (c, d) demonstrates the effect of relasing with larger and more ordered graphitic domains with L_c up to 9.3 nm in size and more stacked graphene layers. These results support the observations from Raman and XRD analysis.

Table 5: Summary of C1s peak deconvolution

v_1 = 218 mm/s			
Peak Name	Position (eV)	Area	FWHM (eV)
C-H (ODA)	283.8	0.75	1.2
C-H (PMDA)	284.2	0.304	1
C=C sp2	284.7	0.246	0.8
C-N	285.1	0.441	1.56
C-O	285.55	0.528	1.36
C=O	288.17	0.311	1.42
Pi-Pi*	290.5	0.285	2.95
v1 = 153 mm/s			
Peak Name	Position (eV)	Area	FWHM (eV)
C-H (ODA)	283.972	0.829	1.506
C=C sp2	284.7	0.987	1.531
C-N	285.815	0.278	1.2
C-O	286.051	0.297	2.113
C=O	288.434	0.422	2.55
Pi-Pi*	291.124	0.259	2.554
v1 = 105 mm/s			
Peak Name	Position (eV)	Area	FWHM (eV)
C-H (ODA)	283.88	0.159	1.346
C=C sp2	284.7	1.05	1.191
C-N	285.4	0.1	0.995
C-O	285.9	0.615	1.992
C=O	287.88	0.287	2.2
Pi-Pi*	290.65	0.33	2.95
v1 = 49 mm/s			
Peak Name	Position (eV)	Area	FWHM (eV)
C-H (ODA)	283.88	0.132	1.342
C=C sp2	284.7	1.057	1.148
C-N	285.401	0.1	1.074
C-O	285.901	0.454	2.059
C-O-C	288.524	0.292	3.042
Pi-Pi*	291.233	0.166	2.132
v1 = 49 mm/s, v2 = 218 mm/s			
Peak Name	Position (eV)	Area	FWHM (eV)
C=C sp2	284.7	1.114	1.252
C-N	285.4	0.1	2.029
C-O	285.9	0.218	2.166
C-O-C	287.798	0.218	2.778
Pi-Pi*	290.641	0.181	2.373

v_1 = 49 mm/s, v_2 = 153 mm/s			
Peak Name	Position (eV)	Area	FWHM (eV)
C=C sp2	284.7	1.101	1.178
C-N	285.4	0.166	2.069
C-O	285.9	0.255	2.213
C-O-C	287.925	0.18	2.514
Pi-Pi*	291.06	0.295	3.162
v1 = 49 mm/s, v2 = 105 mm/s			
Peak Name	Position (eV)	Area	FWHM (eV)
C=C sp2	284.7	1.103	1.187
C-N	285.4	0.141	2.01
C-O	285.9	0.275	2.152
C-O-C	288.048	0.201	2.73
Pi-Pi*	291.2	0.286	3.134
v1 = 49 mm/s, v2 = 49 mm/s			
Peak Name	Position (eV)	Area	FWHM (eV)
C=C sp2	284.7	1.154	1.325
C-N	285.4	0.1	2.076
C-O	285.9	0.445	2.215
C-O-C	288.341	0.217	2.398
Pi-Pi*	290.985	0.197	2.6
v1 = 49 mm/s, v2 = 31 mm/s			
Peak Name	Position (eV)	Area	FWHM (eV)
C=C sp2	284.7	1.123	1.257
C-N	285.4	0.193	2.184
C-O	285.9	0.317	2.346
C-O-C	288.816	0.211	3.361
Pi-Pi*	291.723	0.1	2.687
v1 = 49 mm/s, v2 = 29 mm/s			
Peak Name	Position (eV)	Area	FWHM (eV)
C=C sp2	284.7	1.298	1.382
C-N	285.4	0.131	2.038
C-O	285.9	0.166	1.886
C-O-C	287.179	0.153	2.616
Pi-Pi*	290.551	0.123	2.649

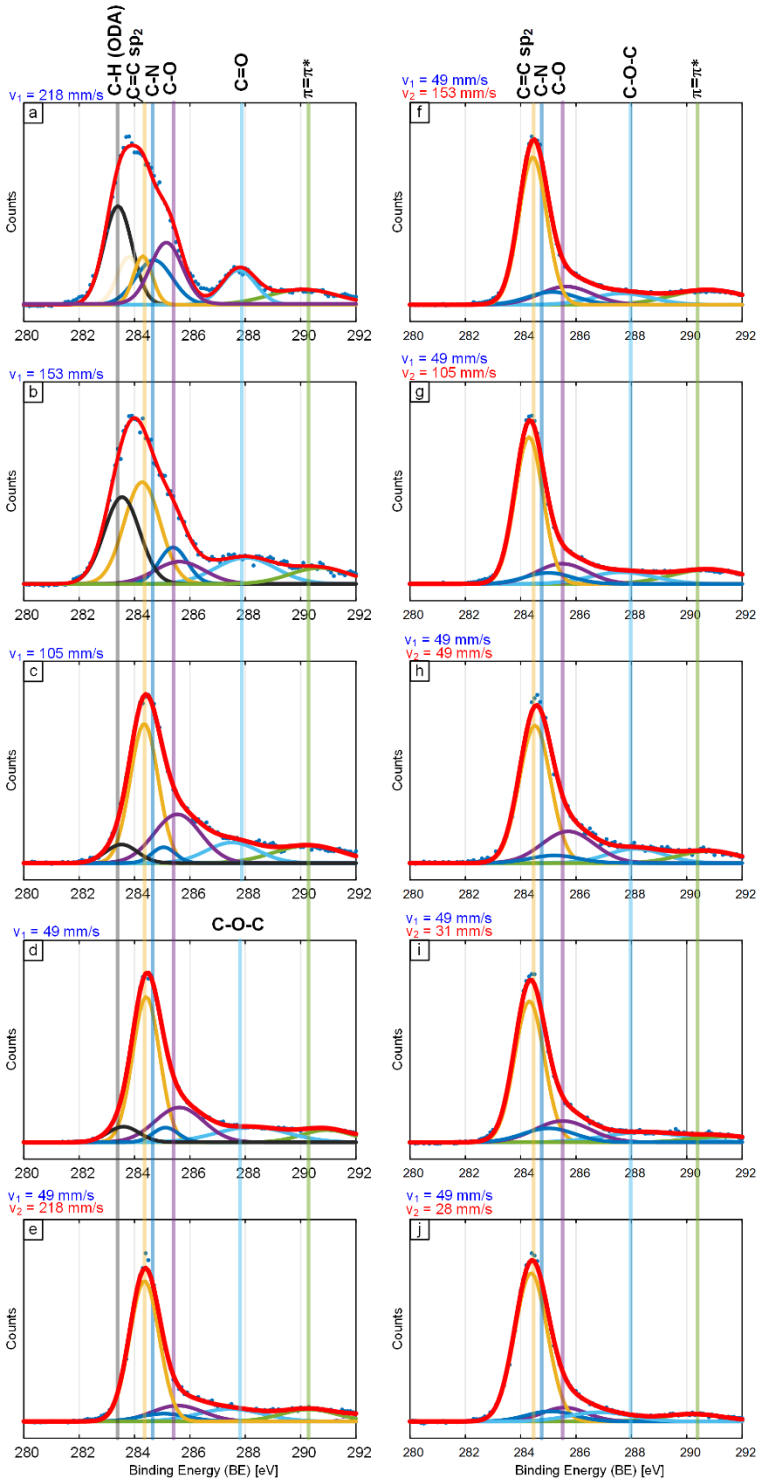

Figure 47: C1s core scans of LINC lines lased using laser conditions P = 12.5 W and different lasing and relasing conditions

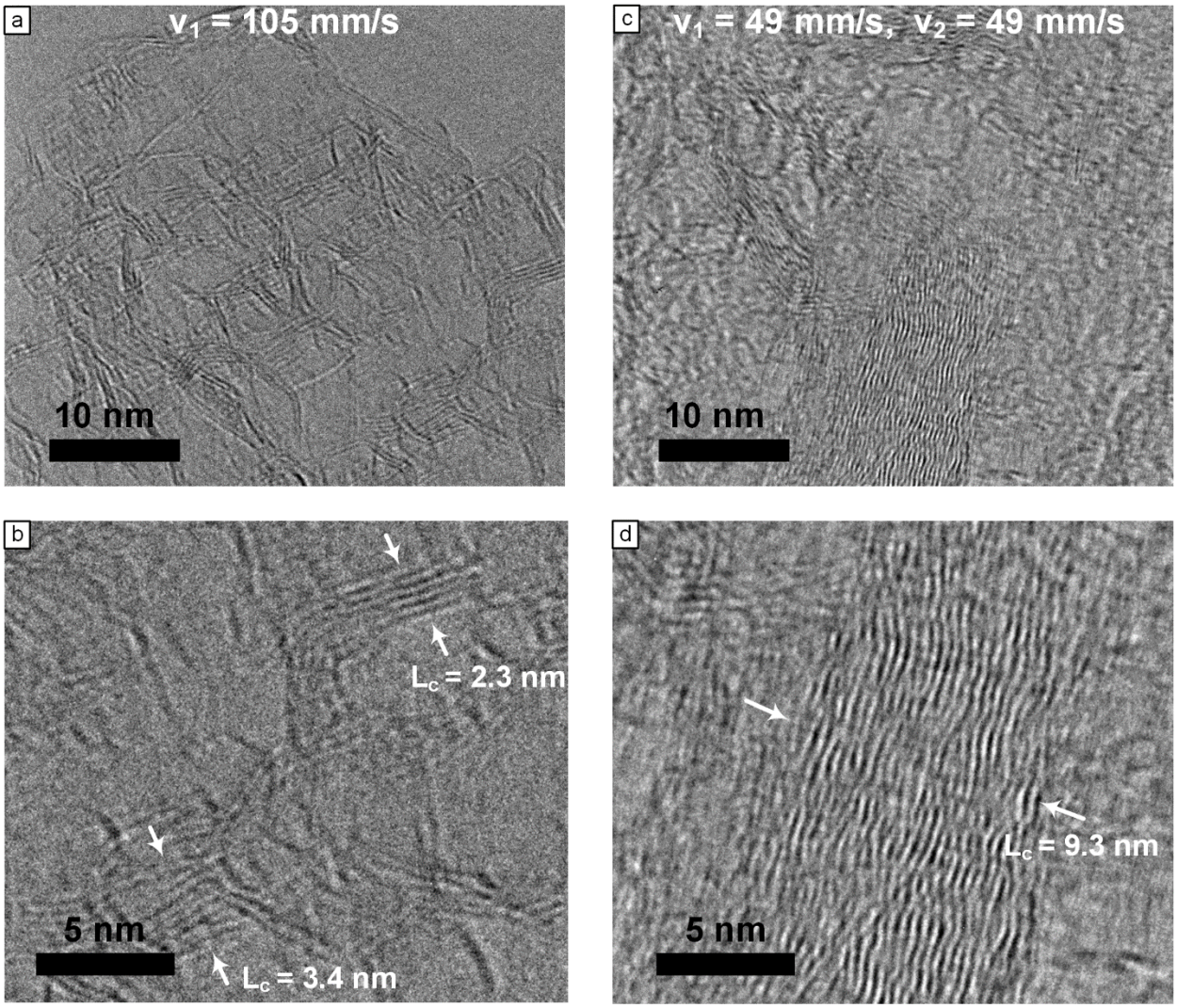

Figure 48: (a) TEM image of LINC at P = 12.5W, z = 9 mm and v1 = 105 mm/s lasing conditions. (b) HRTEM image showing different Lc sizes at .v_1 = 105 mm/s condition (c) TEM image of LINC at P = 12.5W, z = 9 mm and v_1 = 105 mm/s and v_2 = 49 mm/s lasing conditions. (d) HRTEM image showing Lc size at .v_1 = 49 mm/s and v_2 = 49 mm/s condition.

5.5 Relased Electrodes as Sensing Neural Electrodes

To test the electrochemical capability of these electrodes and the influence of relasing on their performance, we fabricate a set of electrodes using three laser conditions using continuous CO_2 laser (λ=10.6 μm) on polyimide sheets (Dupont KHN, polyimide thickness: 127 microns), with P = 12.5 W, z= 9 mm: (a) v_1= 105 mm/s, (b) v_1 = 49 mm/s and (c) v_1 = 49 mm/s, v_2 = 49 mm/s with three replications created for each condition. After insulating the electrodes to control the working electrode area, SEM imaging is used to measure the electrode surface area. SEM imaging of the electrode areas are presented in Figure 49 and shows that the electrodes exhibit a diversity of surface morphologies. The first lasing condition results in electrodes having a dome shape with minimal effects of ablation on the top Figure 49 (a). The second lasing condition results in electrodes demonstrating some ablation on the top (Figure 49 (b)) while the final lasing condition features large levels of ablation on top of the electrode as shown in Figure 49 (c).

5.5.1 Packaging of Electrodes

After fabrication of the electrodes, nitrocellulose based transparent nail polish (7417045109) is applied as an insulation layer to define the working electrode area which is controlled to be a specific length $\approx$ 1.2 mm. The electrodes were externally connected with conductive flat jaw alligator clamps (McMaster Carr, 7236K27) which clamp onto silver paint (PELCO® Conductive Silver Paint, Ted Pella, Inc 16062) applied to the end of the electrode. The silver paste and alligator connection are also insulated with the nitrocellulose based insulation for full insulation. The packaging method is illustrated in Figure 50.

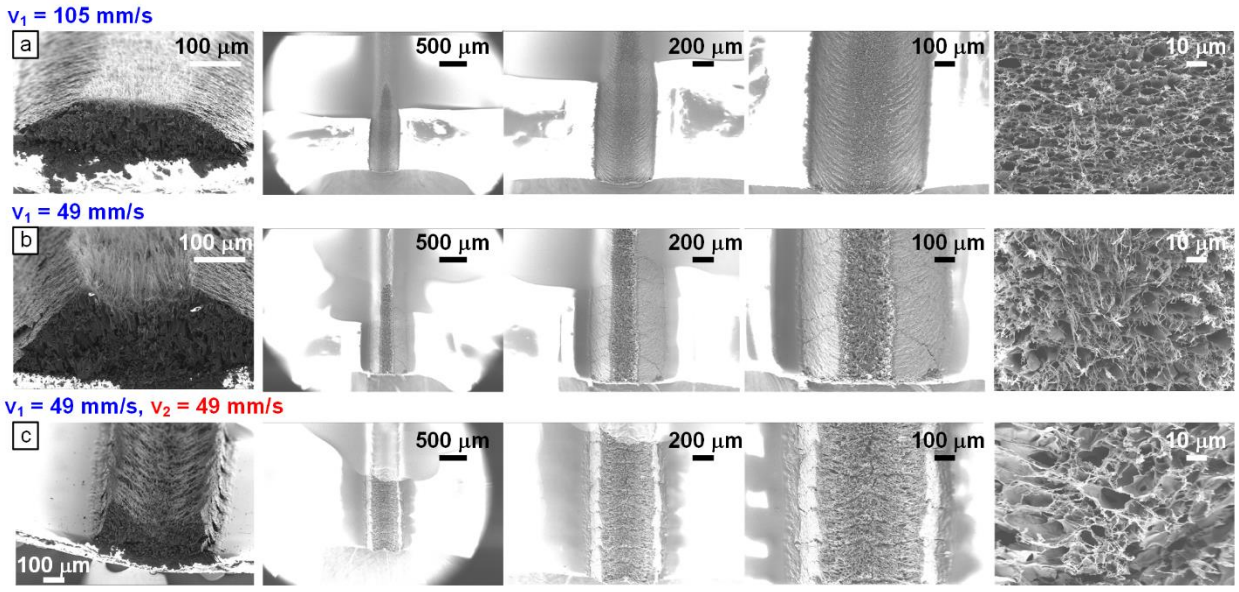

Figure 49: SEM images of LINC neural probes electrodes after packaging for different laser conditions P = 12.5W, z = 9 mm and (a) v_1 = 105 mm/s, (b) v_1 = 49 mm/s and (c) v_1 = 49 mm/s, v_2 = 49 mm/s. showing illustrating the insulation and the surface morphology.

5.5.2 Electrochemical Testing of the Electrodes

Two electrochemical testing methods were used to test the electrodes: Electrochemical Impedance Spectroscopy (EIS), to determine the electrical properties of the system over a large frequency range, and Cyclic Voltammetry (CV), to quantify the electrode capacitive charging, testing.

Electrochemical Impedance Spectroscopy (EIS) were performed in 1x phosphate buffered saline (PBS, composition: 11.9 mM Na2HPO4 and KH2PO4., 137 mM NaCl., 2.7 mM KCl, pH 7.4) applying a sine wave (10 mV RMS amplitude) onto the open circuit potential while varying the frequency from 1 to 105 Hz. EIS was carried out using a potentiostat/galvanostat (Autolab, Metrohm, USA) connected to a three-electrode electrochemical cell with a platinum counter electrode and an Ag/AgCl reference electrode. During the CV tests, the working electrode potential

was swept between 1.2 and −1 V (vs Ag/AgCl) with a scan rate of 100 mV/s. The charge storage capacity (CSC, mC/cm2) was calculated as CSC=(∫di dt)/(geometric area) in an entire CV cycle.

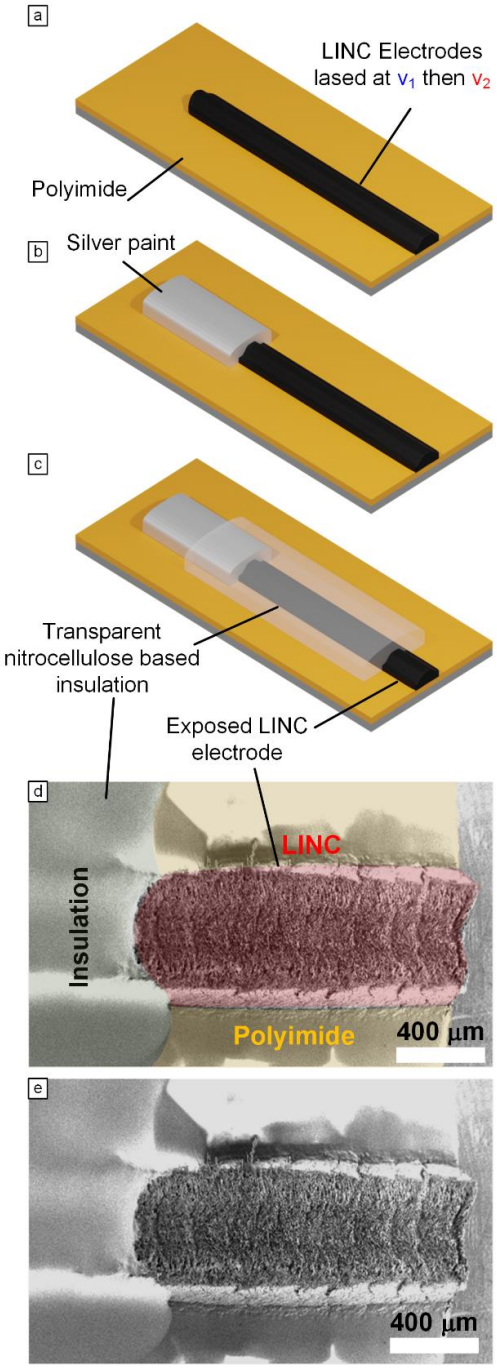

Figure 50: (a, b, c) Schematics illustrating the steps for fabrications and packaging of LINC electrodes for neural sensing applications. (d,e) SEM imaging showing the device packaging

The results, presented in Figure 51, Figure 52 and Figure 53 demonstrates that the LINC that the relasing influences the impedance and electrochemistry on the LINC electrodes, either due to the surface area enhancement to the material or due to the enhanced graphitization or a combination of both.

The relased LINC electrodes presented a lower impedance across the entire frequency range (1–10^5Hz). The normalized impedance magnitude values at 1 kHz, relevant physiological frequency for neural single unit activity, are reported in Table 6. The normalized electrochemical impedance (at 1 kHz) of the relased samples is 2-3 times lower than the LINC obtained with the other laser conditions.

The resistive contribution of the electrode-interface conductivity to the overall electrode impedance is estimated from the impedance measured at the high frequency, where the contribution to the impedance due to the charge transfer at the electrode-tissue interface is not significant. Over the 10^3–10^5 Hz frequency domain, the LINC exhibit a near-resistive phase (approaching 0°) and an impedance modulus that is almost entirely solution resistance. The normalized electrochemical impedance of the relased samples in this frequency range is 2-4 times lower than the LINC obtained with the other laser conditions (Table 6), revealing the higher conductivity of the relased LINC.

CV in the presence of 1x PBS presents an approximately rectangular current response in the -1/1.2 V vs Ag/AgCl potential window (Figure 52 (a)), suggesting predominantly double-layer capacitance governed response during the charging and discharging process [130,131]. Only for the relased microelectrodes, it is possible to observe a small faradaic oxidation peak at ca. 0.3V (Figure 52 (b)), similarly to what observed in high graphitized graphene electrodes.[132] It is worth noting that LINC microelectrodes show a wide water window, with no hydrolysis reactions

occurring between -1V and 1.2 V, making them optimal candidate for electrical micro-stimulation, where the electrodes are required to inject relatively large currents while minimizing electrode degradation due to faradaic effects.

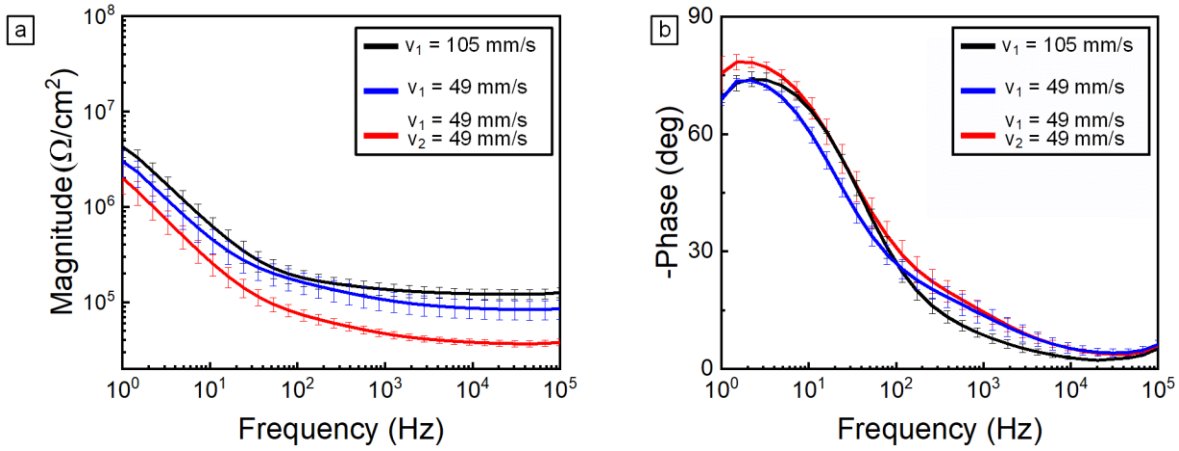

Figure 51: (a) Plot representing area normalized averaged EIS results for electrodes created using different laser conditions. (b) Plot representing area normalized averaged EIS results for electrodes created using different laser conditions.

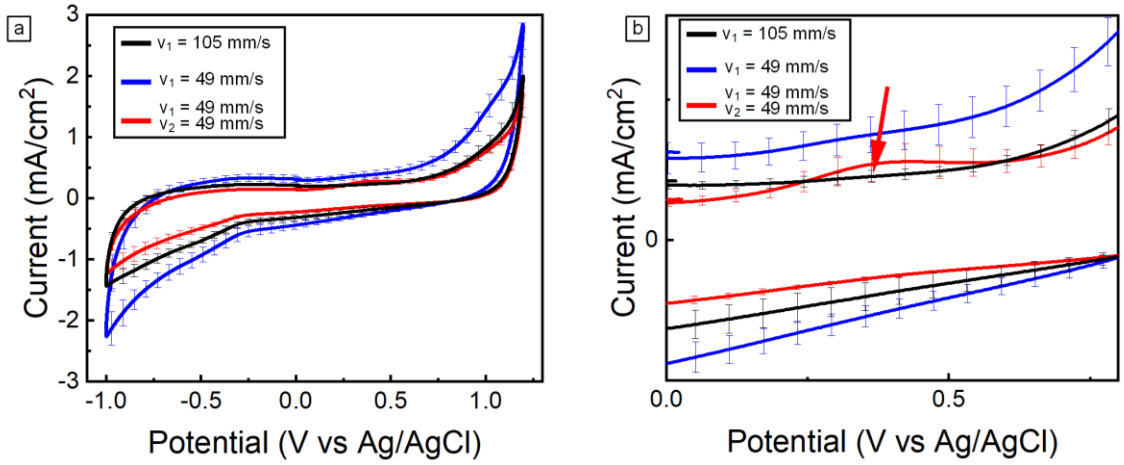

Figure 52: (a) Plot representing area normalized averaged CV results for electrodes created using different laser conditions. (b) Zoomed in CV plot illustrating the prominent peak associated with relasing.

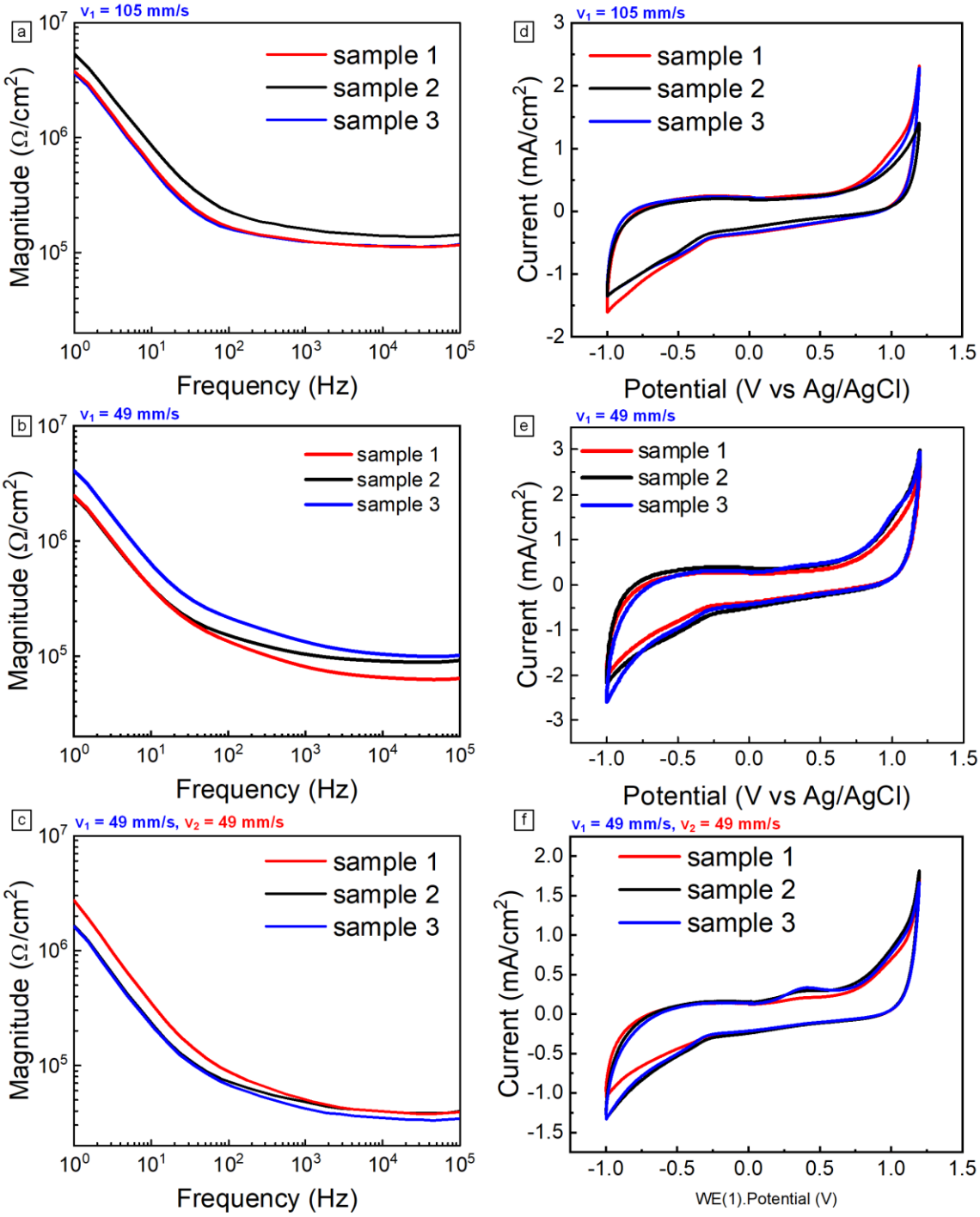

Figure 53: (a-c) Electrochemical impedance spectroscopy plots generated for individual LINC electrodes at different laser conditions. (d-f) CV plots generated using LINC electrodes at different laser conditions

The total charge storage capacity (CSC) values for the LINC obtained with the different laser conditions are reported in Table 6. The CSC were calculated as the time-integral of an entire CV cycle between -1 and 1.2 V.

High surface area carbon materials with controlled morphological structure have been shown to be promising candidates for neural electrode materials, at the purpose of, presenting excellent electrochemical performances and superior electrochemical stability [132,133]. The electrochemical results highlight the potential of the LINC electrodes to be miniaturized and used as superior materials for implantable devices for different neural applications, such as neurochemical sensing, electrical micro-stimulation and electrophysiological recording.

Table 6: Average area normalizaed impedance and CSV values for the electrodes

v_1 [mm/s]	v_2 [mm/s]	Impedance @ 1kHz	Impedance @ 100 kHz	CSV
105		102.14±24.90 kΩ/cm2	85.57±19.41 kΩ/cm2	2.68±0.29 mC/cm2
49		134.00±19.86 kΩ/cm2	125.88±14.44 kΩ/cm2	1.84±0.24 mC/cm2
49	49	45.10±3.95 kΩ/cm2	37.88±2.91 kΩ/cm2	1.46±0.14 mC/cm2

5.6 Conclusion

Using the relasing approach, we manage to enhance the conductivity of LINC materials without compromising the electrode mechanically. We explore the underlying physics behind this enhancement. This has revealed more into the fundamentals of LINC formation and more insight into the control of surface morphology. Additionally, we demonstrate the influence of relasing on the surface morphology and its electrochemical capability and demonstrated its potential for neural sensing.

6.0 Sequential Self-Folding of Shape Memory Polymer Sheets by Laser Rastering toward Origami-Based Manufacturing

In this chapter, we propose a scalable approach for controlled self-folding of shape memory polymers based on laser rastering. Localized heating is achieved by moving laser to deliver controlled energy across the rastering path. This is in contrast to prior work on using a stationary laser spot with a rectangular shape described earlier as illustrated in Figure 3. Our approach allows the accurate control of the spatiotemporal delivery of heat as a function of laser power, speed and number of passes along designed paths on the polymer, which enables control of fold angle and quality. Our results demonstrate that this approach can used to create complex three-dimensional shapes. Hence, it paves the way for developing unique manufacturing capabilities in creating functional parts that require complex 3D geometries and high surface quality.

6.1 Materials and Methods

6.1.1 Shape Memory Polymer

Commercially available sheets of pre-strained polystyrene sheets are used in this study (Grafix® Black Shrink Film, thickness 0.3 mm, bi-axially contract 55% approximately when heated above the glass transition temperature (T_g = 103°C) were used in this study. These sheets are known to have shape memory properties. This is achieved by heating the polymer above its glass transition temperature (T_g), stretching, and then cooling below T_g to preserve its shape. When the material is heated above the T_g, the preserved stresses are released. These sheets were used in

previous work for studying self-folding using different stimuli, and their properties are described in detail in other work. [19,23,27,29,134]

The sheets were cut down to sample sizes of 10 × 20 mm using a ruler and scissors. A protractor and ruler were used to measure the bending angle of the sheets after subjecting them to laser heating. Masking tape and Kapton tape were used to secure the samples to the laser platform, as shown in Figure 54 (a, b).

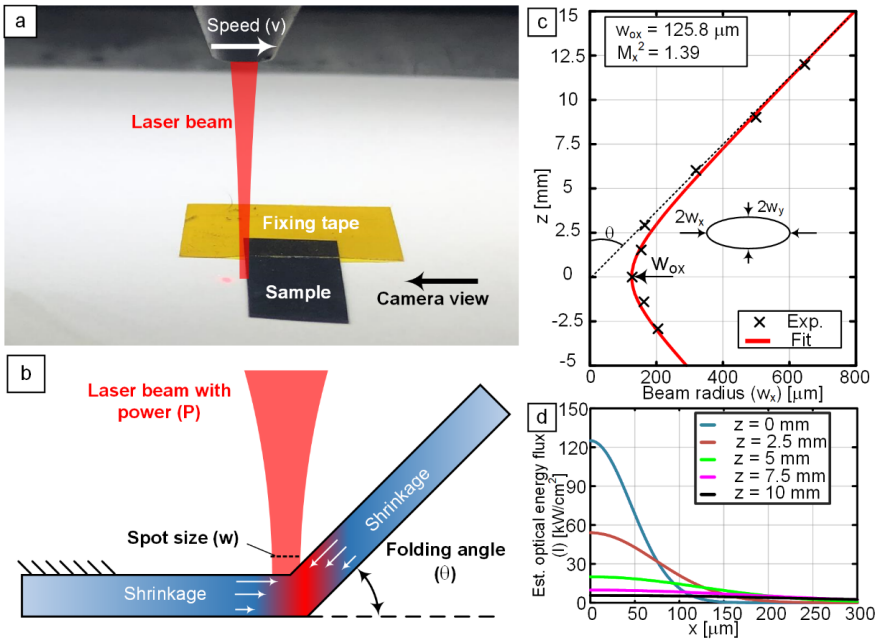

Figure 54: (a) Photograph of the laser processing setup, showing the laser objective lens and the sample with annotation for lasing direction, laser beam, and camera view for videography results shown in this work. (b) Schematic of the folding process showing the gradient of shrinkages, which results from the viscoelastic relaxation across the thickness of the pre-strained sheet having a gradient of temperature. (c) Experimental points representing the estimated laser beam profile along the lasing direction x using the knife edge technique, along with the profile of the fitted Gaussian beam illustrating the divergence of the beam away from the beam waist. The resulting beam spot in the x direction is estimated to be 2wox = 251.6 µm. (d) Estimated optical flux along the x direction at constant power (P = 22.5 W), showing the change of beam intensity with z (i.e. with changing spot size by defocusing the beam).

6.1.2 Laser System

The laser used is a continuous wave (CW) CO_2 laser system (Full Spectrum Laser Pro-Series 20 × 12, 1.5-inch focus lens) with 10.6 μm wavelength and 35 W power from the laser. The black polystyrene used in this study is highly absorbing to 10.6 μm laser light. The laser power can be adjusted by changing the laser current through pulse width modulation. We measure the laser power at different currents using a CO_2 laser power meter (HLP-200, Changchun Laser Optoelectronics Technology Co., Ltd.). The beam radius was measured based on ($1/e^2$) of the maximum intensity (w_y, w_x) at different distances (z) from the beam waist using the knife-edge method [64], where we assume single mode operation (TEM00) with a Gaussian beam profile. Using this technique, the beam radius at the beam waist (w_{ox}, w_{oy}), based on a Gaussian beam assumption, was determined to be 125.8 μm in the x-direction and 84 μm in the y-direction. The experimental beam radius in the x-direction and the estimated beam shape is shown in Figure 54 (c). Using the beam size and measured laser power, the flux at different defocus values is shown in Figure 54 (d).

Additionally, the laser is equipped with an air assist system, which is an air nozzle that is aligned with the laser beam that blows air onto the sample. The function of the air assist is to prevent overheating of the sample and to clear the lasing path from any debris or smoke.

A power (P) ranges of 0.14 - 28 W was used in our experiments in order to control the folding process. A speed (v) range of 108 - 508 mm/s and a fixed spot size (w) of 1 mm were used as well. Within this range of parameters, we were able to control how much energy and fluence were applied to the sample during folding.

The prepared samples were placed on an aluminum grating within the laser system as illustrated in Figure 54 (a, b). The samples were secured by using a piece of masking tape or

Kapton tape to hold the sample in place during the experiment. When the laser is subject to laser heating, the polymer strips would bend with an angle (θ), as illustrated in Figure 54 (b), that is measured with a protractor with respect to the sheets original position. To control the energy delivered for folding, we can control laser power (P), speed (v), number of lasing passes. Upon completing a forward path, the lasing head would decelerate, switch direction and conduct a return path till the number of passes is completed. Additionally, we test the influence of turning the air assist on or off, since the blown air would create some forces on the bending strips while lasing and also cool off the lased lines.

6.1.3 *In Situ* Videography and *Ex Situ* Imaging

Microscope cameras (Celestron Handheld Digital Microscope Pro) were used for imaging of the samples and videography during the lasing process. SEM images of the folds were completed on a Zeiss SIGMA VP Field emission scanning electron microscope. The samples were sputter coated with platinum and then imaged with a beam with an accelerating voltage of 2kV.

6.1.4 Multi-physics Simulation

To gain qualitative insight into the laser folding phenomenon, we develop a 3D FEM model of the laser driven folding. ANSYS APDL was used to run the model with SOLID227 elements, which can couple the thermal and mechanical fields and handle material non-linearity like viscoelasticity, hence can be used to model this problem.[135] We utilize the material parameters used in previous simulation efforts,[136,137] which use a generalized Maxwell model and the Williams–Landel–Ferry equation to account for viscoelastic effects and temperature dependence

as illustrated in Table 7 and Table 8. The polystyrene is modeled as an elastic-viscoelastic material The polystyrene sheet initial geometry has a length of 17 mm a width of 8.5 mm and a thickness of 0.4 mm. The problem is divided into two parts, the first being a thermal programming step to develop the pre-strain and the second being a local heating step to induce the folding as illustrated in Figure 55. In the thermal programming step, volumetric heating (Q_{gen}=0.25 W/mm^3, 0.45 s) is applied to the entire geometry, heating it up to a temperature higher than the PS glass transition temperature T_g. Convection boundary conditions are active at the sheet boundaries (h= 2.2e-5 W/mm² °C , T_∞=22 °C). After the heating is completed and the sheet temperature exceeds the T_g, a pressure P is applied to the upper sheet surface and ramped to a value of 25 MPa in 8 seconds, compressing the sheet, and then the load is held constant. The sheet dimensions after compression had a length of 22 mm a width of 11 mm and a thickness of 0.3 mm. While the pressure is held constant, negative volumetric heating (Q_{gen}= -0.15 W/mm^3, 0.45 s) is applied to cool the sheet to below the T_g, hence maintaining the pre-strained state. The model is then heated at the upper surface center by programming the surface flux boundary condition to reflect the laser heating with Power (P = 2.5W. 4.5W, 6.5 W, 8.5 W, 10.5 W), speed (v = 250 mm/s) and defocus level (z = 8 mm) with a Gaussian profile to drive the folding. We monitor the temperature, axial strain and folding angle across the center of the sheet during and after the heating process for the five power cases. Tetrahedral elements are used to mesh the geometry as shown in Figure 55 (c) with a total element number of 14000 elements. The element number is decided using a convergence study as illustrated in Figure 55 (d).

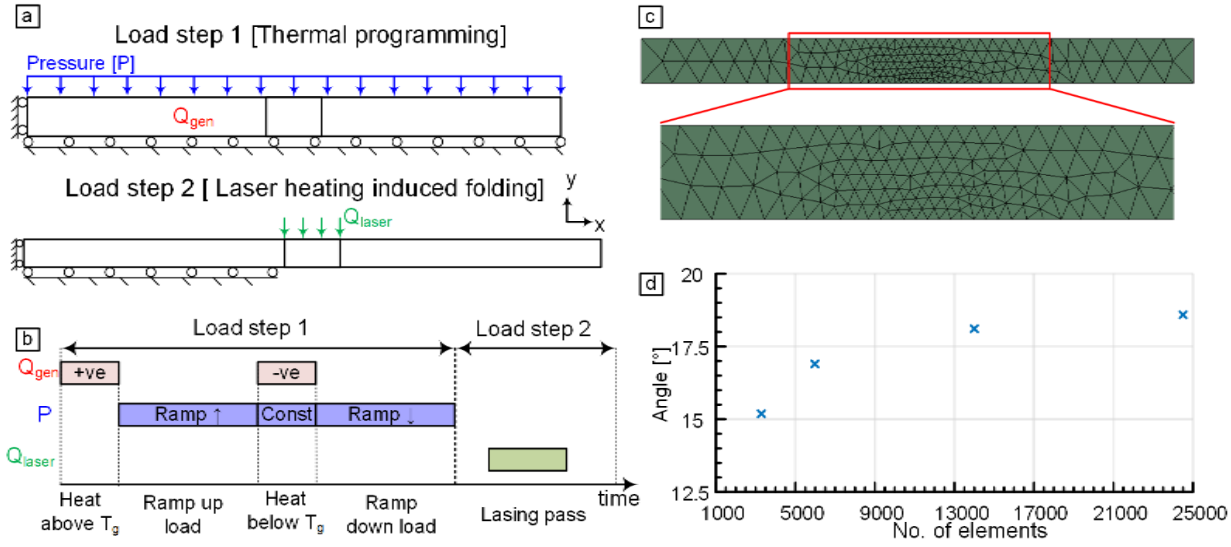

Figure 55: Boundary conditions for the folding simulations

Table 7: PS thermal and mechanical material propeties

PS WLF C1	17.44
PS WLF C2	51.6 K
PS Glass transition temp.	103 °C
PS Young's Modulus	1.78e9 Pa
PS Specific Heat	1300 J/kg K
PS Poisson's Ratio	0.33
PS Thermal Conductivity	0.14 W/m K
PS density	1050 Kg/m^3

Table 8: Prony coefficients for viscoelastic PS model

Branch #	1	2	3	4	5	6
g (i)	0.2089	0.3654	0.3037	0.1011	0.01243	0.004661
τ(i) (s)	1.182	14.77	114.8	402	3096	25680

6.2 Results and Discussion

6.2.1 Influence of Power and Speed with Air Assist On

In this experimental study, the influence of power and speed with the air assist on is tested. In the experiment, a power range (P = 0.1 - 9 W) with a speed range (v = 107 - 500 mm/s) were investigated at a fixed spot size ($2w_x$ = 1 mm) for 9 passes. Multiple passes are conducted in rapid succession, wherein the lasing head abruptly decelerates upon completing a forward path and switch direction to conduct a return path at the same speed (v). The stopping time is estimated to be small compared to the lasing time. The resulting folding angles are shown in Figure 56. Folding started at powers ranging from 1.4 W to 2 W, depending on the lasing speed. The results generally show a quick increase in folding angle between powers 1 – 2 W. With higher speed, it is noted that the transition occurs more slowly. In addition, in the lowest speed case (v = 107.5 mm/s), the folding increases and then drop at powers beyond 3 W, indicating that excessive deformation or cutting damage has occurred.

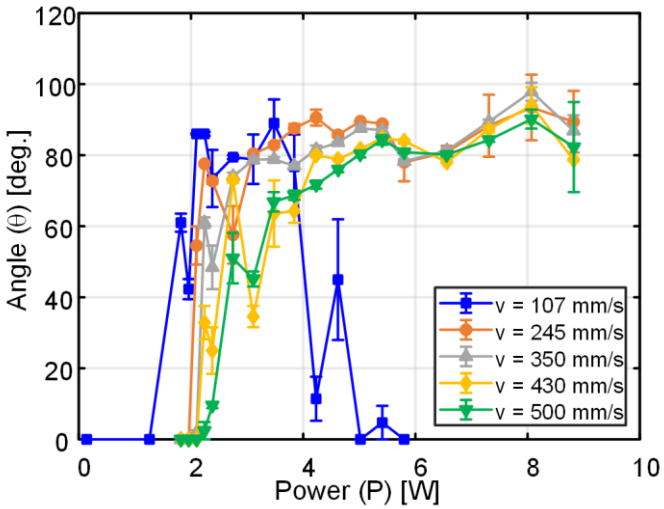

Figure 56: The resulting folding angles generated from different power and speed combinations for the laser with the air assist on. All samples were subject to 9 lasing passes. Error bars indicate standard error based on seven replications.

One advantage of using the air assist is that since the airflow has a cooling effect on the polymer samples, a larger power range can be explored, and a higher range of high-quality folds can be achieved. For example, when the samples are subject to excessive laser fluence, folding can occur, but it is accompanied by excessive deformation and distortion to the fold geometry locally at the hinge. These undesired effects might lead to issues of reduced repeatability and compromised structural integrity of the resulting 3D structures. A juxtaposition of different fold geometries is shown in Figure 57, illustrating that there is a wide range of shapes of folds that occur at the different combinations of power and speed.

Figure 57: Side view and top view images indicating the influence of laser conditions on fold distortion and quality , where too much heating leads to excessive deformation manifested as highly distorted hinges. (P = 3.5 W, v = 500 mm/s, 2wx = 1 mm, n = 9) and (P = 3.5 W, v = 107 mm/s, 2wx = 1 mm, n = 9) were imaged using SEM as well.

While some lasing conditions lead to large angle folding, some of the folds are too distorted. This is why characterizing the quality of the fold by optical imaging is an important complement to the measurement of fold angle. Importantly, it is noted that from our observation, we find that some conditions can achieve both large folding angles and minimal distortion to fold geometry, as shown in Figure 57.

In addition to optical imaging, we use scanning electron microscopy (SEM) to further investigate fold surface quality and local distortion. Our SEM images show the effect of over-

heating (at conditions of lower laser speed) on compromising fold quality as shown in Figure 58 (a,b). The local shrinkage and excessive material flow are visible.

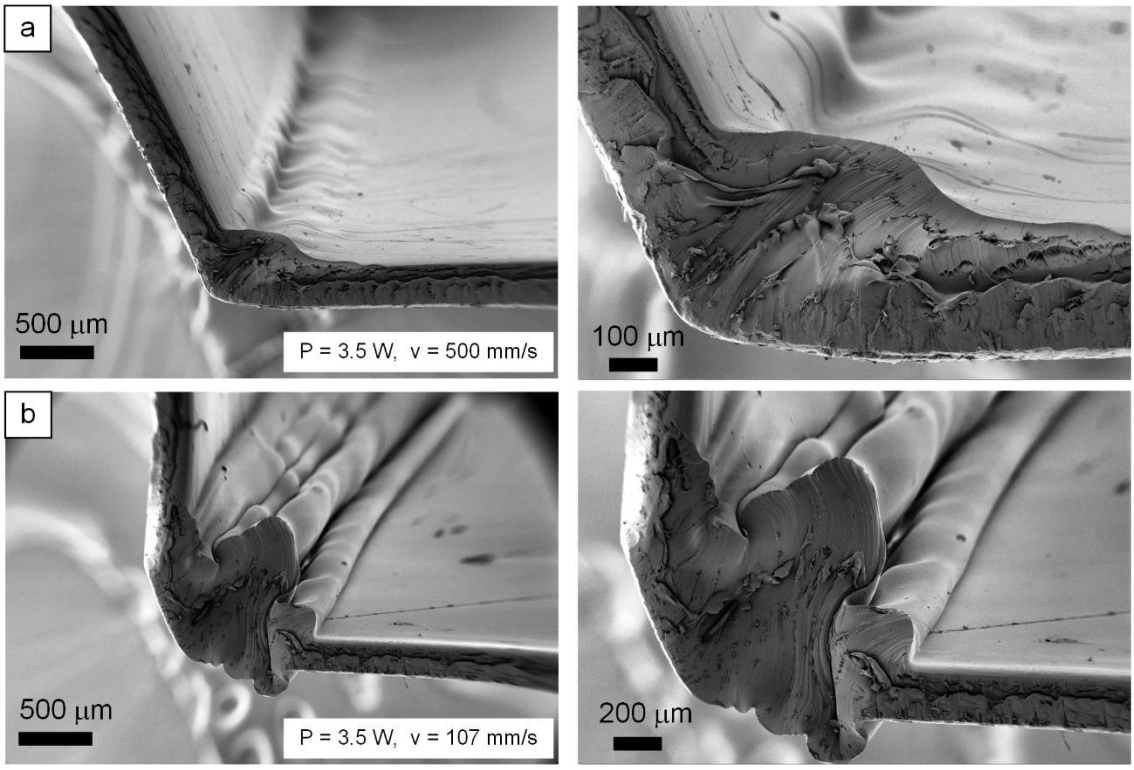

Figure 58: (a) SEM image of fold with minimal hinge distortion illustrating the folding and shrinkage pattern at the edge and at the fold (P = 3.5 W, v = 500 mm/s, $2w_x$ = 1 mm, n = 9) . (b) SEM image of fold with excessive fold distortion (P = 3.5 W, v = 107 mm/s, $2w_x$ = 1 mm, n = 9).

6.2.2 Influence of Power and Speed with Air Assist off

We also investigate the influence of power and speed in the absence of air assist, by varying laser power and speed while maintaining a constant spot size, with the air assist off. In this study, a power range (P= 0.1 - 5 W) is tested with a speeds ranging from 107.5 - 500 mm/s and a fixed spot size ($2w_x$ = 1 mm) for 9 passes. With the air assist off, the polymer samples were subject to higher fluence for a small power range, as compared to the air assist mode. Moreover, turning of the air flow also eliminated the resistance force pushing down on the sample.

Results shown in Figure 59, indicated that folding started at P = 0.1 W at the lowest speed (v = 107.5 mm/s), much lower than with the similar conditions with air assist on, demonstrating the effect of the lower air pressure and no air cooling on the folding.

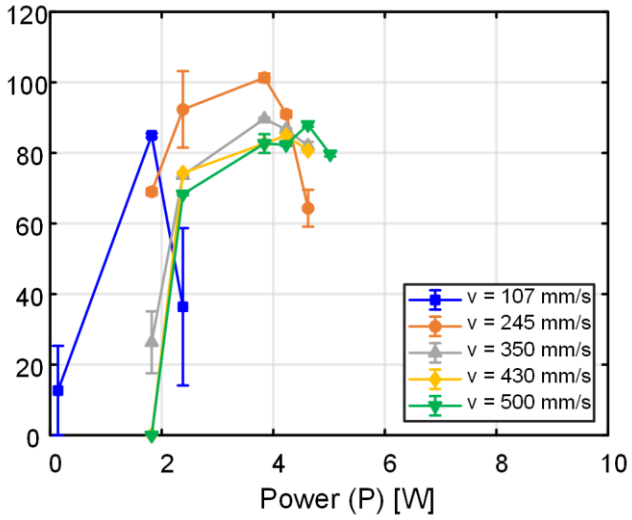

Figure 59: The resulting folding angles generated from different power and speed combinations for the laser with the air assist off. All samples were subject to 9 lasing passes. Error bars indicate standard error based on seven replications.

In the cases with lasing speeds v = 107.5 mm/s and 245.5 mm/s, folding angles are noted to drop beyond P = 1.5 W and 3.5 W respectively, indicating excessive heating that cause too much flow of material or melting of the polymer in some cases. At higher speeds, little change is noted between the folding angle at different speeds. In these cases, folding starts at 1.5 W lasing power, which transitions with increasing power till an average folding angle of 90° is reached at a power of 5 W.

6.2.3 Influence of Number of Lasing Passes

To explore the effect of the number of passes on the folding angle, the number of passes was varied between 1 to 10 passes at two levels of power (P = 2.4 W and P = 5.8 W) and a fixed speed (v = 350 mm/s), fixed spot size and air assist on.

Real-time monitoring of folding angle after each pass is achieved by employing in situ videography. Results where images of the folding are recorded with number of passes are shown in Figure 60. It is noteworthy that after one lasing pass there is little folding, but with subsequent folds, the folding angle increases incrementally until it reaches an average value of around 30° at these conditions (P = 3.5 W, v = 430 mm/s, $2w_x$ = 1 mm). This indicates that the cumulative effect of incrementally adding small energy doses can gradually increase the temperature at the hinge to activate the folding without excessively damaging the hinge. The quantitative results for folding angle dependence on number of passes are presented in Figure 61. For the low power case in Figure 61 (a), it is noted that no folding occurs for less than 5 lasing passes. This implies that the temperature was not high enough to trigger folding until after the 5^{th} pass. With increasing number of passes, the folding angle reached an average value of 8°. Eventually, the angle starts to drop after 9 passes. For the higher power, shown in Figure 61 (b), folding starts after 2 lasing passes. Also, the fold angle increases up to an average of 90° which drops after the 8^{th} pass. The nature of the process prevents lasing beyond 90° since the beam will be blocked by the folded side of the polystyrene sheet. The drop in angle is caused by excessive heating and material flow, as will be discussed later. As noticed from the optical and SEM imaging (Figure 57 and Figure 58), over-heating leads to melting and excessive hinge deformation, which are undesirable. In addition to excessive material flow, more passes lead to excessive relaxation across the whole sheet and hence lower strain gradients and smaller folding angles.

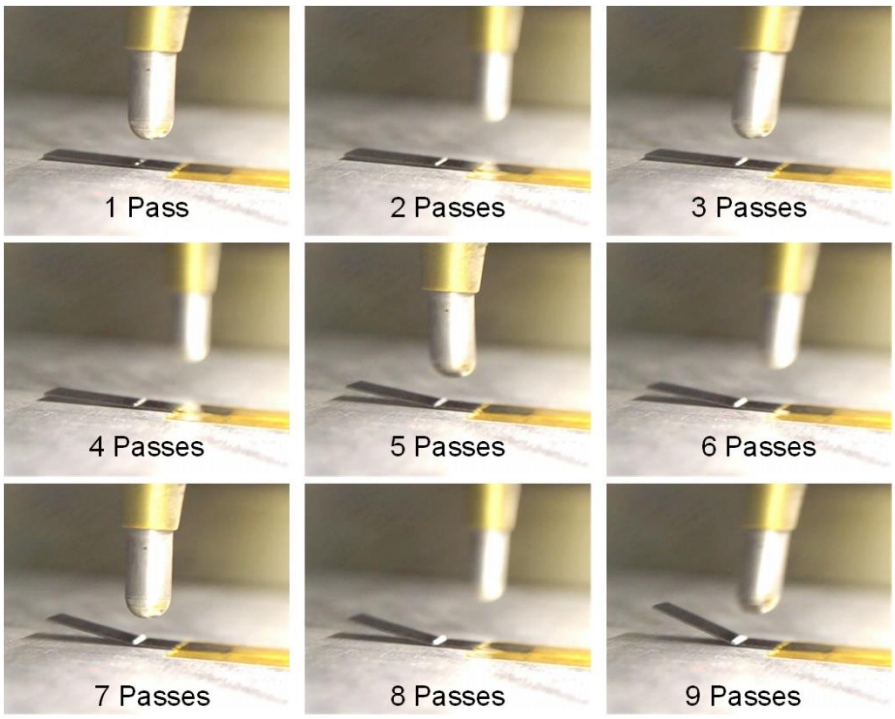

Figure 60: Image frames from in situ videography showing the progression of folding with increasing number of lasing passes at conditions of P = 3.5 W, v =430 mm/s, 2wx = 1 mm, air assist on. The sliver moving part is the laser head plunger, which is used for focusing/defocusing the laser beam on the sample before rastering.

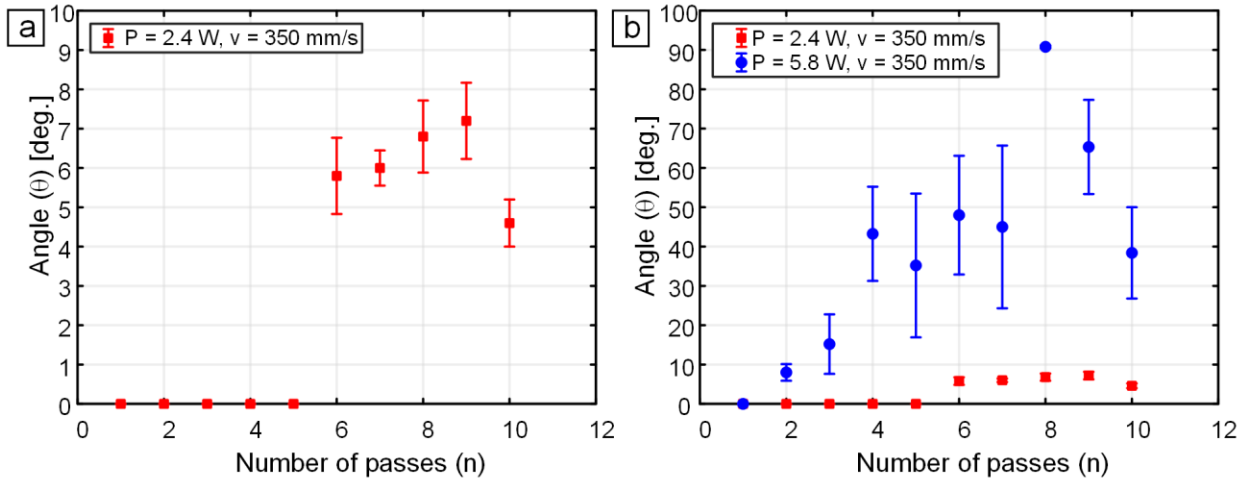

Figure 61: (a) Plot showing the effect of number of passes at fixed power and speed (P = 2.4 W, v =350 mm/s, 2wx = 1 mm). and (b) (P = 5.8 W, v =350 mm/s, 2wx = 1 mm). Error bars indicate standard error based on ten replications. At 8 passes for P = 5.8W, v = 350 m/s the standard error is 0.37.

6.2.4 Influence of Laser Power and Speed on Single Pass Folding

To gain more insight into the process fundamentals, we lase the pre-strained polystyrene for only a single pass (n = 1) at different values of power and speed. We also estimate the corresponding fluence at the different laser conditions to see how fluence is correlated with folding angle. The relationship between power and average fluence is shown in Figure 62 (a) at $2w_x$ = 1 mm. The average fluence is calculated based on Gaussian beam modeling by multiplying the average estimated optical energy flux (as shown in Figure 54 (d)) with the laser dwell time ($t_d=2w_x/v$).

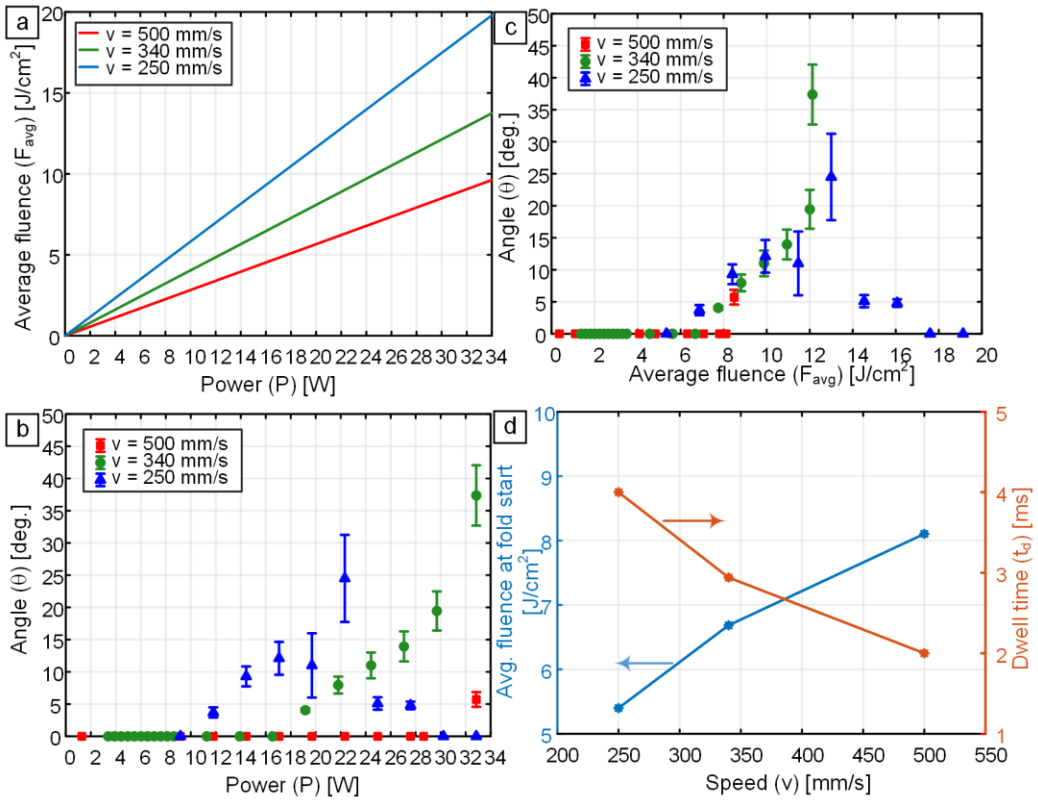

Figure 62: (a) Plot showing how laser power and speed affect laser fluence. (b) Folding angle at different speeds and powers. (Errors bars are the standard error for sample size of 5) (c) Influence of laser fluence and speed on folding angle. (d) Influence of speed and dwell time on the threshold fluence for folding.

The plotted results show that the laser fluence scales linearly with power, with a higher rate of fluence increase at lower speeds. The resulting fold angles at different laser power and speed are shown in Figure 62 (b), with the corresponding fluence values illustrated in Figure 62 (c). The avg. fluence (F_{avg}) at which folding starts is plotted as a function of lasing speed in Figure 62 (d) as well as the dwell time for each laser conditions. For all conditions, folding doesn't start at P < 8 W and F_{avg} < 5.2 J/cm^2, implying that the temperature across the material resulting from these lasing conditions is not high enough to initiate folding (i.e. does not reach the glass transition temperature). It is also noted that the fluence at the initiation of folding is different for each lasing speed. At the lowest speed (v = 250 mm/s), the fluence at which folding starts is at F_{avg} = 5.4 J/cm^2, while at the highest speed (v = 500 mm/s), the fluence at which folding starts is at F_{avg} = 8.2 J/cm^2. For the lowest speed (highest dwell time), an increasing trend is noticed with fluence till a maximum of 25° at a F_{avg} = 13 J/cm^2 after which the folding angle drops with increasing fluence till no folding is observed after F_{avg} = 17 J/cm^2. At v = 340 mm/s, the folding initiates at F_{avg} = 6.8 J/cm^2, and is followed by a monotonic increase in folding angle with average fluence with a maximum average folding angle of 37° at a fluence of F_{avg} = 12 J/cm^2. Further increase of fluence wasn't experimentally achievable due to laser maximum power limitations. It is expected that beyond a certain fluence values, the resulting folding angle will start to decrease, similar to the results obtained at v = 250 mm/s (due to overheating as explained below). At the highest speed, the fluence needed to initiate folding is highest at F = 8.1 J/cm^2. Higher fluence couldn't be delivered due to the maximum laser power limits.

As mentioned earlier, the shrinkage of pre-strained polystyrene films is dependent on the material temperature exceeding the glass transition temperature (T_g), leading to the viscoelastic relaxation locally, which causes the folds. In this case, the resulting fold angle and speed of folding

are dependent on multiple factors. The temporal and spatial temperature distribution (which depend on the laser parameters and material properties) combined with temporal viscoelastic effects (the rate of stress relaxation is also temperature dependent) dictate the observed folding. for low lasing speeds, high fluence and long laser dwell time can lead to low or no folding, because these conditions lead to full stress relaxation of the pre-strain across the polystyrene sheet without gradient of shrinkage across the thickness (hence, no folding is observed for higher power points shown in Figure 62 (b)). We observe this effect experimentally at laser scanning speed at v = 250 mm/s, where the folding angle increased with fluence and then dropped subsequently. Excessive heating can also lead to polystyrene melting and excessive material flow, preventing high quality folding. Future research to elucidate these interactions will focus on thermo-mechanical simulations to study how the lasing conditions interact with the viscoelastic properties of the materials and how they influence the folding dynamics.

6.2.5 Simulation Results

The results of the simulation demonstrate that this approach successfully captures the laser folding behavior with the thermal programming step followed by the laser heating step. Thermal and strain results from the P = 6.5W case are presented in Figure 63. Figure 63 (a, b) demonstrate the thermal gradients across the sheet thickness. Figure 63 (c) demonstrates the steady state strain gradients across the cross section of the sheet driving the folding after laser heating. To help understand the mechanics and kinetics of the process, we plot the change in folding angle with time, the top and bottom surface temperature and strain at the sheet center and the temperature and strain across the thickness at the center of the sheet. The results are presented in Figure 64.

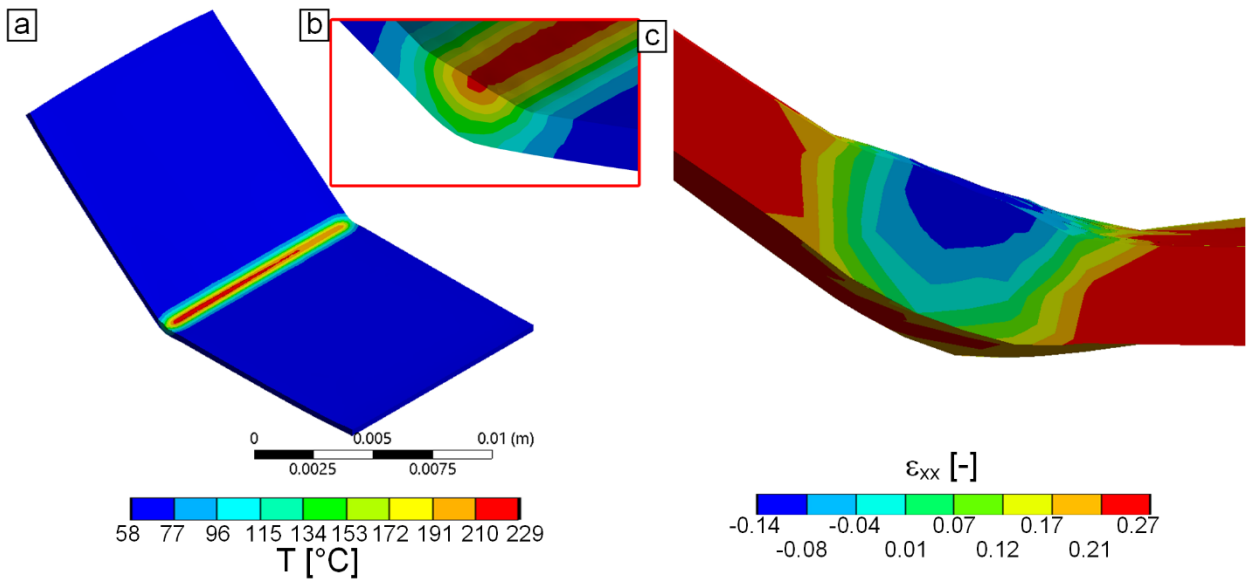

Figure 63: (a) Thermal contour plot at t = 0.137s for the P = 6.5W, v =250 mm/s, z = 8 mm case. (b) Thermal contour plot at the center cross section demostrating the thermal gradients across the cross section at t =0.137 s. (c) Strain contour across the central cross section at steady state for the P = 6.5W, v =250 mm/s, z = 8 mm case.

Figure 64 (a, b, c, d) give a full picture of the kinetics driving the process by monitoring the folding angle during and after the laser heating at the sheet center. At time t_1=0, we notice that both the bottom and top of the sheet are in a state of tensile pre-strain at a value of 0.25, demonstrating the success of the thermal programming step. During the laser pass, the upper surface exceeds the T_g temperature leading to the shrinking of the top surface as observed between t_1 and t_2. This is accompanied by the folding of the sheet to an angle of 40°. The lower surface temperature eventually exceeds T_g at t_2, due to the laser heat conducting through the sheet. The lower face of the sheet also undergoes some shrinkage as well as noted at time t_3 in Figure 64 (a, c). This shrinkage leads to the reduction of the resulting folding to a value of around 30° due to the change in compression strain gradients along the thickness. The change in strain at the upper and lower surface is different from the center due to the convection cooling and asymmetric

heating that happened/is happening at the solid-air interfaces. This drives the piecewise linear shape of the strain curves noted at Figure 64 (c) at t_3, t_4, t_5 and t_6. Eventually, at steady state the strain at the bottom surface is tensile while at the upper surface it is compression, suggesting that the process didn't completely relax the pre-strain across the cross. The net strain led to a folding angle of 35°. No further folding occurs since eventually there are no thermal gradient across the thickness.

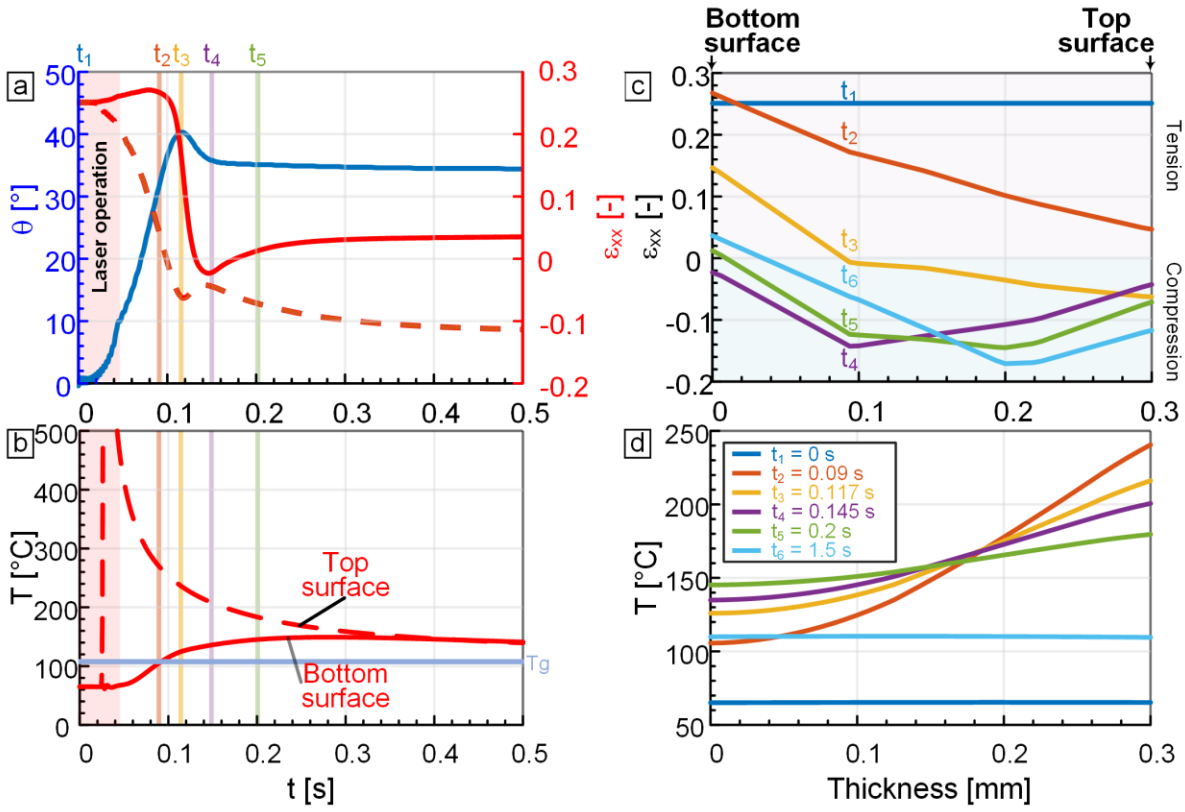

Figure 64: (a) Plot demonstrating the folding angle and strain for the top and bottom of the fold for for the P = 6.5W, v =250 mm/s, z = 8 mm case with t_1 = 0 marking the start of lasing. (b) Temperature at the top and bottom of the fold, with the glass transition temperature Tg illustrated. (c) Plot illustrating the strain acoss the thickness for the different times t_i marked in (a). (d) Plot of the temperature distribution across the thickness at different times during the simulation.

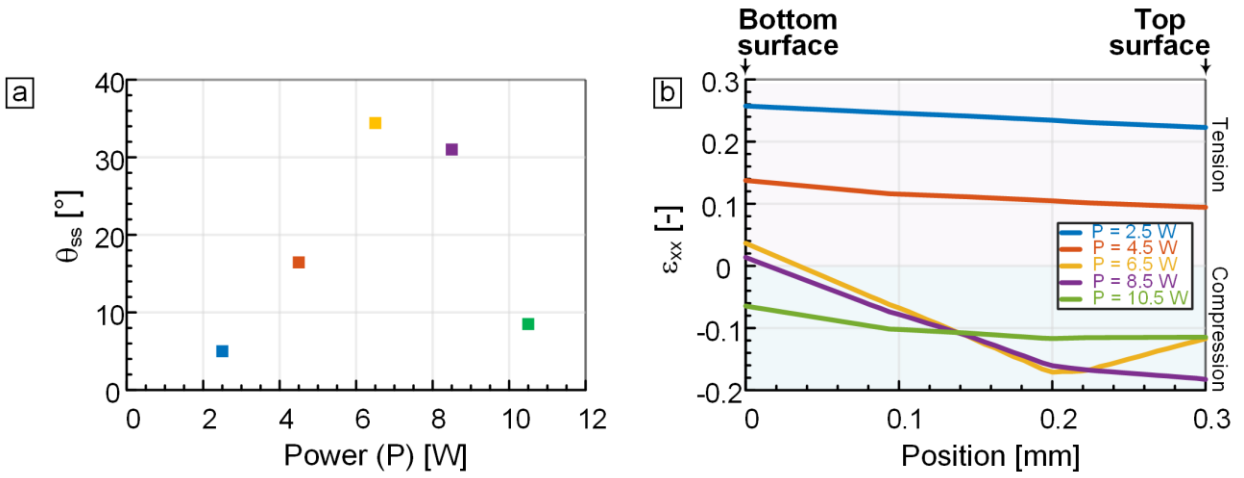

Figure 65: (a) Plot illustrating the steady state folding angle for different lasing power cases for v = 250 mm/s and z = 8 mm. (b) Plot illustrating the steady state strain distributtion across the thickness of the sheet for the corresponding power values in (a).

To get a bigger picture on the influence of power on the steady state folding angle, we evaluate the steady state folding angle and strain distribution resulting from different lasing power values. The results are presented in Figure 65. The results show that initially, with increasing power, the steady state folding angle (θ_{ss}) increases till it reaches a value of 35° beyond which the folding angle drops rapidly beyond P = 8.5 W as observed in Figure 65 (a). This is similar to the trend observed experimentally in Figure 62 (b), which shows a similar trend for v = 250 mm/s albeit for different power values. The results in Figure 65 (b) explain this phenomenon. At lower powers (P = 2.5 W, 4.5 W), the laser heating doesn't lead to significant strain gradients of strain across the thickness, with only tension strain across the cross section, leading to lower folding angles. Beyond a certain power value, the heating leads to steady state tension on the bottom surface and compression on the upper surface, which results in the highest net folding effect at P = 6.5W, 8.5 W and largest strain gradients across the thickness. Beyond these values, the excessive heating leads to only compression strain across the thickness, due to thermal mismatch, not the

pre-strain. Additionally, the strain gradients across the thickness get smaller as well. Overall this approach is an effective technique to understand the fundamentals of this folding process and potentially optimizing the laser conditions for maximizing folding angle. Future work, would be programming the laser scanning for multiple passes, which would enable gradually relaxing the top surface strain without over-relaxing the pre-strain in the bottom surface.

6.2.6 Applications of Complex 3D Geometries

After demonstrating the ability to control both fold angle and quality of fold based on varying laser power and rastering speed, we have also shown that sequential delivery of energy through multiple lasing passes can also be used as a powerful knob to control the localized folding angle. We have combined cutting with folding to illustrate the capability of our approach to create complex 3D geometries like vertex connected triply periodic minimal surface structures which are attractive geometries for mechanical metamaterial applications [138], as shown in Figure 66. This highlights the potential of integrating origami and Kirigami [8] principles in manufacturing.

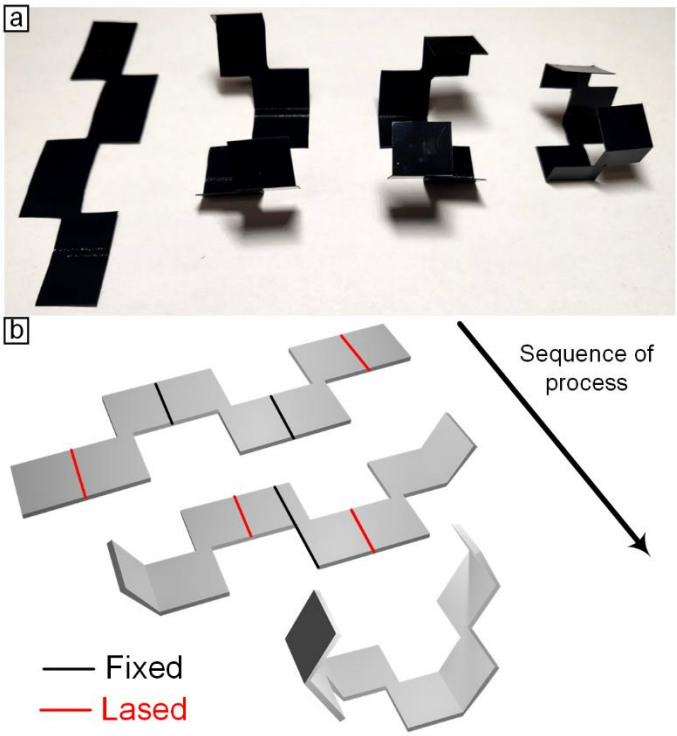

Figure 66: (a)Demonstration of complex shapes such as vertex connected triply periodic minimal surface structures ,created with combining cutting with the laser self-folding approach described in this work. (b) Illustration for the sequence of lasing, with lasing paths and fixation points shown.

We demonstrate the robustness of the produced folds by applying a compressive load on them, as shown in Figure 67. We show that for a load of 1 N does not damage the folds obtained at the lasing conditions of P = 3.5 W, v = 500 mm/s, $2w_x$ = 1 mm, n = 9. In this experiment, a load is applied on top of the vertex of the fold as illustrated in Figure 67 (a), while the sample is mounted on a mass balance. Results show that the fold withstand the load, which the polystyrene elastically deform, and returned to its original configuration upon unloading (Figure 67 (b)) without any damage to the folds. Hence, the resulting geometries obtained by our laser-based folding approach are promising as a building blocks in a repeating architected structure for origami-based energy absorption applications [139] and origami-based cellular metamaterials [140].

Hence, our approach is promising for fabrication of lightweight polymer structures with high surface finish, which is a major advantage compared to common additive manufacturing alternatives. The reason that surface finish is much more superior in our laser-based origami approach compared to 3D printing methods is that the surface finish is dependent on the process of fabricating 2D sheets, which is a rather cost-effective and mature technology. For example, a single 8'' × 11'' sheet of smooth pre-strained polystyrene costs less than 0.4$. Our folding approach is also faster than typical additive manufacturing approaches such as fused deposition modeling and stereo lithography, which also generating minimal waster material.

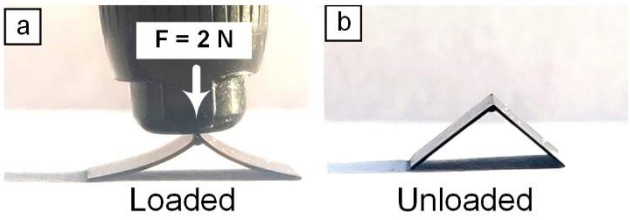

Figure 67: Demonstration for the mechanical robustness of the folds. A compressive load of 2 N was placed on the folds (a). After unloading (b), the fold is shown to be intact without failure.

Our rastering-based approach also invites leveraging computational design tools for control of the spatiotemporal evolution of temperature for achieving desired curves and folds. Combining laser heating, which has the advantage of offering rapid energy delivery with precise control of fluence dose and location of heating, with rastering underscores the versatility of our technique. Among folding-based methods, our approach uniquely allows optimizing the folding angle and minimizing hinge distortion when compared to less abrupt heating methods [19,20]. Another advantage for our approach is that folding happens as a results of a single-step direct-write process, eliminating the need for ink printing. However, further process development is needed to achieve

more complex 3D geometries[26], since shadowing effects can potentially limit the maximum achievable folds and block the laser when lasing large structures. These issues can potentially be remedied by using different scanning methods like using mirror galvanometers to deliver the laser energy fast-enough before shadowing can occur. The approach of directed self-folding based on localized heating can be combined with modern cybermanufacturing infrastructure in order to achieve mass customization in 3D fabrication at on-demand stations or kiosks [141,142].

6.3 Conclusion

In this chapter, we present a new approach for sequential self-folding of polymer sheets, based on laser rastering. The approach is shown to be versatile, allowing direct precise delivery of energy at the hinges, without the need for ink jet printing to sequentially fold the pre-strained polymer sheets. This approach is well suited for creating complex shapes that are difficult to create with 3D printing techniques. From the parametric study results, it is noted that varying the number of lasing passes is a powerful way to achieving high quality folds with desired angles. Additionally, it is observed that power and speed are a direct method for controlling the folding angle with maintaining the quality of the fold. Our findings indicate that there exists optimal conditions that insure both minimal distortion in fold geometries and high precision in the resulting folding angle. Further investigations are needed to correlate the lasing parameters with the spatial variation of fluence and temperature, as well as with the viscoelastic stress relaxation behavior that underlie folding. Additionally, we develop a multi-physics approach to simulate the process, revealing more insight into the process. Taken together, our results highlight the potential of this approach for manufacturing 3D lightweight structures.

7.0 Ongoing and Future Research Directions

In this chapter, we present ongoing and future research directions related to this thesis. This includes designs, applications and developments related to the previously presented LINC research.

7.1 Environmental Control for LINC-based Processes

To study the influence of pressure and gas environment on LINC development, we design a special chamber to control the pressure and environment inside the sample chamber. This is achieved through designing the chamber with KF flange standard parts (typically used in vacuum technology) and a special fabricated ZnSe window (which is transparent to 10.6 μm light).

This allows lasing through the window, while the chamber is held under vacuum or special gas conditions. This would allow introducing doping gases and revealing more about the process fundamentals. 3D CAD models of the design are shown in Figure 68 (a, b). The assembled system is shown in Figure 68 (c). An additional fused silica window is available for fiber lasers.

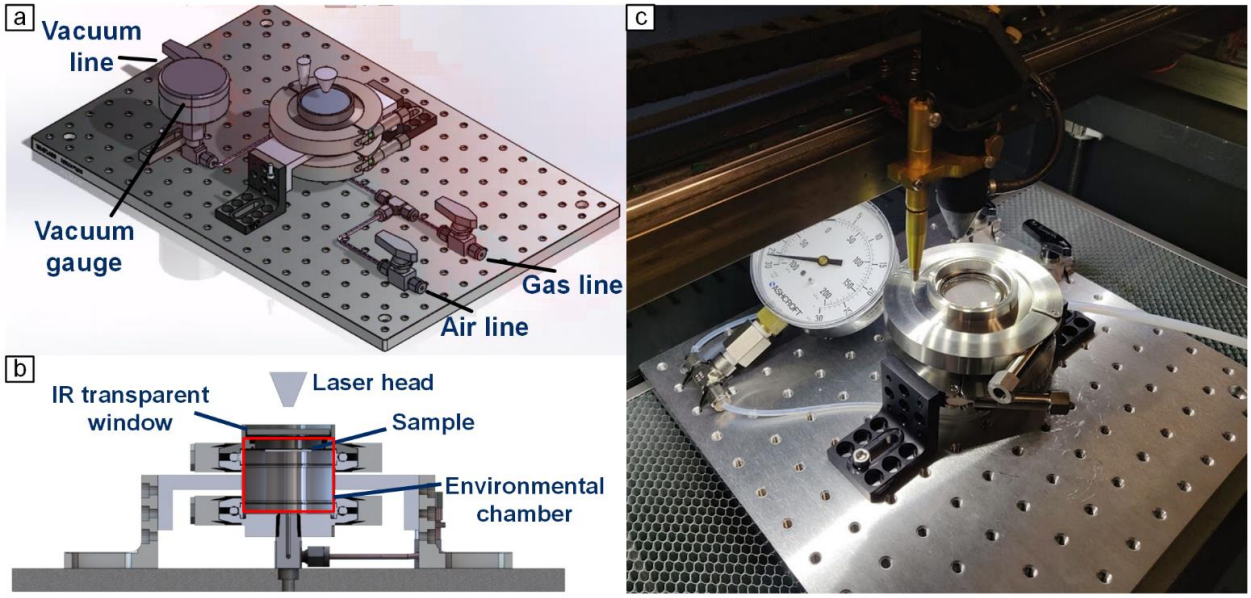

Figure 68: (a,b) 3D CAD model of the laser chamber. (c) Photo of the system installed in the CO2 laser.

7.2 LINC for Contact Angle Control

Another potential application for LINC is surface engineering of commercial polymers. We elucidate the effects of tuning laser processing parameters on the achieved nanoscale morphology and the resulting surface hydrophobicity or hydrophilicity. Our results show that by varying lasing power, rastering speed, laser spot size, and line-to-line gap sizes, a wide range of water contact angles are possible, i.e. from below 20° to above 150° as seen in Figure 69 Combining water contact angle measurements from an optical tensiometer with LINC surface characterization using optical microscopy, electron microscopy, and Raman spectroscopy enables building the process-structure-property relationship. Our findings reveal that both the value of contact angle and the anisotropic wetting behavior of LINC on polyimide are dependent on their hierarchical surface nanostructure which ranges from isotropic nanoporous morphology to fibrous

morphology. Results also show that increasing gap sizes lead to an increase in contact angles and thus an increase in the hydrophobicity of the surface. Hence, our work highlights the potential of this approach for manufacturing flexible devices with tailored surfaces.

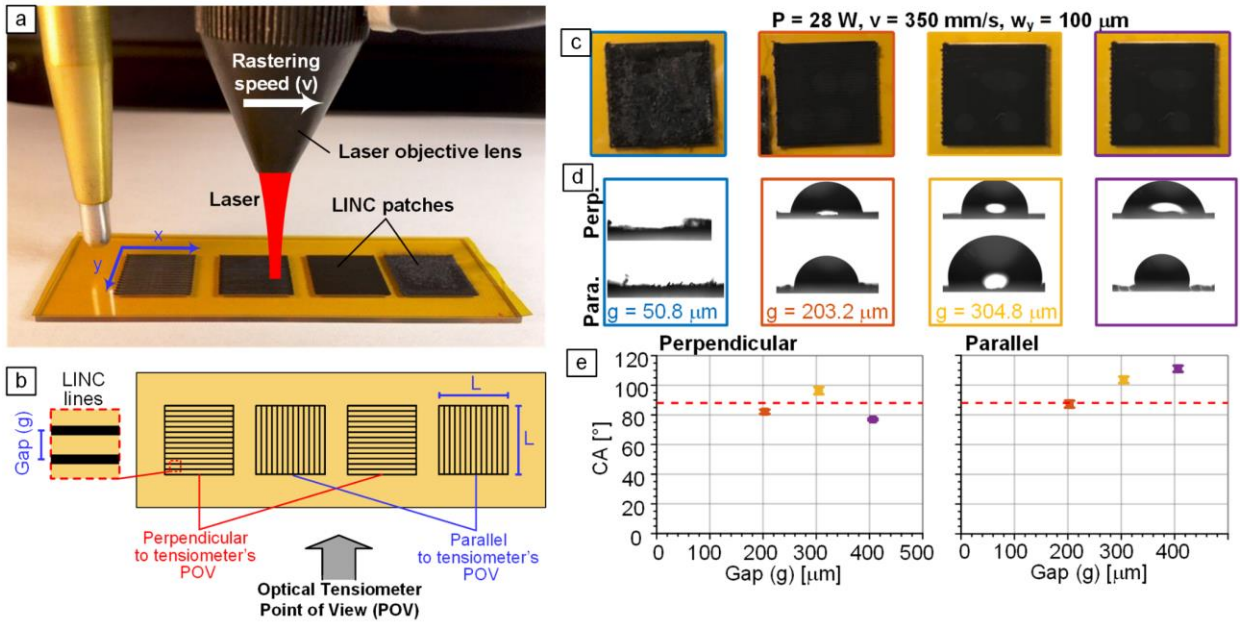

Figure 69: (a, b) Image and schematic illustrating the experimental setup for creating LINC areas for contact angle control. (c-e) Sample of optical sample and contact angle measurements resulting in wicking and hydrophonic surfaces.

7.3 LINC-Based Heaters

One potential application for the approaches described in this work is LINC based spatially patterned heaters. These heaters are the key to many applications in the areas of thermotherapy[143–145], efficient boiling [115] and thermally driven polymer actuation [146–149]. Here we describe different methods for fabricating low cost, facile, flat and flexible thermal

heaters capable of generating distributions of temperature. Through the process of direct write laser carbonization of flexible polymers, spatial distribution of laser graphene morphologies are realized which also demonstrate spatial distributions of resistivity. When the patterns are connected to a current/voltage source, the spatial distributions generate a spatial distribution of temperatures.

In the first method, we exploit a phenomenon in the laser carbonization of polyimide: discrete morphological transitions at specific fluence values described in Chapter 3.0. This feature combined laser defocusing through topographically shaping the flexible substrate for creating continuously lased lines exposed to a spatially continuous range of fluence as illustrated in Figure 70 (a-g). This continuum of fluence leads to a corresponding transition of laser graphene morphology when crossing the threshold value of fluence. The topographical shaping of the substrate allows creating patterns of laser graphene with a corresponding pattern of resistance and hence generated thermal energy that drives the temperature gradients.

In the second approach, the gradients of resistivity in the laser graphene are achieved through relasing as presented in Chapter 5.0. When existing laser graphene is relased, it graphitizes the laser graphene. This subsequently reduces the resistivity of the laser graphene. When connected to a voltage/current source, the drawn current would be distributed based on the patterned spatial resistance gradients leading to thermal gradients as illustrated in Figure 70 (h-k).

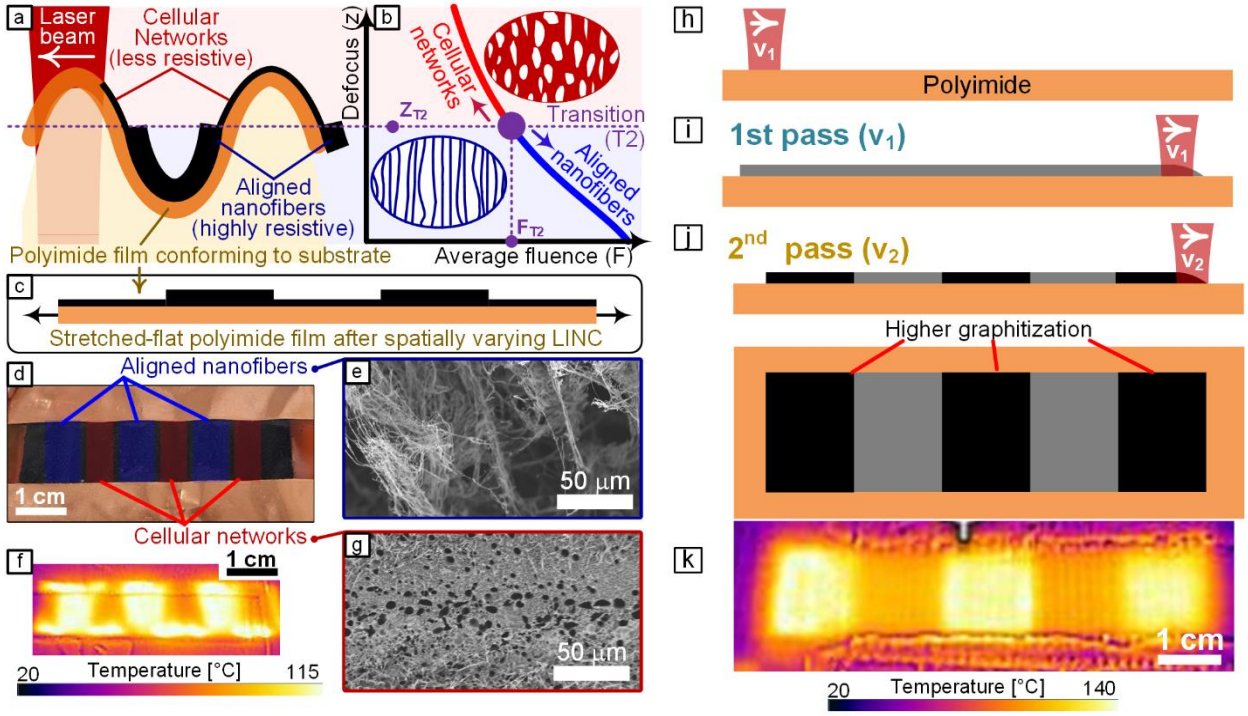

Figure 70: (a-g) Defocusing approach to creating heaters with spatial thermal gradient heaters. (h-k) Relasing based approach to creating spatial thermal gradient heaters.

7.4 LINC Neural Sensors

To demonstrate the bio-sensing capability of LINC, we fabricated heteroatom-doped graphene electrodes. Accordingly, we leverage this laser-induced polymer-to-doped-graphene conversion for fabricating electrically conductive microelectrodes with efficient utilization of heteroatoms (N-doped, F-doped, and S-doped).[132] Tuning laser fluence enabled achieving electrical resistivity lower than ~13 Ω sq^{-1} for F-doped and N-doped graphene. The resulting microelectrodes exhibit superior performance for electrochemical sensing of dopamine, one of the important neurotransmitters in the brain as demonstrated in Figure 71.

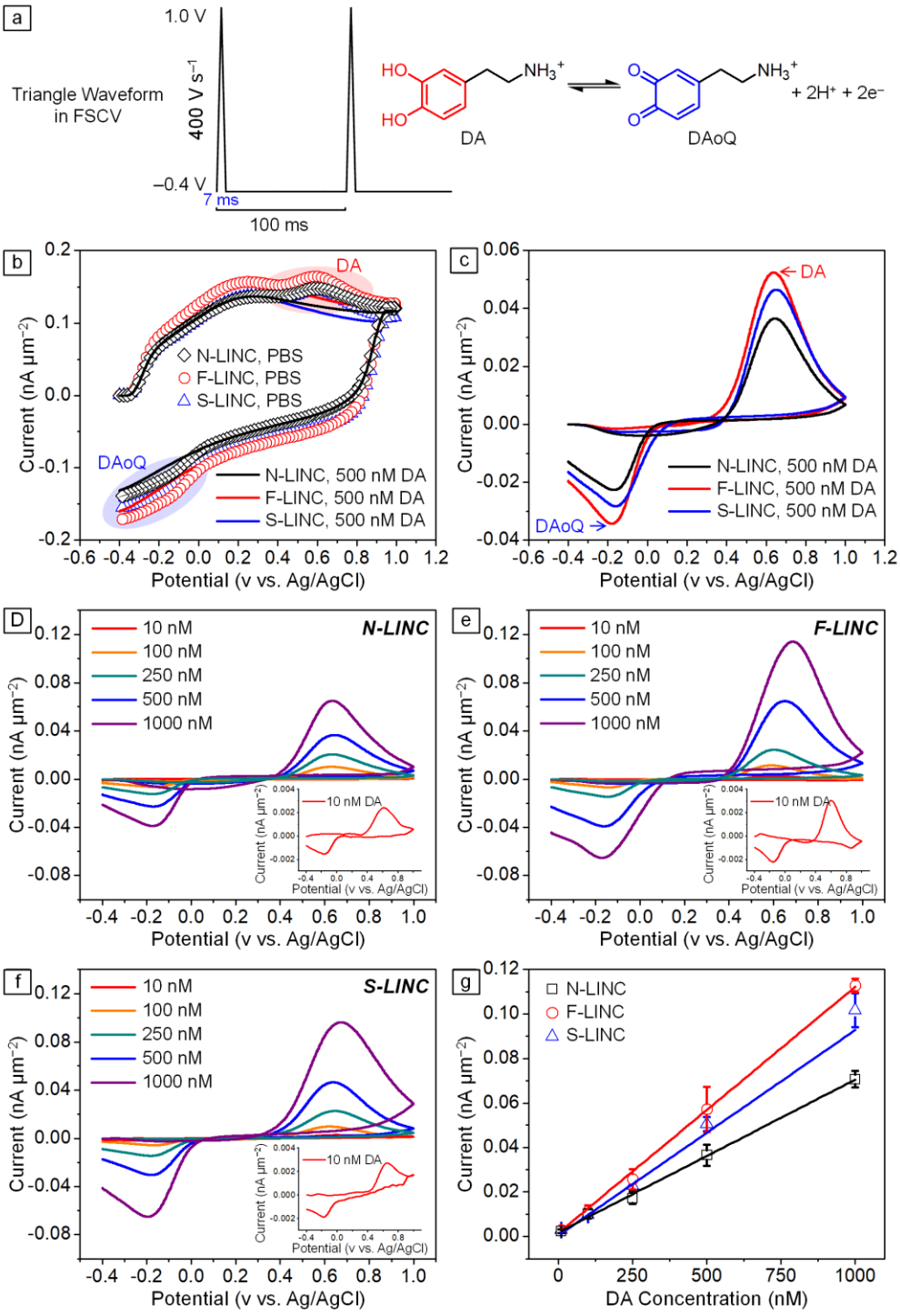

Figure 71: Dopamine sensitivity with three different doped LINC fabricated at *P* = 12.5 W, *v* = 49 mm/s (laser fluence = 170 J cm^{-2}). (a) Schematic of the FSCV waveform used, with holding potential –0.4 V, swhitching potential 1 V at 400 V s^{-1}, 10 Hz (left) and schematic of the two-electrons and two-protons DA reaction (right).

(b) FSCV background current in PBS (lines) and in presence of 500 nM DA (scatters) for N-LINC (black), F-LINC (red), and S-LINC (blue) respectively; (c) corresponding background subtracted CVs, highlight the dopamine oxidation peaks and dopamine-*o*-quinone reduction peaks. Representative background subtracted CVs for 10, 100, 250, 500 nM and 1 μM bolus of DA injection collected using (d) N-LINC, (e) F-LINC, and (f) S-LINC, respectively. Inset: representative background subtracted FSCVs for 10 nM DA concentrations. (g) Calibration curves (10 nM–1.0 μM concentration range) of DA in PBS using N-LINC (black), F-LINC (red), and S-LINC (blue), respectively. Data were calibrated from 7 replicates (n = 7).

Compared with carbon fiber microelectrodes, the gold standard in electrochemical dopamine sensing, our F-doped high surface area graphene microelectrodes demonstrated 3 order of magnitude higher sensitivity per unit area, detecting dopamine concentrations as low as 10 nM with excellent reproducibility. Hence, this approach is promising for facile fabrication of microelectrodes with superior capabilities for various electrochemical and sensing applications including early diagnosis of neurological disorders.

7.5 Fiber Laser Based LINC

LINC processing is inherently a one sided process (i.e. carbonization on only top side), mainly, due to opaqueness of the polyimide to IR lasers, especially for CO_2 laser (λ = 10.6 μm). This limits the architectures of possible LINC devices to planar circuits on one side of the film. Here we develop a novel way to expand the capability of the process by developing a technique enabling selective and simultaneous direct writing of LINC on both sides of the film. One key aspect to this proposed process is the transparency of polyimide films to lasers with smaller wavelength (e.g. 1 μm fiber laser).[68] Combining this transparency with adding a thin layer of

laser absorbing material on either or both sides of the film enables selective carbonization on either or both sides. This process is further enhanced by the increase in opaqueness of polyimide in the heat affected zone ahead of the laser, making the downstream points on the path of a scanned laser opaque, a phenomenon demonstrated for other transparent materials.[74] Preliminary results obtained using a fiber laser (1 μm wavelength) with commercial black permachrome ink as an initiator confirm this selectivity of LINC formation as shown in Figure 70. Future work will investigate the effect of initiator material and thickness on the absorptance of polyimide using UV-vis-NIR spectroscopy in transmission/reflection mode. Moreover, optical properties of initiators will be correlated to resulting LINC atomic structure, morphology, chemistry, and electrical conductivity (as described earlier). Using a Master Oscillator Power Amplifier (MOPA) laser which enables pulse width and frequency (in addition to power and speed) can enable precisely tuning the thermal kinetics.[150,151] This approach could also be key for one-step fabrication of through-film interconnects, as shown in Figure 72. This novel approach will allow unprecedented ability to create complex 3D architectures of LINC having a circuit on the top, another circuit on the bottom, and a through-film interconnect between them. Moreover, this idea can be extended to multilayer films toward more complex 3D flexible electronics. Another mechanism that can be leveraged is non-linear absorption which could trigger multi-photon absorption at specific internal locations across film thickness.[152]

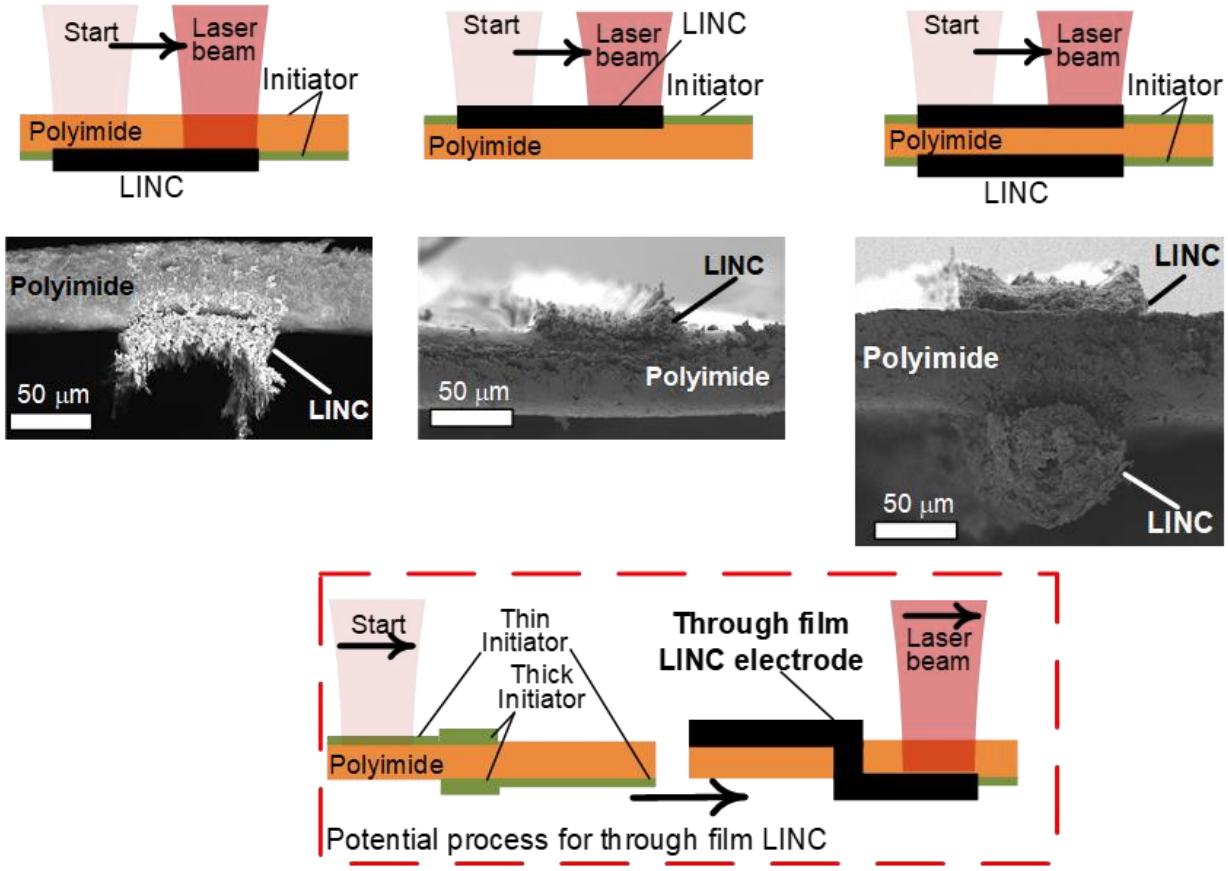

Figure 72: Illustration and SEM images demonstrating different approaches for selective lasing of LINC on polyimide as well as a method for creating LINC based electrical interconnetcs across the polyimide film.

The small spot size of the fiber laser allows fabricating thin electrodes that are 40 μm thick. These electrodes can be leveraged for implantable neural sensing electrodes on flexible polyimide. As an example a set of microelectrode arrays are made using the fiber laser as demonstrated in Figure 73.

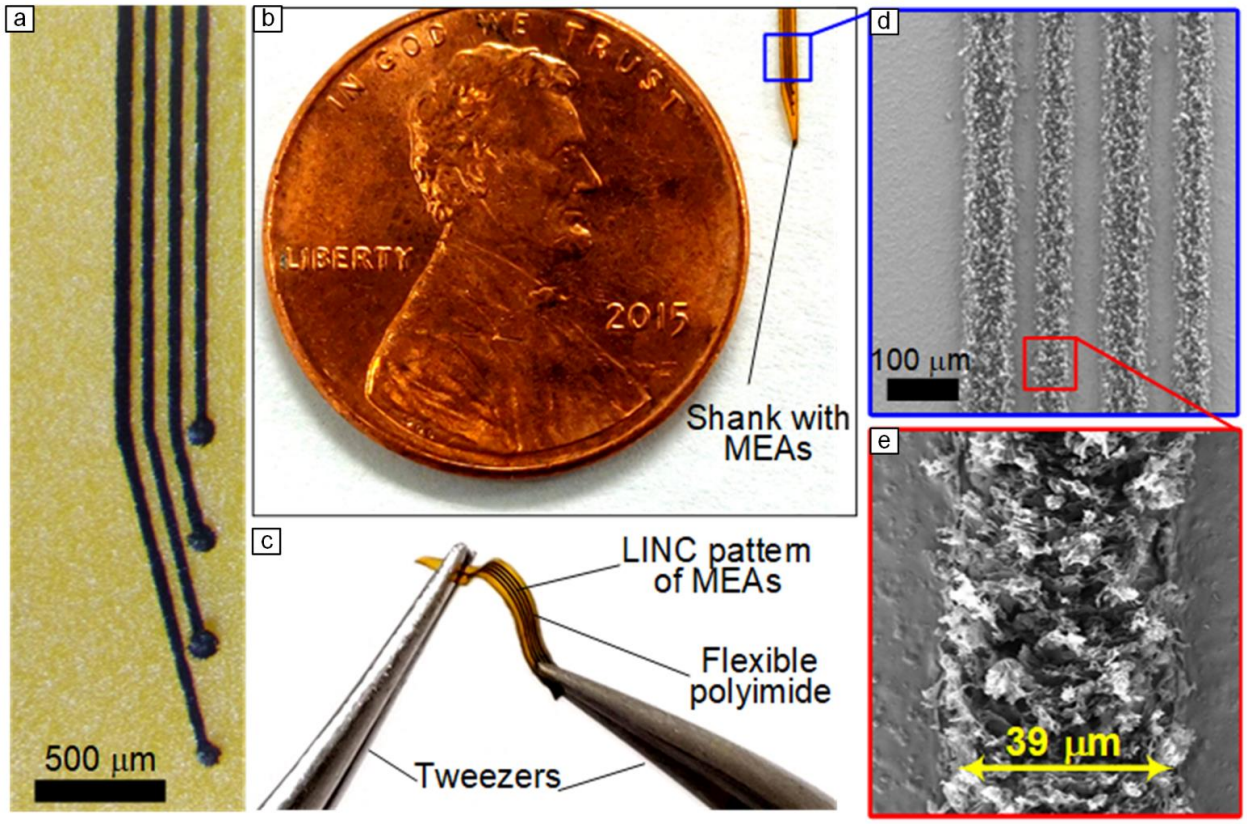

Figure 73: (a-c) Optical image of 40 μm wide MEA arrays. (d-e) SEM images of the MEA electrodes demonstrating the array width

8.0 Conclusions

Laser processing of polymer is a versatile process that enables a plethora of manufacturing process that enable the fabrication of 3D shapes and functional flexible devices, all under the same platform. Throughout this thesis we investigate the fundamentals of two of these processes: laser induced carbonization of polymer and laser based self-folding of shape memory polymers. By using experimental, analytical and numerical methods, we reveal many insights into the processes as summarized in the following section.

8.1 Contributions

1) Developed framework to study and analyze the energetics and kinetics of laser induced na nocarbon based electrode formation and how it connects to the resulting the morphology, molecular structure and chemistry of LINC using analytical, SEM, XRD, XPS, TEM and Raman spectroscopy methods.
2) Developed a thermal model to study the process kinetics using the finite element approac h to explain experimental results of LINC formation at different speeds.
3) Developed phenomenologically based hypothesis explaining the fundamentals of formatio n of the different LINC morphologies.
4) Developed methods for optimizing laser conditions for LINC conductivity and electroche mistry for heater, surface engineering and bio-sensing applications.
5) Designed and assembled an environmental chamber that allows creating a vacuum enviro nment and gas environments to aid in investigating the effect of changing lasing environm ent on the laser morphology and properties.
6) Developed novel techniques for lasing 30 μm LINC electrodes using a 1.06 μm pulsed fib er laser with a smaller spot size, which typically generates laser light that isn't absorbed st rongly by polyimide.

7) Developed methods for surface texturing for developing superhydrophobic and hydrophili c LINC surfaces.
8) Developed a method for achieving laser based self-folding of shape memory polymers an d optimizing the process parameters for high quality folds.
9) Developed a multi-physics thermal model of the folding process to understand the driving phenomenon behind the process.

8.2 Publication Based on Contributions from This Thesis

- **Abdulhafez, M.**, Tomaraei, G. N., and Bedewy, M., 2022, "Kinetically Controlled Laser Induced Graphene and Ablation Thresholds," In Preparation
- **Abdulhafez, M.**, Castagnola, E., Baglieri, G., Tomaraei, G. N., Cui, X. T., and Bedewy, M., 2022, "Low Impedance Laser-Induced Graphene Microelectrodes with Relase-Speed-Dependent Properties," In Preparation
- **Abdulhafez, M**., and Bedewy, M., "Kinetics of Self-Folding of Shape Memory Polymer Sheets by Laser Rastering," In Preparation
- **Abdulhafez, M.**, Tomaraei, G. N., and Bedewy, M., 2021, "Fluence-Dependent Morphological Transitions in Laser-Induced Graphene Electrodes on Polyimide Substrates for Flexible Devices," *ACS Appl. Nano Mater.*, 4(3), pp. 2973–2986.
- **Abdulhafez, M**., McComb, A. J., and Bedewy, M., 2020, "Tailoring Surface Hydrophobicity of Commercial Polyimide by Laser-Induced Nanocarbon Texturing," *J. Micro Nano-Manufacturing*, 8(3), p. 031006.
- **Abdulhafez, M**., Line, J., and Bedewy, M., 2021, "Sequential Self-Folding of Shape Memory Polymer Sheets by Laser Rastering Toward Origami-Based Manufacturing*," J. Manuf. Sci. Eng*., 143(9), pp. 1–9.

- Nam, K., **Abdulhafez, M**., Najaf Tomaraei, G., and Bedewy, M., 2021, "Laser-Induced Fluorinated Graphene for Superhydrophobic Surfaces with Anisotropic Wetting and Switchable Adhesion," Appl. Surf. Sci., p. 151339.
- Nam, K.-H., **Abdulhafez, M**., Castagnola, E., Tomaraei, G. N., Cui, X. T., and Bedewy, M., 2021, "Laser Direct Write of Heteroatom-Doped Graphene on Molecularly Controlled Polyimides for Electrochemical Biosensors with Nanomolar Sensitivity," Carbon.
- Elsisy, M., Poska, E., **Abdulhafez, M.**, and Bedewy, M., 2021, "Current-Dependent Dynamics of Bidirectional Self-Folding for Multi-Layer Polymers Using Local Resistive Heating," J. Eng. Mater. Technol., 143(3), pp. 1–26.

8.3 Publications Based on Related /Synergetic Topics

- **Abdulhafez, M**., Kadry, K., Zaazoue, M., Goumnerova, L. C., and Bedewy, M., 2018, "Biomechanical Root Cause Analysis of Complications in Head Immobilization Devices for Pediatric Neurosurgery," Proceedings of the 2018 Manufacturing Science and Engineering Conference, Volume 1: Additive Manufacturing; Bio and Sustainable Manufacturing, American Society of Mechanical Engineers, College Station, pp. 1–10.
- **Abdulhafez, M**., Lee, J., and Bedewy, M., 2020, "In Situ Measurement of Carbon Nanotube Growth Kinetics in a Rapid Thermal Chemical Vapor Deposition Reactor With Multizone Infrared Heating," J. Micro Nano-Manufacturing, 8(1).

- Lee*, J., **Abdulhafez*, M**., and Bedewy, M., 2019, "Decoupling Catalyst Dewetting, Gas Decomposition, and Surface Reactions in Carbon Nanotube Forest Growth Reveals Dependence of Density on Nucleation Temperature," J. Phys. Chem. C, 123(47), pp. 28726–28738. (Equal contribution)
- Lee, J., **Abdulhafez, M**., and Bedewy, M., 2019, "Data Analytics Enables Significant Improvement of Robustness in Chemical Vapor Deposition of Carbon Nanotubes Based on Vacuum Baking," Ind. Eng. Chem. Res., 58(27), pp. 11999–12009.
- Cho, S. Y., **Abdulhafez, M.**, Lee, M. E., Jin, H.-J., and Bedewy, M., 2018, "Promoting Helix-Rich Structure in Silk Fibroin Films through Molecular Interactions with Carbon Nanotubes and Selective Heating for Transparent Biodegradable Devices," ACS Appl. Nano Mater., 1(10), pp. 5441–5450.
- Lee, J., **Abdulhafez, M**., and Bedewy, M., 2019, "Multizone Rapid Thermal Processing to Overcome Challenges in Carbon Nanotube Manufacturing by Chemical Vapor Deposition," J. Manuf. Sci. Eng., 141(9).
- Lee, J., Tomaraei, G. N., **Abdulhafez, M.,** and Bedewy, M., 2021, "Boosting Catalytic Lifetime in Chemical Vapor Deposition of Carbon Nanotubes by Rapid Thermal Pretreatment of Alumina-Supported Metal Nanocatalyst," Chem. Mater., pp. 1–49.
- Tomaraei, G., Lee, J., **Abdulhafez, M.**, and Bedewy, M., 2021, "Reducing Variability in Chemical Vapor Deposition of Carbon Nanotubes Based on Gas Purification and Sample Support Redesign," J. Micro Nano-Manufacturing, 9(1), pp. 1–8.

Bibliography

[1] Boyvat, M., Koh, J., and Wood, R. J., 2017, "Addressable Wireless Actuation for Multijoint Folding Robots and Devices," Sci. Robot., **2**(8), p. eaan1544.

[2] Birkmeyer, P., Peterson, K., and Fearing, R. S., 2009, "DASH: A Dynamic 16g Hexapedal Robot," 2009 IEEE/RSJ Int. Conf. Intell. Robot. Syst. IROS 2009, pp. 2683–2689.

[3] Miskin, M. Z., Cortese, A. J., Dorsey, K., Esposito, E. P., Reynolds, M. F., Liu, Q., Cao, M., Muller, D. A., McEuen, P. L., and Cohen, I., 2020, "Electronically Integrated, Mass-Manufactured, Microscopic Robots," Nature, **584**(7822), pp. 557–561.

[4] Gu, G., Zou, J., Zhao, R., Zhao, X., and Zhu, X., 2018, "Soft Wall-Climbing Robots," Sci. Robot., **3**(25), p. eaat2874.

[5] Hu, C., Pané, S., and Nelson, B. J., 2018, "Soft Micro- and Nanorobotics," Annu. Rev. Control. Robot. Auton. Syst., **1**(1), pp. 53–75.

[6] Rus, D., and Tolley, M. T., 2018, "Design, Fabrication and Control of Origami Robots," Nat. Rev. Mater., **3**(6), pp. 101–112.

[7] Elsisy, M., Poska, E., Abdulhafez, M., and Bedewy, M., 2021, "Current-Dependent Dynamics of Bidirectional Self-Folding for Multi-Layer Polymers Using Local Resistive Heating," J. Eng. Mater. Technol., **143**(3), pp. 1–26.

[8] Lamoureux, A., Lee, K., Shlian, M., Forrest, S. R., and Shtein, M., 2015, "Dynamic Kirigami Structures for Integrated Solar Tracking," Nat. Commun., **6**, pp. 1–6.

[9] Felton, S., Tolley, M., Demaine, E., Rus, D., and Wood, R., 2014, "A Method for Building Self-Folding Machines," Science (80-.)., **345**(6197), pp. 644–646.

[10] Kellermayer, M. S. Z., Smith, S. B., Granzier, H. L., and Bustamante, C., 1997, "Folding-Unfolding Transitions in Single Titin Molecules Characterized with Laser Tweezers," Science (80-.)., **276**(5315), pp. 1112–1116.

[11] Saito, K., Nomura, S., Yamamoto, S., Niyama, R., and Okabe, Y., 2017, "Investigation of Hindwing Folding in Ladybird Beetles by Artificial Elytron Transplantation and Microcomputed Tomography," Proc. Natl. Acad. Sci. U. S. A., **114**(22), pp. 5624–5628.

[12] Todd, P. H., 1982, "A Geometric Model for the Cortical Folding Pattern of Simple Folded Brains," J. Theor. Biol., **97**(3), pp. 529–538.

[13] Mahadevan, L., and Rica, S., 2005, "Self-Organized Origami," Science (80-.)., **307**(5716), p. 1740.

[14] Yakacki, C. M., Shandas, R., Lanning, C., Rech, B., Eckstein, A., and Gall, K., 2007, "Unconstrained Recovery Characterization of Shape-Memory Polymer Networks for Cardiovascular Applications," Biomaterials, **28**(14), pp. 2255–2263.

[15] Morgan, J., Magleby, S. P., and Howell, L. L., 2016, "An Approach to Designing Origami-Adapted Aerospace Mechanisms," J. Mech. Des. Trans. ASME, **138**(5).

[16] Song, Z., Ma, T., Tang, R., Cheng, Q., Wang, X., Krishnaraju, D., Panat, R., Chan, C. K., Yu, H., and Jiang, H., 2014, "Origami Lithium-Ion Batteries," Nat. Commun., **5**.

[17] Mueller, S., Kruck, B., and Baudisch, P., 2013, "LaserOrigami," *CHI '13 Extended Abstracts on Human Factors in Computing Systems on - CHI EA '13*, ACM Press, New York, New York, USA, p. 2851.

[18] Liu, Y., Shaw, B., Dickey, M. D., and Genzer, J., 2017, "Sequential Self-Folding of Polymer Sheets," Sci. Adv., **3**(3), pp. 1–7.

[19] Liu, Y., Boyles, J. K., Genzer, J., and Dickey, M. D., 2012, "Self-Folding of Polymer Sheets Using Local Light Absorption," Soft Matter.

[20] Elsisy, M., Poska, E., and Bedewy, M., 2018, "Current-Dependent Kinetics of Self-Folding for Multi-Layer Polymers Using Local Resistive Heating," *Proceedings of the 2018 Manufacturing Science and Engineering Conference*, p. V002T04A017.

[21] Cho, J. H., Azam, A., and Gracias, D. H., 2010, "Three Dimensional Nanofabrication Using Surface Forces," Langmuir, **26**(21), pp. 16534–16539.

[22] Felton, S. M., Tolley, M. T., Shin, B., Onal, C. D., Demaine, E. D., Rus, D., and Wood, R. J., 2013, "Self-Folding with Shape Memory Composites," Soft Matter, **9**(32), pp. 7688–7694.

[23] Davis, D., Mailen, R., Genzer, J., and Dickey, M. D., 2015, "Self-Folding of Polymer Sheets Using Microwaves and Graphene Ink," RSC Adv., **5**(108), pp. 89254–89261.

[24] Suzuki, K., Yamada, H., Miura, H., and Takanobu, H., 2007, "Self-Assembly of Three Dimensional Micro Mechanisms Using Thermal Shrinkage of Polyimide," Microsyst. Technol., **13**(8–10), pp. 1047–1053.

[25] Lee, J. G., Won, S., Park, J. E., and Wie, J. J., 2020, "Multifunctional Three-Dimensional Curvilinear Self-Folding of Glassy Polymers," J. Micro Nano-Manufacturing, **8**(3), pp. 1–7.

[26] Lee, J. H., Choi, J. C., Won, S., Lee, J. W., Lee, J. G., Kim, H. R., and Wie, J. J., 2020, "Light-Driven Complex 3D Shape Morphing of Glassy Polymers by Resolving Spatio-Temporal Stress Confliction," Sci. Rep., **10**(1), pp. 1–12.

[27] Liu, Y., Miskiewicz, M., Escuti, M. J., Genzer, J., and Dickey, M. D., 2014, "Three-Dimensional Folding of Pre-Strained Polymer Sheets via Absorption of Laser Light," J. Appl. Phys., **115**(20).

[28] Piqué, A., Mathews, S. A., Charipar, N. A., and Birnbaum, A. J., 2012, "Laser Origami: A New Technique for Assembling 3D Microstructures," Laser-based Micro- Nanopackaging Assem. VI. Proc. SPIE, **8244**, p. 82440B.

[29] Tolley, M. T., Felton, S. M., Miyashita, S., Aukes, D., Rus, D., and Wood, R. J., 2014, "Self-Folding Origami: Shape Memory Composites Activated by Uniform Heating," Smart Mater. Struct., **23**(9), p. 094006.

[30] Lin, J., Peng, Z., Liu, Y., Ruiz-Zepeda, F., Ye, R., Samuel, E. L. G. G., Yacaman, M. J., Yakobson, B. I., and Tour, J. M., 2014, "Laser-Induced Porous Graphene Films from Commercial Polymers," Nat. Commun., **5**(1), p. 5714.

[31] In, J. Bin, Hsia, B., Yoo, J. H., Hyun, S., Carraro, C., Maboudian, R., and Grigoropoulos, C. P., 2015, "Facile Fabrication of Flexible All Solid-State Micro-Supercapacitor by Direct Laser Writing of Porous Carbon in Polyimide," Carbon, **83**, pp. 144–151.

[32] Li, L., Zhang, J., Peng, Z., Li, Y., Gao, C., Ji, Y., Ye, R., Kim, N. D., Zhong, Q., Yang, Y., Fei, H., Ruan, G., and Tour, J. M., 2016, "High-Performance Pseudocapacitive Microsupercapacitors from Laser-Induced Graphene," Adv. Mater., **28**(5), pp. 838–845.

[33] Singh, S. P., Li, Y., Be'er, A., Oren, Y., Tour, J. M., and Arnusch, C. J., 2017, "Laser-Induced Graphene Layers and Electrodes Prevents Microbial Fouling and Exerts Antimicrobial Action," ACS Appl. Mater. Interfaces, **9**(21), pp. 18238–18247.

[34] Chen, X., Luo, F., Yuan, M., Xie, D., Shen, L., Zheng, K., Wang, Z., Li, X., and Tao, L., 2019, "A Dual-Functional Graphene-Based Self-Alarm Health-Monitoring E-Skin," Adv. Funct. Mater., **29**(51), p. 1904706.

[35] Stanford, M. G., Zhang, C., Fowlkes, J. D., Hoffman, A., Ivanov, I. N., Rack, P. D., and Tour, J. M., 2020, "High-Resolution Laser-Induced Graphene. Flexible Electronics beyond the Visible Limit," ACS Appl. Mater. Interfaces, **12**(9), pp. 10902–10907.

[36] Saidina, D. S., Eawwiboonthanakit, N., Mariatti, M., Fontana, S., and Hérold, C., 2019, "Recent Development of Graphene-Based Ink and Other Conductive Material-Based Inks for Flexible Electronics," J. Electron. Mater., **48**(6), pp. 3428–3450.

[37] Huang, Q., and Zhu, Y., 2019, "Printing Conductive Nanomaterials for Flexible and Stretchable Electronics: A Review of Materials, Processes, and Applications," Adv. Mater. Technol., **4**(5), p. 1800546.

[38] Srinivasan, R., 1986, "Ablation of Polymers and Biological Tissue by Ultraviolet Lasers," Science (80-.)., **234**(4776), pp. 559–565.

[39] Schumann, M., Sauerbrey, R., and Smayling, M. C., 1991, “Permanent Increase of the Electrical Conductivity of Polymers Induced by Ultraviolet Laser Radiation,” Appl. Phys. Lett., **58**(4), pp. 428–430.

[40] Phillips, H. M., Wahl, S., and Sauerbrey, R., 1993, “Submicron Electrically Conducting Wires Produced in Polyimide by Ultraviolet Laser Irradiation,” Appl. Phys. Lett., **62**(20), pp. 2572–2574.

[41] Feurer, T., Sauerbrey, R., Smayling, M. C., and Story, B. J., 1993, “Ultraviolet-Laser-Induced Permanent Electrical Conductivity in Polyimide,” Appl. Phys. A Solids Surfaces, **56**(3), pp. 275–281.

[42] Srinivasan, R., 1993, “Ablation of Polyimide (Kapton ™) Films by Pulsed (Ns) Ultraviolet and Infrared (9.17 Mm) Lasers,” Appl. Phys. A Solids Surfaces, **56**(5), pp. 417–423.

[43] Srinivasan, R., Hall, R. R., Wilson, W. D., Loehle, W. D., and Allbee, D. C., 1994, “Ultraviolet Laser Irradiation of the Polyimide, PMDA-ODA (Kapton™), to Yield a Patternable, Porous, Electrically Conducting Carbon Network,” Synth. Met., **66**(3), pp. 301–307.

[44] Srinivasan, R., Hall, R. R., and Allbee, D. C., 1993, “Generation of Electrically Conducting Features in Polyimide (Kapton ™) Films with Continuous Wave, Ultraviolet Laser Radiation,” Appl. Phys. Lett., **63**(24), pp. 3382–3383.

[45] Endo, M., Hakamada, K., Kim, C., Miyazawa, N., and Kasai, T., 1998, “Raman Spectra of Carbon Film Obtained by Pulse-Laser Irradiation to Polyimide,” Tanso, **1998**(183), pp. 156–161.

[46] Dyer, P. E., Pervolaraki, M., and Lippert, T., 2005, “Experimental Studies and Thermal Modelling of 1064- And 532-Nm Nd:YVO 4 Micro-Laser Ablation of Polyimide,” Appl. Phys. A Mater. Sci. Process., **80**(3), pp. 529–536.

[47] Davenas, J., 1989, “Laser and Ion Beam Processing of Conductive Polyimide,” Appl. Surf. Sci., **36**(1–4), pp. 539–544.

[48] Raffel, J. I., Freidin, J. F., and Chapman, G. H., 1983, “Laser-formed Connections Using Polyimide,” Appl. Phys. Lett., **42**(8), pp. 705–706.

[49] Yang, Y., Song, Y., Bo, X., Min, J., Pak, O. S., Zhu, L., Wang, M., Tu, J., Kogan, A., Zhang, H., Hsiai, T. K., Li, Z., and Gao, W., 2020, “A Laser-Engraved Wearable Sensor for Sensitive Detection of Uric Acid and Tyrosine in Sweat,” Nat. Biotechnol., **38**(2), pp. 217–224.

[50] Tao, L.-Q., Tian, H., Liu, Y., Ju, Z.-Y., Pang, Y., Chen, Y.-Q., Wang, D.-Y., Tian, X.-G., Yan, J.-C., Deng, N.-Q., Yang, Y., and Ren, T.-L., 2017, “An Intelligent Artificial Throat with Sound-Sensing Ability Based on Laser Induced Graphene,” Nat. Commun., **8**(1), p. 14579.

[51] Singh, S. P., Li, Y., Zhang, J., Tour, J. M., and Arnusch, C. J., 2018, "Sulfur-Doped Laser-Induced Porous Graphene Derived from Polysulfone-Class Polymers and Membranes," ACS Nano, **12**(1), pp. 289–297.

[52] Rahimi, R., Ochoa, M., Yu, W., and Ziaie, B., 2015, "Highly Stretchable and Sensitive Unidirectional Strain Sensor via Laser Carbonization," ACS Appl. Mater. Interfaces, **7**(8), pp. 4463–4470.

[53] Luo, S., Hoang, P. T., and Liu, T., 2016, "Direct Laser Writing for Creating Porous Graphitic Structures and Their Use for Flexible and Highly Sensitive Sensor and Sensor Arrays," Carbon, **96**, pp. 522–531.

[54] Duan, X., Yao, Y., Niu, M., Luo, J., Wang, R., and Liu, T., 2019, "Direct Laser Writing of Functional Strain Sensors in Polyimide Tubes," ACS Appl. Polym. Mater., **1**, pp. 2914–2923.

[55] Stanford, M. G., Yang, K., Chyan, Y., Kittrell, C., and Tour, J. M., 2019, "Laser-Induced Graphene for Flexible and Embeddable Gas Sensors," ACS Nano, **13**, pp. 3474–3482.

[56] Rahimi, R., Ochoa, M., and Ziaie, B., 2016, "Direct Laser Writing of Porous-Carbon/Silver Nanocomposite for Flexible Electronics," ACS Appl. Mater. Interfaces, **8**(26), pp. 16907–16913.

[57] Singh, S. P., Ramanan, S., Kaufman, Y., and Arnusch, C. J., 2018, "Laser-Induced Graphene Biofilm Inhibition: Texture Does Matter," ACS Appl. Nano Mater., **1**(4), pp. 1713–1720.

[58] Nasser, J., Lin, J., Zhang, L., and Sodano, H. A., 2020, "Laser Induced Graphene Printing of Spatially Controlled Super-Hydrophobic/Hydrophilic Surfaces," Carbon, **162**, pp. 570–578.

[59] Luong, D. X., Yang, K., Yoon, J., Singh, S. P., Wang, T., Arnusch, C. J., and Tour, J. M., 2019, "Laser-Induced Graphene Composites as Multifunctional Surfaces," ACS Nano, **13**(2), pp. 2579–2586.

[60] Duy, L. X., Peng, Z., Li, Y., Zhang, J., Ji, Y., and Tour, J. M., 2018, "Laser-Induced Graphene Fibers," Carbon, **126**(7), pp. 472–479.

[61] Lamberti, A., Perrucci, F., Caprioli, M., Serrapede, M., Fontana, M., Bianco, S., Ferrero, S., and Tresso, E., 2017, "New Insights on Laser-Induced Graphene Electrodes for Flexible Supercapacitors: Tunable Morphology and Physical Properties," Nanotechnology, **28**(17), p. 174002.

[62] Zeng, D. W., Yung, K. C., and Xie, C. S., 2002, "XPS Investigation of the Chemical Characteristics of Kapton Films Ablated by a Pulsed TEA CO2 Laser," Surf. Coatings Technol., **153**(2–3), pp. 210–216.

[63] Wang, R., Duan, X., Yao, J., Ruan, X., Yao, Y., and Liu, T., 2020, "Processing–Structure–Property Relationship in Direct Laser Writing Carbonization of Polyimide," J. Appl. Polym. Sci., **137**(34), p. 48978.

[64] Bilger, H. R., and Habib, T., 1985, "Knife-Edge Scanning of an Astigmatic Gaussian Beam," Appl. Opt., **24**(5), p. 686.

[65] Poprawe, R., Boucke, K., and Hoffman, D., 2018, *Tailored Light 1*.

[66] Poprawe, R., 2004, *Tailored Light 2 Laser Applicaiton Technology*, Springer.

[67] Jiang, J., Jacobs, A. G., Wenning, B., Liedel, C., Thompson, M. O., and Ober, C. K., 2017, "Ultrafast Self-Assembly of Sub-10 Nm Block Copolymer Nanostructures by Solvent-Free High-Temperature Laser Annealing," ACS Appl. Mater. Interfaces, **9**(37), pp. 31317–31324.

[68] Palm, W. J., 2012, "Wavelength and Temperature Dependence of Continuous-Wave Laser Absorptance in Kapton® Thin Films," Opt. Eng., **51**(12), p. 121802.

[69] Ferrari, A. C., and Robertson, J., 2004, "Raman Spectroscopy of Amorphous, Nanostructured, Diamond–like Carbon, and Nanodiamond," Philos. Trans. R. Soc. London. Ser. A Math. Phys. Eng. Sci., **362**(1824), pp. 2477–2512.

[70] Koehler, T., Frauenheim, T., and Jungnickel, G., 1995, "Stability, Chemical Bonding and Vibrational Properties of Amorphous Carbon at Different Mass Density," Phys. Rev. B, **52**(16), pp. 11837–11844.

[71] Drabold, D. A., Fedders, P. A., and Stumm, P., 1994, "Theory of Diamondlike Amorphous Carbon," Phys. Rev. B, **49**(23), pp. 16415–16422.

[72] Piscanec, S., Mauri, F., Ferrari, A. C., Lazzeri, M., and Robertson, J., 2005, "Ab Initio Resonant Raman Spectra of Diamond-like Carbons," Diam. Relat. Mater., **14**(3–7), pp. 1078–1083.

[73] Otto, A., and Schmidt, M., 2010, "Towards a Universal Numerical Simulation Model for Laser Material Processing," Phys. Procedia, **5**(PART 1), pp. 35–46.

[74] Shin, J., Ko, J., Jeong, S., Won, P., Lee, Y., Kim, J., Hong, S., Jeon, N. L., and Ko, S. H., 2021, "Monolithic Digital Patterning of Polydimethylsiloxane with Successive Laser Pyrolysis," Nat. Mater., **20**(1), pp. 100–107.

[75] Fardel, R., Urech, L., Lippert, T., Phipps, C., Fitz-Gerald, J. M., and Wokaun, A., 2009, "Laser Ablation of Energetic Polymer Solutions: Effect of Viscosity and Fluence on the Splashing Behavior," Appl. Phys. A Mater. Sci. Process., **94**(3), pp. 657–665.

[76] Bourgerette, C., Oberlin, A., and Inagaki, M., 1992, "Structural and Textural Changes from Polyimide Kapton to Graphite: Part I. Optical Microscopy and Transmission Electron Microscopy," J. Mater. Res., **7**(5), pp. 1158–1173.

[77] Yoshida, A., Kaburagi, Y., and Hishiyama, Y., 2006, "Full Width at Half Maximum Intensity of the G Band in the First Order Raman Spectrum of Carbon Material as a Parameter for Graphitization," Carbon, **44**(11), pp. 2333–2335.

[78] Inagaki, M., Harada, S., Sato, T., Nakajima, T., Horino, Y., and Morita, K., 1989, "Carbonization of Polyimide Film 'Kapton,'" Carbon, **27**(2), pp. 253–257.

[79] Inagaki, M., Ohta, N., and Hishiyama, Y., 2013, "Aromatic Polyimides as Carbon Precursors," Carbon, **61**, pp. 1–21.

[80] Hatori, H., Yamada, Y., and Shiraishi, M., 1994, "Bursting of Graphitized Polyimide Films through the Liberation of Included Nitrogen," Carbon, **32**(2), pp. 359–361.

[81] Reneker, D. H., and Yarin, A. L., 2008, "Electrospinning Jets and Polymer Nanofibers," Polymer (Guildf)., **49**(10), pp. 2387–2425.

[82] Inagaki, M., Hishiyama, Y., and Kaburagi, Y., 1994, "Effect of Heating Rate during Carbonization on Graphitization of Carbon Films Derived from Aromatic Polyimides," Carbon, **32**(4), pp. 637–639.

[83] Torrisi, F., Hasan, T., Wu, W., Sun, Z., Lombardo, A., Kulmala, T. S., Hsieh, G. W., Jung, S., Bonaccorso, F., Paul, P. J., Chu, D., and Ferrari, A. C., 2012, "Inkjet-Printed Graphene Electronics," ACS Nano, **6**(4), pp. 2992–3006.

[84] Biswas, R. K., Farid, N., O'Connor, G., and Scully, P., 2020, "Improved Conductivity of Carbonized Polyimide by CO 2 Laser Graphitization," J. Mater. Chem. C, **8**(13), pp. 4493–4501.

[85] Katagiri, G., 1996, "Raman Spectroscopy of Graphite and Carbon Materials and Its Recent Application," TANSO, **1996**(175), pp. 304–313.

[86] Wu, J. Bin, Lin, M. L., Cong, X., Liu, H. N., and Tan, P. H., 2018, "Raman Spectroscopy of Graphene-Based Materials and Its Applications in Related Devices," Chem. Soc. Rev., **47**(5), pp. 1822–1873.

[87] Marla, D., Zhang, Y., Jabbari, M., Sonne, M. R., Spangenberg, J., and Hattel, J. H., 2016, "A Computational Model for Heterogeneous Heating during Pulsed Laser Irradiation of Polymers Doped with Light-Absorbing Microparticles," Appl. Phys. A, **122**(12), p. 1042.

[88] Ruan, X., Wang, R., Luo, J., Yao, Y., and Liu, T., 2018, "Experimental and Modeling Study of CO2 Laser Writing Induced Polyimide Carbonization Process," Mater. Des., **160**, pp. 1168–1177.

[89] Brunco, D. P., Thompson, M. O., Otis, C. E., and Goodwin, P. M., 1992, "Temperature Measurements of Polyimide during KrF Excimer Laser Ablation," J. Appl. Phys., **72**(9), pp. 4344–4350.

[90] Dreyfus, R. W., 1992, “CN Temperatures above Laser Ablated Polyimide,” Appl. Phys. A Solids Surfaces, **55**(4), pp. 335–339.

[91] Ortelli, E. E., Geiger, F., Lippert, T., and Wokaun, A., 2001, “Pyrolysis of Kapton® in Air: An in Situ DRIFT Study,” Appl. Spectrosc., **55**(4), pp. 412–419.

[92] Ortelli, E. E., Geiger, F., Lippert, T., Wei, J., and Wokaun, A., 2000, “UV-Laser-Induced Decomposition of Kapton Studied by Infrared Spectroscopy,” Macromolecules, **33**(14), pp. 5090–5097.

[93] Hatori, H., Yamada, Y., Shiraishi, M., Yoshihara, M., and Kimura, T., 1996, “The Mechanism of Polyimide Pyrolysis in the Early Stage,” Carbon, **34**(2), pp. 201–208.

[94] Zhu, C., Ning, W., Xu, G., and Luo, L., 2014, “Influence of the Viscoelastic Properties of the Polyimide Dielectric Coating on the Wafer Warpage,” J. Electron. Mater., **43**(9), pp. 3255–3262.

[95] Kato, T., Yamada, Y., Nishikawa, Y., Ishikawa, H., and Sato, S., 2021, “Carbonization Mechanisms of Polyimide: Methodology to Analyze Carbon Materials with Nitrogen, Oxygen, Pentagons, and Heptagons,” Carbon, **178**, pp. 58–80.

[96] Wang, R., Duan, X., Yao, J., Ruan, X., Yao, Y., and Liu, T., 2020, “Processing–Structure–Property Relationship in Direct Laser Writing Carbonization of Polyimide,” J. Appl. Polym. Sci., **137**(34), pp. 1–13.

[97] Abdulhafez, M., Tomaraei, G. N., and Bedewy, M., 2021, “Fluence-Dependent Morphological Transitions in Laser-Induced Graphene Electrodes on Polyimide Substrates for Flexible Devices,” ACS Appl. Nano Mater., **4**(3), pp. 2973–2986.

[98] Nam, K.-H., Abdulhafez, M., Castagnola, E., Tomaraei, G. N., Cui, X. T., and Bedewy, M., 2021, “Laser Direct Write of Heteroatom-Doped Graphene on Molecularly Controlled Polyimides for Electrochemical Biosensors with Nanomolar Sensitivity,” Carbon.

[99] Schuepfer, D. B., Badaczewski, F., Guerra-Castro, J. M., Hofmann, D. M., Heiliger, C., Smarsly, B., and Klar, P. J., 2020, “Assessing the Structural Properties of Graphitic and Non-Graphitic Carbons by Raman Spectroscopy,” Carbon, **161**, pp. 359–372.

[100] Mezzi, A., and Kaciulis, S., 2010, “Surface Investigation of Carbon Films: From Diamond to Graphite,” Surf. Interface Anal., **42**(6–7), pp. 1082–1084.

[101] Kaciulis, S., 2012, “Spectroscopy of Carbon: From Diamond to Nitride Films,” Surf. Interface Anal., **44**(8), pp. 1155–1161.

[102] Bell, R. T., Jacobs, A. G., Sorg, V. C., Jung, B., Hill, M. O., Treml, B. E., and Thompson, M. O., 2016, “Lateral Temperature-Gradient Method for High-Throughput Characterization of Material Processing by Millisecond Laser Annealing,” ACS Comb. Sci., **18**(9), pp. 548–558.

[103] Gallais, L., Vidal, T., Lescoute, E., Pontillon, Y., and Rullier, J. L., 2021, "High Power Continuous Wave Laser Heating of Graphite in a High Temperature Range up to 3800 K," J. Appl. Phys., **129**(4).

[104] Wakefield, R. M., and Peterson, D. L., 1973, "Graphite Ablation in Combined Convective and Radiative Heating," J. Spacecr. Rockets, **10**(2), pp. 149–154.

[105] McKinley, G. H., 2005, "Visco-Elasto-Capillary Thinning and Break-up of Complex Fluids," Rheol. Rev., **3**(05), pp. 1–48.

[106] Jones, T. J., Reynolds, C. D., and Boothroyd, S. C., 2019, "Fluid Dynamic Induced Break-up during Volcanic Eruptions," Nat. Commun., **10**(1), p. 3828.

[107] Gaillard, A., Sijs, R., and Bonn, D., 2021, "What Determines the Drop Size in Sprays of Polymer Solutions?"

[108] Keshavarz, B., Houze, E. C., Moore, J. R., Koerner, M. R., and McKinley, G. H., 2016, "Ligament Mediated Fragmentation of Viscoelastic Liquids," Phys. Rev. Lett., **117**(15).

[109] Villermaux, E., 2020, "Fragmentation versus Cohesion," J. Fluid Mech., **898**, pp. 1–121.

[110] Gonnermann, H. M., and Manga, M., 2007, "The Fluid Mechanics inside a Volcano," Annu. Rev. Fluid Mech., **39**, pp. 321–356.

[111] Derby, B., 2010, "Inkjet Printing of Functional and Structural Materials: Fluid Property Requirements, Feature Stability, and Resolution," Annu. Rev. Mater. Res., **40**(1), pp. 395–414.

[112] Modesto-López, L. B., Pérez-Arjona, A., and Ganán-Calvo, A. M., 2019, "Flow Blurring-Enabled Production of Polymer Filaments from Poly(Ethylene Oxide) Solutions," ACS Omega, **4**(2), pp. 2693–2701.

[113] Miller, E., Gibson, B., McWilliams, E., and Rothstein, J. P., 2005, "Collision of Viscoelastic Jets and the Formation of Fluid Webs," Appl. Phys. Lett., **87**(1).

[114] Villermaux, E., 2012, "The Formation of Filamentary Structures from Molten Silicates: Pele's Hair, Angel Hair, and Blown Clinker," Comptes Rendus Mécanique, **340**(8), pp. 555–564.

[115] Kong, D., Kang, M., Kim, K. Y., Jang, J., Cho, J., In, J. Bin, and Lee, H., 2020, "Hierarchically Structured Laser-Induced Graphene for Enhanced Boiling on Flexible Substrates," ACS Appl. Mater. Interfaces, **12**(33), pp. 37784–37792.

[116] Wang, M., Yang, Y., and Gao, W., 2021, "Laser-Engraved Graphene for Flexible and Wearable Electronics," Trends Chem.

[117] Muzyka, K., and Xu, G., 2021, "Laser-Induced Graphene in Facts, Numbers, and Notes in View of Electroanalytical Applications: A Review," Electroanalysis, pp. 1–17.

[118] Griesche, Christian; Hoecherl, Kilian; Baeumner, A. J., Griesche, C., Hoecherl, K., and Baeumner, A. J., 2021, "Substrate-Independent Laser-Induced Graphene Electrodes for Microfluidic Electroanalytical Systems," ACS Appl. Nano Mater., **under revi**.

[119] Nam, K., Abdulhafez, M., Najaf Tomaraei, G., and Bedewy, M., 2021, "Laser-Induced Fluorinated Graphene for Superhydrophobic Surfaces with Anisotropic Wetting and Switchable Adhesion," Appl. Surf. Sci., p. 151339.

[120] Alhajji, E., Zhang, F., and Alshareef, H. N., 2021, "Status and Prospects of Laser-Induced Graphene for Battery Applications," Energy Technol., **9**(10), pp. 1–15.

[121] Xu, Y., Fei, Q., Page, M., Zhao, G., Ling, Y., Chen, D., and Yan, Z., 2021, "Laser-Induced Graphene for Bioelectronics and Soft Actuators," Nano Res., **12**(1).

[122] Lahcen, A. A., Rauf, S., Beduk, T., Durmus, C., Aljedaibi, A., Timur, S., Alshareef, H. N., Amine, A., Wolfbeis, O. S., and Salama, K. N., 2020, "Electrochemical Sensors and Biosensors Using Laser-Derived Graphene: A Comprehensive Review," Biosens. Bioelectron., **168**(August), p. 112565.

[123] Santos, N. F., Pereira, S. O., Moreira, A., Girão, A. V., Carvalho, A. F., Fernandes, A. J. S. S., and Costa, F. M., 2021, "IR and UV Laser-Induced Graphene: Application as Dopamine Electrochemical Sensors," Adv. Mater. Technol., **6**(6), p. 2100007.

[124] Xu, G., Jarjes, Z. A., Desprez, V., Kilmartin, P. A., and Travas-Sejdic, J., 2018, "Sensitive, Selective, Disposable Electrochemical Dopamine Sensor Based on PEDOT-Modified Laser Scribed Graphene," Biosens. Bioelectron., **107**(February), pp. 184–191.

[125] Tan, P. S., Vaughan, E., Islam, J., Burke, N., Iacopino, D., and Tierney, J. B., 2021, "Laser Scribing Fabrication of Graphitic Carbon Biosensors for Label-Free Detection of Interleukin-6," Nanomaterials, **11**(8), pp. 1–14.

[126] Nayak, P., Kurra, N., Xia, C., and Alshareef, H. N., 2016, "Highly Efficient Laser Scribed Graphene Electrodes for On-Chip Electrochemical Sensing Applications," Adv. Electron. Mater., **2**(10), pp. 1–11.

[127] Murray, R., Burke, M., Iacopino, D., and Quinn, A. J., 2021, "Design of Experiments and Optimization of Laser-Induced Graphene," ACS Omega, **6**(26), pp. 16736–16743.

[128] Wahab, H., Jain, V., Tyrrell, A. S., Seas, M. A., Kotthoff, L., and Johnson, P., 2020, "Machine-Learning-Assisted Fabrication: Bayesian Optimization of Laser-Induced Graphene Patterning Using in-Situ Raman Analysis," Carbon, **167**, pp. 609–619.

[129] Minhas-Khan, A., Nambi, S., and Grau, G., 2021, "Low-Resistance Laser-Induced Graphitic Carbon by Maximizing Energy Delivery and Pulse Overlap," Carbon, **181**, pp. 310–322.

[130] Cogan, S. F., 2008, "Neural Stimulation and Recording Electrodes," Annu. Rev. Biomed. Eng., **10**, pp. 275–309.

[131] Nimbalkar, S., Castagnola, E., Balasubramani, A., Scarpellini, A., Samejima, S., Khorasani, A., Boissenin, A., Thongpang, S., Moritz, C., and Kassegne, S., 2018, "Ultra-Capacitive Carbon Neural Probe Allows Simultaneous Long-Term Electrical Stimulations and High-Resolution Neurotransmitter Detection," Sci. Rep., **8**(1), pp. 1–14.

[132] Castagnola, E., Garg, R., Rastogi, S. K., Cohen-Karni, T., and Cui, X. T., 2021, "3D Fuzzy Graphene Microelectrode Array for Dopamine Sensing at Sub-Cellular Spatial Resolution," Biosens. Bioelectron., **191**(April).

[133] Ansaldo, A., Castagnola, E., Maggiolini, E., Fadiga, L., and Ricci, D., 2011, "Superior Electrochemical Performance of Carbon Nanotubes Directly Grown on Sharp Microelectrodes," ACS Nano, **5**(3), pp. 2206–2214.

[134] Felton, S. M., Tolley, M. T., Shin, B., Onal, C. D., Demaine, E. D., Rus, D., and Wood, R. J., 2013, "Self-Folding with Shape Memory Composites," Soft Matter, **9**(32), pp. 7688–7694.

[135] ANSYS Inc., *Mechanical APDL Element Reference*.

[136] Mailen, R. W., Liu, Y., Dickey, M. D., Zikry, M., and Genzer, J., 2015, "Modelling of Shape Memory Polymer Sheets That Self-Fold in Response to Localized Heating," Soft Matter, **11**(39), pp. 7827–7834.

[137] Mailen, R. W., Dickey, M. D., Genzer, J., and Zikry, M. A., 2017, "A Fully Coupled Thermo-Viscoelastic Finite Element Model for Self-Folding Shape Memory Polymer Sheets," J. Polym. Sci. Part B Polym. Phys., **55**(16), pp. 1207–1219.

[138] Callens, S. J. P., Tümer, N., and Zadpoor, A. A., 2019, "Hyperbolic Origami-Inspired Folding of Triply Periodic Minimal Surface Structures," Appl. Mater. Today, **15**, pp. 453–461.

[139] Xiang, X. M., Lu, G., and You, Z., 2020, "Energy Absorption of Origami Inspired Structures and Materials," Thin-Walled Struct., **157**(August).

[140] Kamrava, S., Mousanezhad, D., Ebrahimi, H., Ghosh, R., and Vaziri, A., 2017, "Origami-Based Cellular Metamaterial with Auxetic, Bistable, and Self-Locking Properties," Sci. Rep., **7**, pp. 1–9.

[141] Wang, Z., Iquebal, A. S., and Bukkapatnam, S. T. S., 2018, "A Vision-Based Monitoring Approach for Real-Time Control of Laser Origami Cybermanufacturing Processes," Procedia Manuf., **26**, pp. 1307–1317.

[142] Iquebal, A. S., Wang, Z., Ko, W. H., Wang, Z., Kumar, P. R., Srinivasa, A., and Bukkapatnam, S. T. S., 2018, "Towards Realizing Cybermanufacturing Kiosks: Quality Assurance Challenges and Opportunities," Procedia Manuf., **26**, pp. 1296–1306.

[143] Bobinger, M. R., Romero, F. J., Salinas-Castillo, A., Becherer, M., Lugli, P., Morales, D. P., Rodríguez, N., and Rivadeneyra, A., 2019, "Flexible and Robust Laser-Induced Graphene Heaters Photothermally Scribed on Bare Polyimide Substrates," Carbon, **144**, pp. 116–126.

[144] Zhou, R., Li, P., Fan, Z., Du, D., and Ouyang, J., 2017, "Stretchable Heaters with Composites of an Intrinsically Conductive Polymer, Reduced Graphene Oxide and an Elastomer for Wearable Thermotherapy," J. Mater. Chem. C, **5**(6), pp. 1544–1551.

[145] Chen, J., Wang, Y., Liu, F., and Luo, S., 2020, "Laser-Induced Graphene Paper Heaters with Multimodally Patternable Electrothermal Performance for Low-Energy Manufacturing of Composites," ACS Appl. Mater. Interfaces, **12**(20), pp. 23284–23297.

[146] Wang, W., Han, B., Zhang, Y., Li, Q., Zhang, Y. L., Han, D. D., and Sun, H. B., 2020, "Laser-Induced Graphene Tapes as Origami and Stick-On Labels for Photothermal Manipulation via Marangoni Effect," Adv. Funct. Mater., **2006179**, pp. 1–11.

[147] Dallinger, A., Kindlhofer, P., Greco, F., and Coclite, A. M., 2021, "Multiresponsive Soft Actuators Based on a Thermoresponsive Hydrogel and Embedded Laser-Induced Graphene," ACS Appl. Polym. Mater.

[148] Deng, H., Zhang, C., Su, J. W., Xie, Y., Zhang, C., and Lin, J., 2018, "Bioinspired Multi-Responsive Soft Actuators Controlled by Laser Tailored Graphene Structures," J. Mater. Chem. B, **6**(34), pp. 5415–5423.

[149] Zhang, T. Y., Wang, Q., Deng, N. Q., Zhao, H. M., Wang, D. Y., Yang, Z., Liu, Y., Yang, Y., and Ren, T. L., 2017, "A Large-Strain, Fast-Response, and Easy-to-Manufacture Electrothermal Actuator Based on Laser-Reduced Graphene Oxide," Appl. Phys. Lett., **111**(12), p. 121901.

[150] Romero, R., Guerreiro, P. T., Hendow, S. T., and Salcedo, J. R., 2011, "Dynamic Pulsing of a MOPA Fiber Laser," Int. Conf. Appl. Opt. Photonics, **8001**, p. 80010T.

[151] Hendow, S. T., Guerreiro, P. T., Schilling, N., and Rabe, J., 2010, "Pulse Shape Control of a MOPA Fiber Laser for Marking of Stainless Steel and Other Materials," *International Congress on Applications of Lasers & Electro-Optics*, Laser Institute of America, pp. 951–958.

[152] Dorin, B., Parkinson, P., and Scully, P., 2017, "Direct Laser Write Process for 3D Conductive Carbon Circuits in Polyimide," J. Mater. Chem. C, **5**(20), pp. 4923–4930.